AN EXTREME ULTRAVIOLET AND PLASMA SPECTROMETER SCIENTIFIC PAYLOAD FOR A CUBESAT

by

AYOKUNLE OLUWASEUN AYELESO

Thesis submitted in fulfilment of the requirements for the degree

Master of Technology: Electrical Engineering

in the Faculty of Engineering

at the Cape Peninsula University of Technology

Supervisor: Prof. R.R. van Zyl

Bellville

April 2014

DECLARATION

I, Ayokunle Oluwaseun Ayeleso, declare that the contents of this dissertation/thesis represent my own unaided work, and that the dissertation/thesis has not previously been submitted for academic examination towards any qualification. Furthermore, it represents my own opinions and not necessarily those of the Cape Peninsula University of Technology (CPUT).

Signed **Date**

ABSTRACT

In the Earth's upper atmosphere, damage to spacecraft electronics is caused by the exposure to extreme ultraviolet (EUV) radiation, solar protons and cosmic rays emanating from the Sun. One particular region where these types of radiation occur is the South Atlantic Magnetic Anomaly (SAMA) region. Therefore, there is a need to design sensors which could be used to investigate the flux and energy levels of radiation in this region. In order to do so, the present study focuses on the numerical simulations of plasma (atomic oxygen ion) in the ionosphere's F-layer region using the principle of Langmuir single probe theory. Another goal of this study is to investigate the behaviour of a copper plate sensor under exposure to ultraviolet (UV) radiation through simulation and experimentation in a laboratory setting in terms of the photoelectric effect principle.

Simulation results of the plasma model of the ionosphere's F-layer region using an ideal single spherical probe showed that ionospheric plasma parameters such as electron temperature and electron density can be determined using the $I-V$ characteristic curve obtained from the probe. Similarly, the simulation results of the behaviour of the copper plate under exposure to UV radiation showed that UV light with wavelengths shorter than 237 nm produced photocurrents. After calculations and simulations, the stopping potentials that could decelerate electrons emitted with UV radiation wavelengths between 100 nm and 237 nm are, respectively, between -7.6 V and -0.2 V. When comparing the calculated copper stopping potentials with the simulated copper stopping potentials, the results converge for shorter wavelengths. These short wavelengths are relevant in this study because they are comparable to EUV wavelengths (10 nm to 121 nm) in the SAMA region. Therefore, the stopping potential results were used in the experimental design and VUV radiation testing of the sensor prototypes.

Two different copper sensor prototypes, namely a spherical extreme ultraviolet and plasma spectrometer (SEPS) sensor and a planar sensor were designed and constructed for the realisation of this project. The planar sensor, with dimensions that fit on the sides of a one unit (1U) CubeSat was developed to minimise the experimental uncertainty observed with the SEPS sensor. The aim of this study is to characterise the sensors and their responses to typical plasma and EUV radiation levels using the facilities available in the Western Cape region (South Africa). Plasma testing was not investigated due to lack of test facilities. Therefore, the investigation into plasma measurements was simulation-based. Experimental EUV radiation testing was conducted. Extreme ultraviolet radiation measurements were performed with different vacuum ultraviolet (VUV) sources, namely a pulsed laser and a deuterium lamp (steady) radiation. These measurements posed challenges due to the significant ambient noise present in the laboratory. Consequently, the study looked at both

time and frequency domain analyses as avenues to mitigate the effect of noise on the measurements.

The initial VUV pulsed laser radiation experiments, with the SEPS sensor used as a two plate spherical capacitor by connecting its outer grids and positively biased, produced no voltage pulses. Only the significant ambient noise levels were observed. The absence of voltage pulses can be attributed to the fact that electrons escaped the metal sphere too energetically, and may fly through the outer combined grids under the additional acceleration of the positive bias and are not collected. A triple probe structure with a negative inner grid is necessary to slow down electrons enough to be captured by the positive outer grid. Based on this principle of operation, the simpler planar sensor was used for further experimentation. In that way, the experimental uncertainties that are compounded by the concentric spherical construction of the SEPS sensors would be avoided.

In the VUV pulsed laser radiation experiment, the time-averaged measured terminal voltages were obtained. The frequency content of the measured terminal voltages was also observed through performing a Fast Fourier Transform (FFT) on the time signals. Significant harmonics were observed at frequencies ranging from 210 MHz to 250 MHz. In addition, these results showed that output voltage pulses were detected through both time and frequency domain analyses.

In other experiments with VUV deuterium lamp (steady) radiation, the measured time-averaged terminal voltages obtained from the planar sensor showed significant generation of currents (0 µA, -0.7 µA and 1.0 µA) which compared well with the theoretical calculation (0.69 µA). Conclusively, these results validate the measurement approach and operation of the planar sensor and could be used to design a one unit (1U) CubeSat sensor that measures EUV radiation when launched into space. The study further highlights the challenges that future sensor development will face in terms of the facilities available in the region, due to the very small signals that have to be measured in laboratory environments with high levels of ambient noise.

ACKNOWLEDGEMENTS

I wish to thank:

- The Almighty God, for giving me the grace to reach this far.
- My supervisor, Professor Robert van Zyl for his supervision, guidance, contribution and encouragement throughout the thesis write up.
- Dr C.M. Steekamp for her dedication in making the project a success.
- The management of French South African Institute of Technology (F'SATI), for sponsoring my studies at the Cape Peninsula University of Technology. Without them the project will not have been possible.
- The management of the Laser Research Institute, Physics Department at the University of Stellenbosch for providing the testing facilities used for this project.
- The management of IThemba Laboratory for providing some of the equipment used for this project.
- My colleagues in the Department of Electrical Engineering, Cape Peninsula University of Technology Bellville campus for the support, guidance and encouragement I received from them.
- My family, especially Dr Ademola Ayeleso, for their support and encouragement during the time of my studies. Their advice and moral support have helped me to the conclusion of the project.
- Berenice Ayeleso for her contribution and support toward my studies.
- Minko Flavien and Craig Olivier for their support and contribution towards my studies.

The financial assistance of the French South African Institute of Technology and the National Research Foundation towards this research is acknowledged. Opinions expressed in this thesis and the conclusions arrived at, are those of the author, and not necessarily to be attributed to the National Research Foundation.

DEDICATION

This research is dedicated to almighty God and also to my parents CH & Mrs P.B AYELESO, for their support and encouragement for seeing me through in achieving quality education.

RESEARCH OUTPUTS

1) Member of the team that won the 1st prize in category 2 of the internationally recognised 2nd Mission Idea Contest (MIC 2) for micro/nano-satellite utilisation (Tokyo, Japan, 10 October 2012)

   Title: Underground and surface water detection and monitoring using a microsatellite

2) Won the 1st prize for oral presentation at the CPUT Postgraduate Conference 2013 (Cape Town, South Africa, 5 November 2013)

   Title: Simulation of the behaviour of a copper plate material exposed to vacuum ultraviolet radiation

3) Poster presentation at the CPUT Research Day 2013 (Cape Town, South Africa, 29 November 2013)

   Title: Plasma measurement in the ionosphere

4) Submitted manuscript to an accredited journal:
   Journal name: Journal of Engineering, Design and Technology
   Title: Photocurrents obtained from a triple planar probe sensor for in situ extreme ultraviolet (EUV) radiation measurements on low Earth orbiting CubeSats

TABLE OF CONTENTS

LIST OF FIGURES

LIST OF TABLES

GLOSSARY

Symbols	Definition/Explanation
a	Sheath distance
A_p	Probe surface area
A_{p1}	Surface area for probe P_1
A_{p2}	Surface area for probe P_2
A_{p3}	Surface area for probe P_3
c	Speed of light
C	Capacitance
d_{sphere}	Sphere diameter
e	Unit electron charge
E	Electron energy
$E_{K\ electrons}$	Electron kinetic energy
E_{photon}	Photon energy
E_{tr}	Transfer energy
$\mathrm{F}(v)$	Maxwellian electron velocity distribution function
h	Planck's constant
$\hbar$	Reduced Planck's constant
I	Photocurrent
I_e	Electron current
I_{esat}	Electron-saturation current
I_i	Ion current
I_{isat}	Ion-saturation current
I_{probe}	Probe current
I_{sensor}	Sensor current
J_{esat}	Electron-saturation current density

J_{isat}	Ion-saturation current density
K_B	Boltzmann's constant
m_e	Electron mass
m_i	Ion mass
m_h	Mass of the heavy particles
n_e	Electron density
n_i	Ion density
$N_{electrons}$	Number of electrons
N_p	Number of particles
N	Number of photons associated with the VUV deuterium light
P	Power received at the sensor
Q	Charge
r_p	Probe radius
R	Load resistor
T	Temperature
T_e	Electron temperature
T_i	Ion temperature
V_b	Probe bias voltage
V_{co}	Terminal voltage of fully charged capacitor
V_f	Floating probe potential
V_{stop}	Stopping potential
V_p	Plasma potential
v	Average velocity of plasma particles in thermal equilibrium
v_{min}	Minimum velocity of electrons
v_y	Average velocity of electrons travelling in the y-direction
ω	Frequency of the VUV 140 nm light source
ω_p	Plasma frequency

Φ	Work function
τ	Mean time of collisions between plasma and neutral atoms
λ_D	Debye length
ε_o	Permittivity of free space
Ω	Solid angle
ξ	Electric field

Terms/Abbreviation	**Definition/Explanation**
COTS	Commercial-off-the-shelf
CPUT	Cape Peninsula University of Technology
ERR	Electron-retardation region
ESR	Electron-saturation region
EUV	Extreme Ultraviolet
FFT	Fast Fourier Transform
F'SATI	French South African Institute of Technology
GDP	Gas-discharge plasma
HF	High Frequency
IG	Inner grid
IGS	Inner grid sphere
ISR	Ion-saturation region
LEO	Low Earth Orbit
LPP	Laser-produced plasma
MP	Metallic plate
MS	Metallic sphere
OG	Outer grid
OGS	Outer grid sphere
OML	Orbital motion limited
QE	Quantum efficiency
RF	Radio frequency
SALT	Southern Africa Large Telescope

SAMA	South Atlantic Magnetic Anomaly
SANSA	South African National Space Agency
SEPS	Spherical Extreme Ultraviolet and Plasma Spectrometer
SKA	Square Kilometre Array
SRI	Spectral radiant intensity
SSE	Satellite Systems Engineering
TSL	Thin sheath limited
UVA	Ultraviolet A
UVB	Ultraviolet B
UVC	Ultraviolet C
VARB	Van Allen Radiation Belt
VUV	Vacuum Ultraviolet

CHAPTER ONE: GENERAL INTRODUCTION

1.1 Introduction

South Africa is becoming a prominent innovator in aerospace research and development. Setting up facilities and agencies such as the South African National Space Agency (SANSA), the Southern Africa Large Telescope (SALT) at Sutherland and the Square Kilometre Array (SKA) has contributed immensely toward the development of space science and technology. The French South African Institute of Technology (F'SATI) at the Cape Peninsula University of Technology (CPUT) is actively involved in the development of space technology in South Africa. F'SATI introduced a Satellite Systems Engineering (SSE) programme in 2009. The focus of the SSE is in line with the South African Government's goal of developing human capacity in the specialised area of satellite engineering. Students receive hands-on training by working on satellite related projects (F'SATI, 2013). The students, staff and engineers at F'SATI recently developed a one unit (1U) CubeSat, ZACUBE-1 (Figure 1.1), and are currently developing a three unit (3U) CubeSat, ZACUBE-2 (Figure 1.2) (Visser, 2009). ZACUBE-1 carries a high frequency (HF) beacon payload to characterise radio propagation through the ionosphere. In future missions, a low-cost charged particle sensor will be used as a payload on a CubeSat for monitoring the distribution of energetic particles in the South Atlantic Magnetic Anomaly (SAMA) region.

A CubeSat is a nano-satellite which has a standard form factor of 10 cm x 10 cm x 10 cm (1U) and mass of up to 1.33 kg. It can also be stacked into larger standard form factors, for example 30 cm x 10 cm x 10 cm (3U) (Simmons, 2008:5−13). Commercial-off-the-shelf (COTS) components are widely employed to build CubeSats, which ultimately reduces cost. A CubeSat provides a platform to test technologies before implementation on expensive satellites and allows students to work on various aspects of satellite engineering. CubeSats can be used for various other applications, such as remote sensing and space weather research.

Mavromichalaki *et al*. (2006:1141) states that “Space weather refers to conditions on the Sun and in the solar wind, magnetosphere, ionosphere and thermosphere that can influence the performance and reliability of space borne and ground based technological systems and endanger human life and health”. One particular region of interest to space weather research is the SAMA (Heirtzler, 2002:1701; Casadio & Arino, 2011:1056). Examples of launched CubeSat space weather missions are Cute-1.7 and the Illinois Observing Nano-satellite mission (Simmons, 2008:9−11). The main objectives of Cute-1.7 is to monitor the flux of charged particles in the Low Earth Orbit (LEO) and to determine the total damage caused by radiation in a year mission life time while the main objective of the Illinois Observing Nano-satellite mission is to measure the airglow molecules of oxygen in the Earth's mesosphere (Simmons, 2008:10−11).

The focus of the present study is to investigate the behaviour of a spherical extreme ultraviolet and plasma spectrometer (SEPS) sensor and a planar sensor when exposed to plasma and vacuum ultraviolet (VUV) radiation, in a laboratory environment, mimicking the actual extreme ultraviolet (EUV) radiation environment.

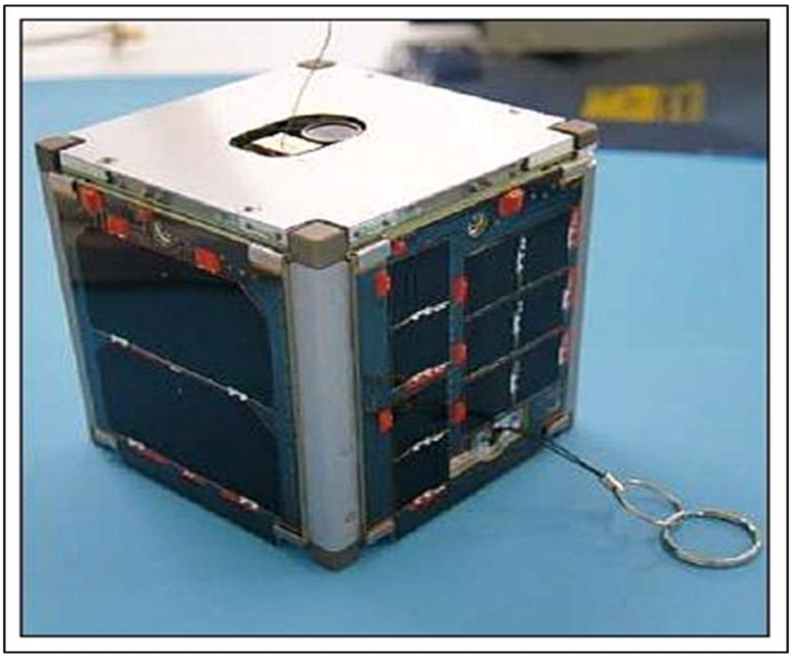

Figure 1.1: Picture of ZACUBE-1 which was launched on 21 November 2013 (From F'SATI, 2013)

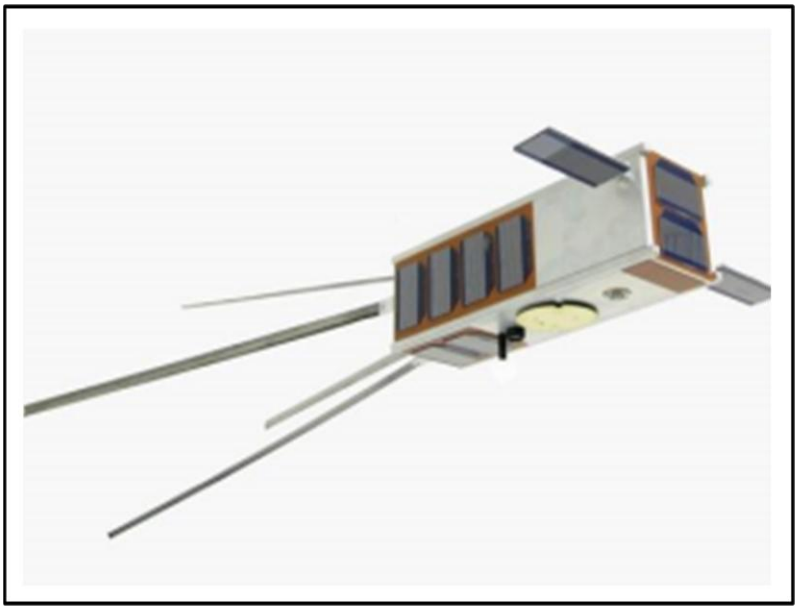

Figure 1.2: Representation of ZACUBE-2, a 3U CubeSat under development by CPUT students (Adapted from F'SATI, 2013)

1.2 Research background and awareness of the problem

In the LEO, damage to satellite electronics occurs due to intensive exposure to EUV radiation, cosmic rays and high energy protons throughout the SAMA region. Ginet *et al*. (2007:1) states that in the absence of high-latitude solar proton events, the SAMA is the main region where satellites are exposed to high energy protons. The SAMA region exists at an altitude of about 400 to 1700 km within the inner Van Allen Radiation Belt (VARB) of the LEO. This region is also located in the southern hemisphere off the coast of Brazil and is very susceptible to space weather (Ginet *et al*., 2007:1). The SAMA region is mostly populated with plasma and radiation, which pose a threat to human life and degrade satellite electronic systems. For these reasons, space scientists will continue to develop suitable instruments that will aid in monitoring the space environment. In addition, there is need for a better understanding of the SAMA to mitigate the detrimental effects of radiation in this region.

1.3 Research statement

There is a need to characterise and model the SAMA region. This has necessitated research into sensors that can be used for such measurements. The focus of this research is to study the sensors' electric response to plasma and EUV radiation.

1.4 Objectives of the research

In view of the above:

- The principles of using a spherical sensor and a planar sensor based on Langmuir probe theory and the photoelectric effect will be investigated through the development of sensor prototypes.
- The testing of such sensors will be investigated.
- Attention is given to the practical challenges associated with these tests at the available testing and calibration facilities in the Western Cape (South Africa) to facilitate future sensor development activities.

1.5 Investigative questions

The investigation questions to guide the research are:

- Which types of sensors can be used to investigate the plasma and radiation in the SAMA region?
- Which materials can be used to develop the sensors?
- How can the sensors be developed and adapted to fit within the limitations of CubeSat design?
- Which facilities are available in the Western Cape region to develop, test and characterise the sensors?

- How can the sensors be calibrated and tested for measuring radiation?
- What are the practical challenges experienced in test environment?

1.6 Significance of the research

This research:

- Contributes to the body of knowledge of plasma and radiation sensors.
- Results in the development of sensors which could be used for monitoring the flux and energy levels of radiation.
- Lays a platform for future sensor development by identifying the practical challenges that are posed in terms of the facilities available, as well as experimental difficulties associated with the testing of the sensors.
- Suggests methodologies for testing the sensors despite the associated experimental challenges. These challenges are mostly very small currents that need to be measured in very noisy environments.
- Identifies experimental complexities that need to be addressed by future researchers.
- Helps scientists and engineers to improve space weather monitoring and forecasting.

1.7 Research delineation

The research concerns particle and radiation sensors that are compatible with CubeSat technology. Emphasis is placed on the calibration and testing of the sensors. Tests are limited to the facilities available in the Western Cape region. For this region, plasma measurement is excluded due to limited availability of facilities. Therefore, only plasma simulations are done and EUV radiation testing is conducted.

1.8 Research methodology

The following methods of investigation are followed to achieve the objectives of the research.

Literature review: Relevant resources were consulted to have a broad understanding of the research field.

Experiment and *evaluation*: The experimental setup is designed to test the functionality of the sensors when exposed to intensive ultraviolet (UV) radiation. This entails subjecting the sensors to various radiation conditions and observing their photocurrent responses. Once the sensors are tested successfully, they can be integrated with the CubeSat subsystems.

Critical analysis of findings: The sensors' functionality test results are analysed and compared with theory. There is also a critical discussion of the available testing facilities and the testing environment in these laboratories.

1.9 Summary of chapters

- Chapter One gave a general introduction and overview of what the project is about. The research problem, research statement, research objectives, investigative questions, significance and delineation of the research have been discussed.
- Chapter Two reviews the literature supporting the research. The chapter focuses on various plasma probe and EUV radiation measurement techniques.
- Chapter Three deals with the numerical simulation of the measurement of plasma in the ionosphere's F-layer region. This chapter concludes with simulating the expected behaviour of a copper sensor when exposed to intensive UV radiation.
- Chapter Four deals with the development of EUV radiation sensor prototypes and their experimental test setup. In addition, the results obtained from the different experiments conducted, are discussed. This chapter concludes with comparing the experimental results with theory.
- Chapter Five concludes the study. It summarises the key findings and also gives recommendations for future research.

CHAPTER TWO: LITERATURE REVIEW

2.1 Introduction

This chapter reviews the literature supporting the research. The chapter focuses on the study of EUV radiation and plasma probe theory. A theoretical overview of the Langmuir single, double and the triple probes is given.

2.2 South Atlantic Magnetic Anomaly

Solar and cosmic radiation consists mainly of protons, electrons and ions. During solar storms, these sources of radiation diffuse toward the Earth and are often trapped by the Earth's magnetic field in the VARB region. The Earth's magnetic axis is inclined to the Earth's rotational axis by 11° and the VARB is a region that is symmetric to the Earth's magnetic axis (Figure 2.1). The inner VARB is closest to the Earth's surface over the South Atlantic Ocean and farthest from the Earth's surface over the North Pacific Ocean (Figure 2.1) (Heirtzler, 2002:1701; Casadio & Arino, 2011:1056). Above the South Atlantic Ocean is the SAMA region where the Earth's magnetic field is very weak. Radiation in the SAMA is elevated. As a result, the region is extremely hazardous to spacecraft electronics and poses a threat to human life (Heirtzler, 2002:1701; De Santis & Qamili, 2010:339).

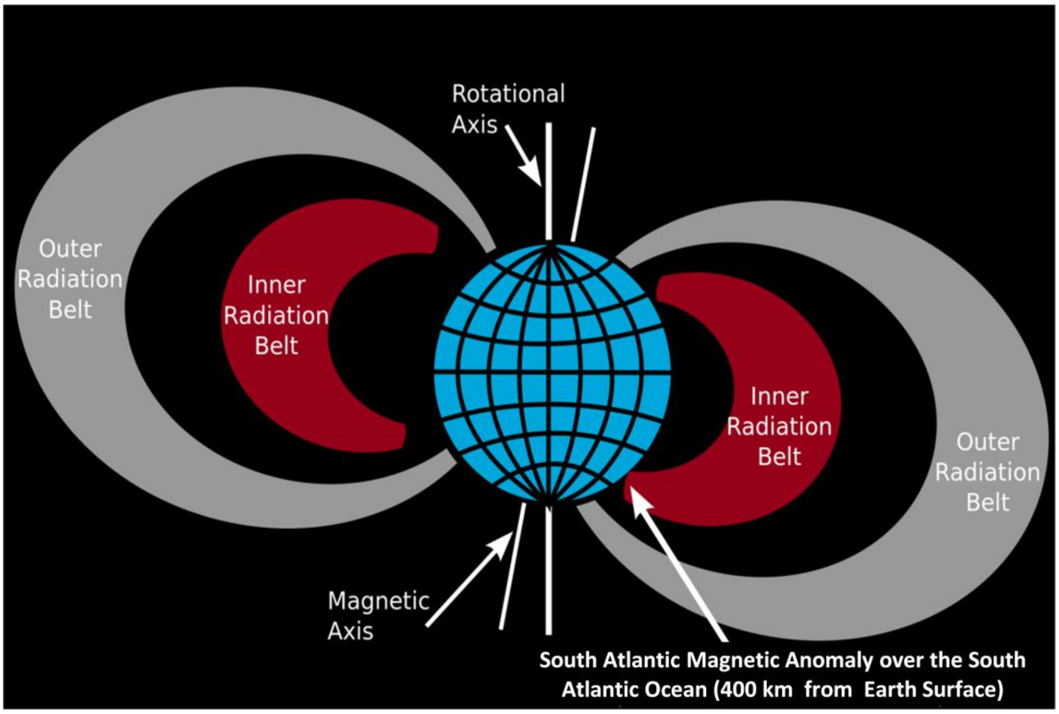

Figure 2.1: Schematic representation of the South Atlantic Magnetic Anomaly (Adapted from Robin, 2006)

2.3 Highly Energetic Charged Particles

The highly energetic charged particle formation begins within a layer of the Earth’s atmosphere called the ionosphere. This layer extends from an altitude of about 90 km to 1000 km above the Earth's surface and is often ionised by solar radiation. Solar radiation in this layer is strong enough to dislodge electrons from molecules, thus, producing free electrons with positively charged ions (Escobar, 2009:7).

When high energy charged particles (protons, electrons and ions) originated from the Sun diffuse throughout the atmosphere, their motion are restricted and trapped in the near Earth environment (VARB) (Stassinopoulos & Raymond, 1988:1423). These trapped charged particles, because of their charge, move in opposite directions, that is, electrons drift eastward while protons and heavy ions drift westward within the Earth's magnetic field lines. The energetic trapped electrons (below 10 MeV) are in the inner and the outer zone of the VARB (Figure 2.1). Contrary to the electrons, the energetic trapped protons (above 1 MeV) are often observed as the most penetrating radiation in the SAMA region. This is due to their intensive flux in the LEO (Stassinopoulos & Raymond, 1988:1424−1425). Furthermore, the interaction between protons, electrons, ions and orbiting spacecraft is hazardous to the spacecraft and causes degradation of spacecraft electronic materials and loss of spacecraft data (Mavromichalaki *et al*., 2007:1089−1093). With the aim of finding a solution to the above effects, the sensors presented in the current study could be used to measure particles in the SAMA region.

2.4 Extreme Ultraviolet Radiation

Extreme ultraviolet radiation can be obtained from two kinds of plasmas in the laboratory: the laser-produced plasma (LPP) and the gas-discharge plasma (GDP) (Ota *et al.,* 2006:28−29). Figure 2.2 depicts the EUV radiation source mode of detection. In this figure, the EUV light source is collected by the collecting optics (normal incidence and total reflection mirrors) and transmitted to the intermediate focus. The intermediate focus is the entrance through which the reflecting surface (illuminator) is illuminated. Furthermore, the UV spectra are subdivided into EUV (10 to 121 nm), VUV (10 to 200 nm), ultraviolet C (UVC) (100 to 280 nm), ultraviolet B (UVB) (280 to 315 nm) and ultraviolet A (UVA) (315 to 400 nm) (Tobiska & Nusinov, 2000:388; Tobiska & Nusinov, 2005:5−10).

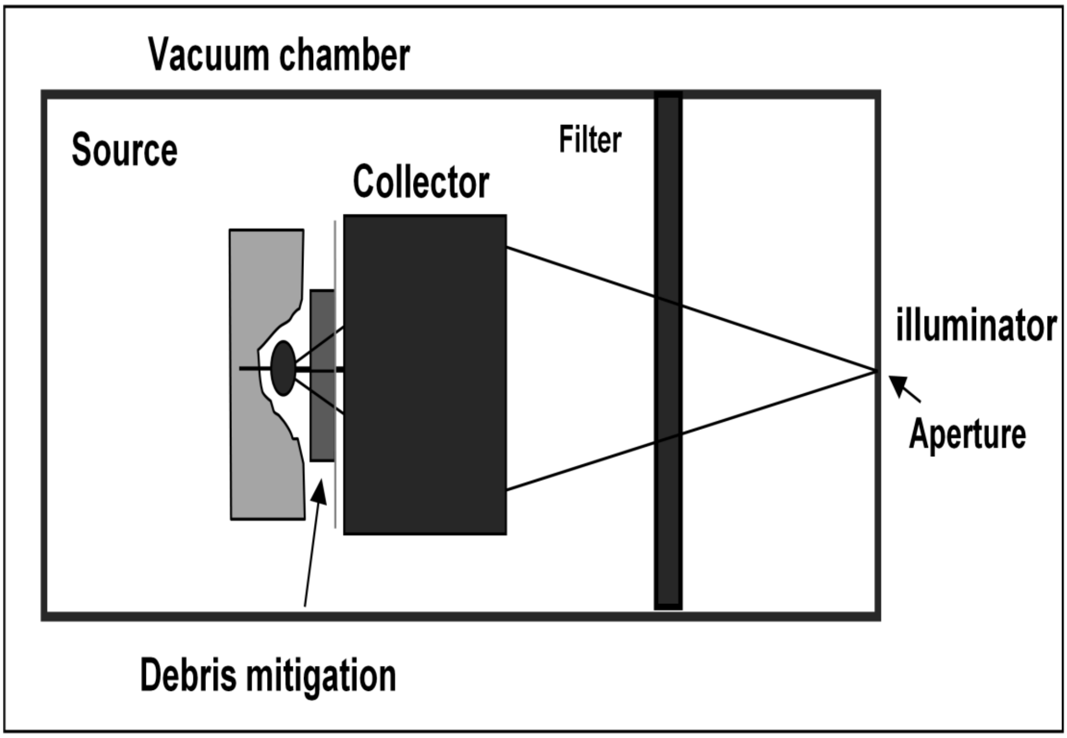

Figure 2.2: Extreme ultraviolet radiation source mode of detection (Adapted from Ota *et al.,* 2006:29)

2.5 Plasma

Chen (1984:3) describes plasma as the quasi-neutral gas of charged and neutral particles which display a collective behaviour. When a material at high temperature is ionised, its state is transformed from solid to liquid and then to gaseous form. This ionised gas is called plasma (Miyamoto, 2000:1). The Earth and other planetary bodies such as stars and the solar systems are often surrounded by streams of energetic particles in the form of plasma trapped within their respective magnetic fields (Barth *et al*., 2003:466). According to Grill (1994:4), the average velocity of plasma particles in thermal equilibrium, v, depends on temperature, T, as given by equation 2.1,

$$v = \sqrt{\frac{K_B T}{m}}$$ **Equation 2.1**

where m [kg] is the mass of the particle, $K_B = 1.38 \times 10^{-23}$ [J/K] is Boltzmann's constant and T [K] is the temperature of the gas.

2.5.1 Plasma parameters

Plasma is described by parameters such as electron temperature, T_e, ion temperature, T_i, Debye length, λ_D, electron density, n_e, ion density, n_i, plasma frequency, ω_p, and plasma potential, V_p. These parameters will be discussed in detail in the following sections.

2.5.1.1 Energy transfer between electrons and heavy particles

In plasma (gaseous system), particles are always in motion which causes collisions among them. There are two types of collisions among particles in the plasma: elastic and inelastic collisions. Elastic collisions are collisions among electrons and heavy particles (neutral atoms, ions, neutral molecular fragments), and which do not result in excitation of the heavy particles (Grill, 1994:5). In this case, the energy transfer, E_{tr}, is given by (Grill, 1994:5−7),

$$E_{tr} = \frac{2m_e}{m_h}E \qquad \textbf{Equation 2.2}$$

where m_h [kg] is the mass of the heavy particles, m_e [kg] is the electron mass and E [J] is the energy of the electron.

Inelastic collisions are collisions among electrons and heavy particles, and which result in excitation, ionisation or dissociation of the heavy particles. In this case, the energy transfer is given by (Grill, 1994:5−7),

$$E_{tr} = \frac{m_h}{m_{in} + m_h}E \qquad \textbf{Equation 2.3}$$

where $m_{in} = m_e << m_h$ is the mass of particles losing energy.

After inelastic collisions between electrons and heavy particles, the electrons transfer most of their energy to the heavy particles. As a result, energetic plasma species are created. Heavy particles can also dissipate their energy to the surroundings through radiation.

2.5.1.2 Plasma temperature

Plasma is often described as a mixture of particles, each with different electric charge, mass and temperature (Grill, 1994:7). The plasma temperature represents the mean translational energy of the particle species in the plasma. It is characterised by the specific average temperature of different particle species such as the electron temperature, T_e, and the ion temperature, T_i (Grill, 1994:7−8). Moreover, heavy particle species can have several temperatures at the same time such as the excitation temperature, T_{ex}, the ionisation temperature, T_{ion}, dissociation temperature, T_d, and the radiation temperature, T_r. In order for the plasma to attain a thermal equilibrium state, all temperatures must be equal to one another as given by equation 2.4 (Grill, 1994:8),

$$T_{ex} = T_{ion} = T_d = T_r = T_e \, . \qquad \textbf{Equation 2.4}$$

Furthermore, in the thermal equilibrium state, the distribution of particle velocities is Maxwellian. The one-dimensional Maxwellian electron velocity distribution function, $F(v)$, is given by equation 2.5 (Chen, 1984:4),

$$F(v) = B \cdot exp\left(-\frac{\frac{1}{2} m_e v^2}{K_B T_e} \right) . \qquad \textbf{Equation 2.5}$$

The constant B is related to the electron density, n_e, by equation 2.6 (Chen, 1984:4; Miyamoto, 2000:7),

$$B = n_e \left(\frac{m_e}{2\pi K_B T_e} \right)^{1/2} , \qquad \textbf{Equation 2.6}$$

$$n_e = \int_{-\infty}^{\infty} F(v) dv \, . \qquad \textbf{Equation 2.7}$$

Figure 2.3 represents a typical Maxwellian electron velocity distribution. This distribution is often characterised by the temperature of the electrons.

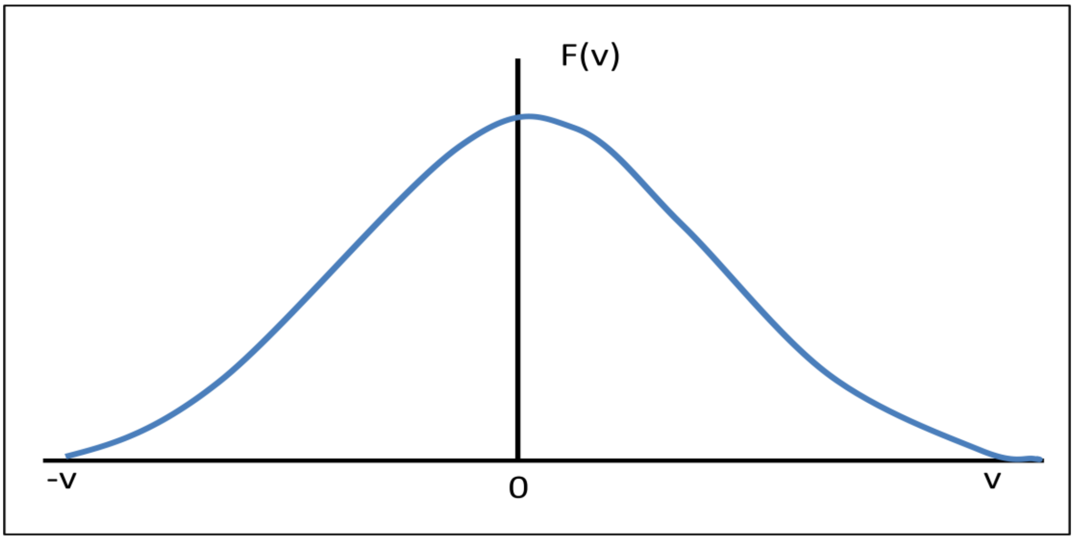

Figure 2.3: Schematic representation of the Maxwellian electron velocity distribution (Adapted from Chen, 1984:5; Sinclair, 2005:4)

The average kinetic energy of the electrons (E_{kav}) in the velocity distribution (Figure 2.3) is given by equation 2.8 (Chen, 1984:5; Sinclair, 2005:4),

$$E_{kav} = \frac{1}{2} K_B T_e \; . \qquad \textbf{Equation 2.8}$$

Similarly, the Maxwellian distribution of electron velocity can be extended to three dimensions and the average kinetic energy of the electrons is given by equation 2.9,

$$E_{kav} = \frac{3}{2} K_B T_e \; . \qquad \textbf{Equation 2.9}$$

The conversion of one electron volt (eV) to electron temperature, T_e, is given by equation 2.10 (Sinclair, 2005:5),

$$K_B T_e = 1\,\text{eV} = 1.6 \times 10^{-19}\ \text{J}, \qquad \textbf{Equation 2.10}$$

$$T_e = \frac{1\ \text{eV}}{K_B} = 11604\ \text{K}.$$

2.5.1.3 Debye length

Another important parameter, related to plasma, is the Debye length, λ_D. Consider the situation where two oppositely charged probes are immersed in the plasma; electrons will be attracted to the positively charged probe while ions will move towards the negatively charged probe. This creates a sheath (clouds of particles) around the probes and, hence, prevents an electric field from forming inside the plasma. This phenomenon is known as Debye shielding (Sinclair, 2005:2). The thickness of the sheath (Debye length) depends on the electron density and the electron temperature, as given by equation 2.11 (Grill, 1994:12−13; Düsterer, 2002:21),

$$\lambda_D = \sqrt{\frac{\varepsilon_o K_B T_e}{n_e e^2}} \; . \qquad \textbf{Equation 2.11}$$

where e is the unit electron charge

In the quasi-neutral state of the plasma, the electron density and the ion density are always equal (Grill, 1994:5; Asselin, 2011:20). From equation 2.11, when n_e increases, λ_D decreases. This is because there are more electrons inside every layer of the plasma (Chen, 1984:10). Furthermore, if the particles are more energetic, the Debye length will increase and the screening effect will be felt further away from the probes.

Debye shielding is only valid if there is a sufficient number of particles, N_P, in the plasma (Grill, 1994:13). This shielding is caused by the large number of electrons in the Debye sphere. The number of electrons within the Debye sphere can be determined using equation 2.12 (Chen, 1984:11),

$$N_p = n_e \frac{4}{3} \pi \lambda_D{}^3 \ . \qquad \textbf{Equation 2.12}$$

2.5.1.4 Plasma sheath theory

Plasma sheath theory uses the Langmuir probe principle to model the current obtained from a probe immersed in a plasma. This principle provides two approximation methods that can be used to determine the characteristics of the plasma, namely the Orbital Motion Limited (OML) and the Thin Sheath Limited (TSL) approximations (Escobar, 2009:15). In the OML approximation, the plasma is tenuous and the Debye length is larger than the probe radius, $r_p << \lambda_D$ (Weyde, 2006:22; Escobar, 2009:15). Figure 2.4 shows the OML trajectory of particles around a probe. In this figure, the sheath distance is represented by a, the probe radius is represented by r_p, the radial component of the plasma velocity is represented by $\vec{u}$ and the tangential component of the plasma velocity is represented by $\vec{v}$.

In the TSL approximation, the plasma is very dense and the Debye length is much smaller than the probe radius, $r_p >> \lambda_D$ (Weyde, 2006:22).

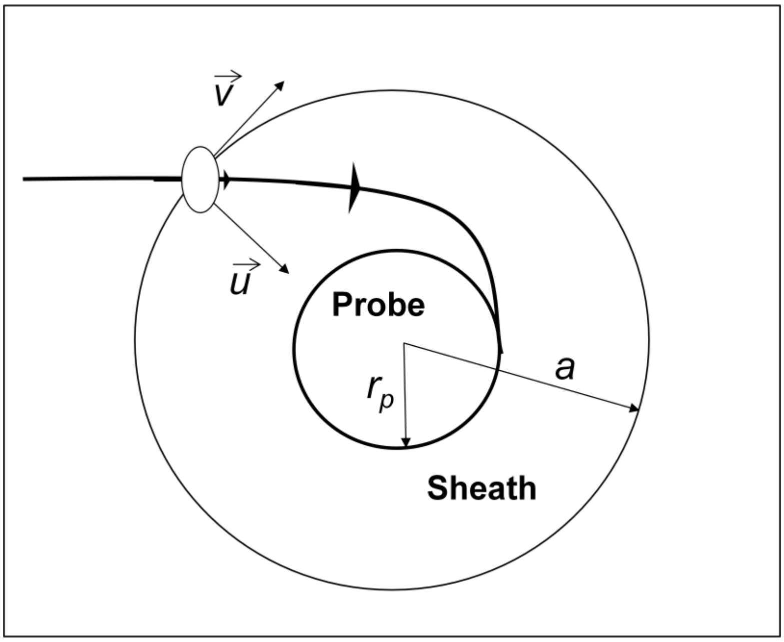

Figure 2.4: Schematic representation of the particle trajectory in the orbital motion limited approximation (Adapted from Escobar, 2009:15)

As shown in Figures 2.5 and 2.6, the VARB is located just above the ionosphere, at an altitude of approximately 1000 km above the Earth's surface. The typical electron density in the VARB is between 10^6 m^{-3} and 10^{10} m^{-3} and the electron temperature is between 1 eV and 2 eV (Weyde, 2006:23; Kotova, 2007:409). Near the VARB, there is a torus-shaped region known as the plasmasphere. The plasma in this region is extremely dense with a peak density of 10^{10} m^{-3} and cold temperature of approximately 1 eV (Weyde, 2006:23; Kotova, 2007:409). The characteristic densities of the plasma covered in this study falls within that of the ionosphere (F-layer) region and the plasmasphere region. When comparing the Debye length (3.8 mm) used in the ionosphere region to the spherical probes radii (30 mm, 35 mm and 40 mm) used in the present study, the Debye length is much smaller than the probe radii, i.e., $\lambda_D << r_p$. Thus, the current entering the probe immersed in the ionosphere region can be determined using the TSL approximation. However, in the plasmasphere region, the spherical probe radii is smaller than the Debye length (74.3 mm), i.e., $r_p << \lambda_D$. Therefore, the current entering the probe immersed in the plasmasphere region can be determined using the OML approximation. The characteristic Debye length of different regions around the VARB is listed in Table 2.1.

Table 2.1: **Plasma regions and characteristic Debye length (Adapted from Weyde, 2006:23; Escobar, 2009:38)**

Plasma regions	Electron density [m^{-3}]	Electron Temperature [eV]	Debye Length [m]
Ionosphere	10^{12}	≈ 0.26	3.8×10^{-3}
Plasmasphere	10^{10}	≈ 1	74.3×10^{-3}
Magnetosphere	10^7	≈ 500	52.3
Solar wind	5×10^6	≈ 10	10.5

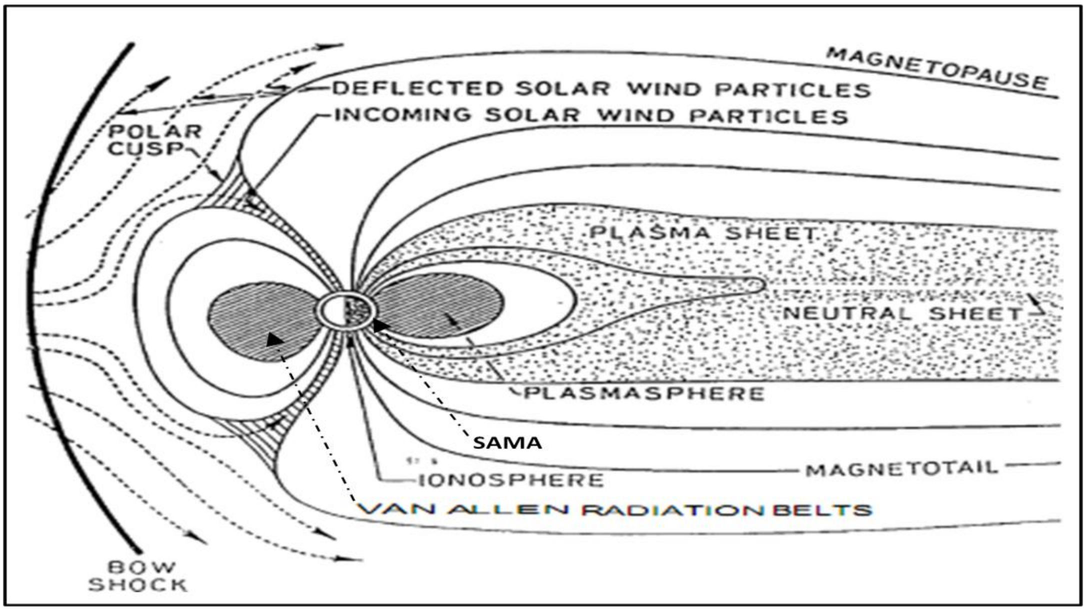

Figure 2.5: Schematic representation of the Earth's magnetosphere showing the ionosphere region (Adapted from Siingh *et al.*, 2005:638)

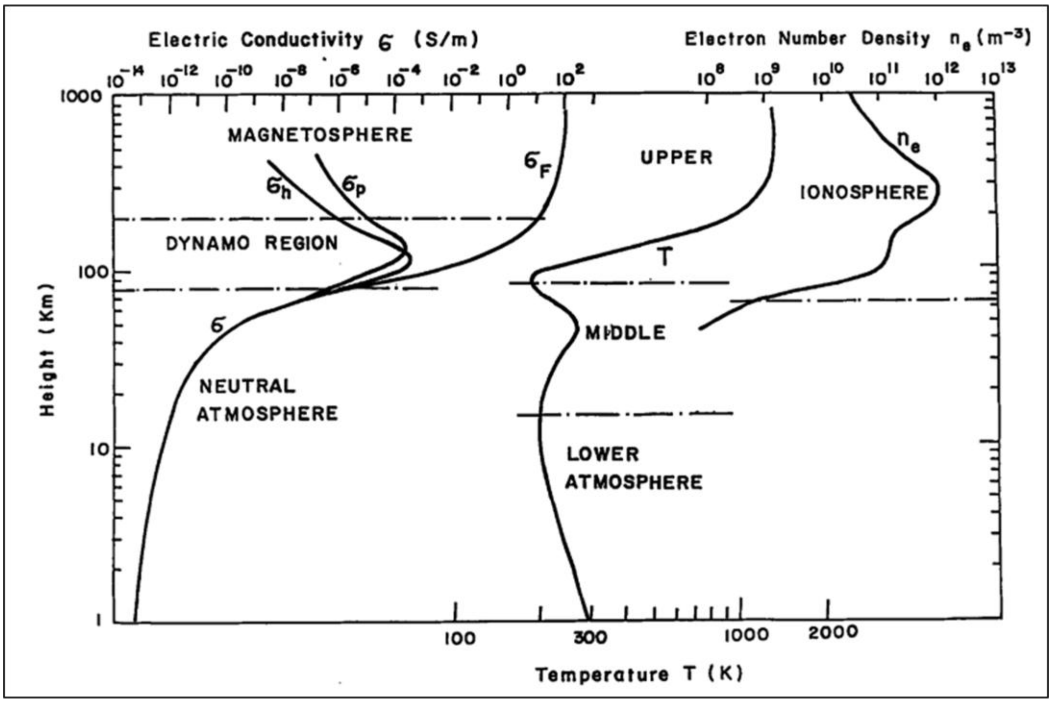

Figure 2.6: Schematic representation of the Earth's magnetosphere showing the electron density and the electron temperature (From Siingh *et al*., 2005:640)

2.5.1.5 Plasma frequency

When the charge neutrality within the plasma is perturbed, the electrons will respond faster than the ions to the electric forces created by the perturbation because of their small mass. The electrons' response to the perturbation is characterised by oscillations and the frequency at which they oscillate in the plasma is given by equation 2.13 (Grill, 1994:16; Miyamoto, 2000:8; Düsterer, 2002:21),

$$\omega_p = \left(\frac{n_e e^2}{m_e \varepsilon_o}\right)^{1/2}$$ **Equation 2.13**

where ω_p [rad/s] is the plasma frequency.

For an ionised gas to display the collective behaviour of plasma, the following conditions must be satisfied (Chen, 1984:12; Grill, 1994:13−17):

- The charged particles must be dense enough such that the Debye length is much smaller than the probe radius, i.e., $\lambda_D << r_p$.
- The number of particles within the Debye sphere must be much greater than one, i.e., $N_p >> 1$.
- The product of the frequency of the oscillating plasma and the mean time of collision between plasma and neutral atoms, τ, must be much greater than one, i.e., $\omega_p \tau >> 1$.

2.5.1.6 Plasma potential

The plasma potential, V_p, is the electric potential measured when a probe is immersed in the plasma. This potential is usually a small positive voltage measured at a position in the plasma with respect to the wall of the device producing the plasma. It can also be determined analytically using equation 2.14 (Merlino, 2007:1078-1080),

$$V_p = V_f - \left(\frac{K_B T_e}{e} \cdot ln \left(0.6 \cdot \sqrt{\frac{2\pi m_e}{m_i}} \right) \right) \qquad \textbf{Equation 2.14}$$

where V_f [V] is the floating probe potential and also the reference potential.

2.5.2 Plasma behaviour

Langmuir probes are usually used to collect current over a range of the applied probe voltage, V_b. The relationship between the probe voltage and the collected current from the probe is known as the current-voltage (*I*−*V*) characteristic curve. The *I*−*V* characteristic curve is sub-divided into three regions of operation, which are, the electron-retardation region (ERR), the ion-saturation region (ISR) and the electron-saturation region (ESR) (Asselin, 2011:31−32). While studying the *I*−*V* characteristic curve depicted in Figure 2.7, the plasma potential, V_p, can be determined within the ERR and ESR, while the floating probe potential, V_f, can be determined within the ISR and ERR. The floating probe potential, $V_f = 0$, represents the point where the ion current, I_i, and the electron current, I_e, tend to be in equilibrium, with the probe current, I_{probe}, equal to zero, i.e., $I_{probe}(V_b) = I_e(V_b) + I_i(V_b) = 0$ (Chen, 2003:2).

Figure 2.8 shows the *I*−*V* characteristic curves of the different Langmuir probes which are either spherical, cylindrical or planar probes (Asselin, 2011:34).

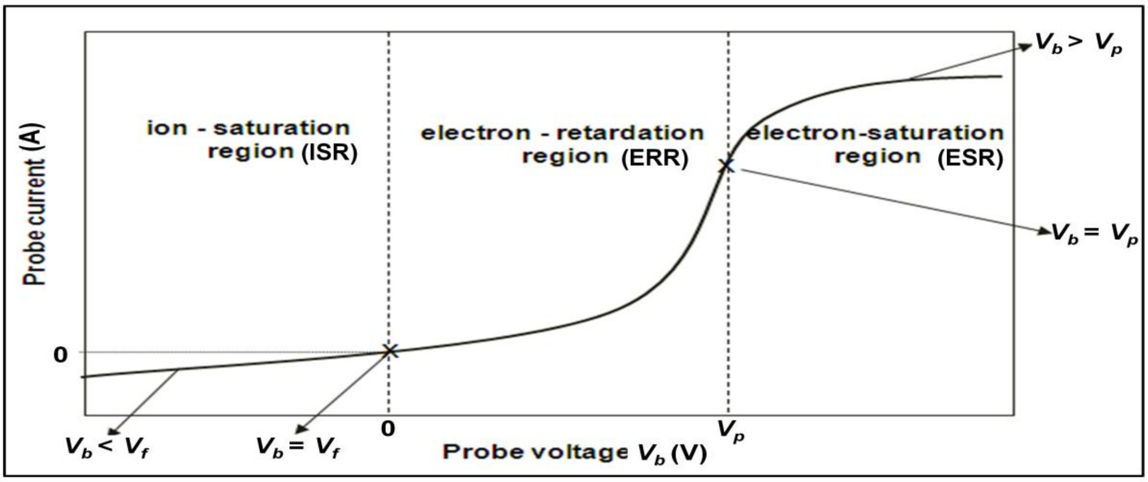

Figure 2.7: The typical Langmuir probe *I*−V characteristic curve (Adapted from Escobar, 2009:16)

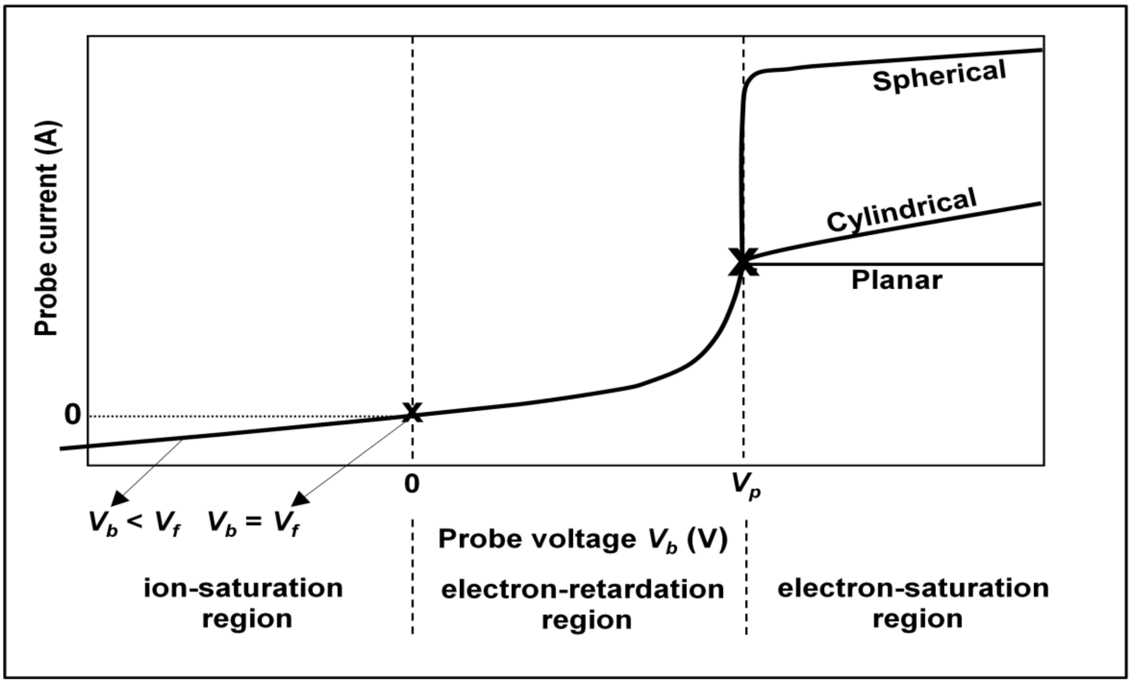

Figure 2.8: The different Langmuir probes' *I−V* characteristic curves (Adapted from Asselin, 2011:34)

Furthermore, when the Langmuir probe is immersed in the plasma and a probe voltage is applied to its surface, a plasma sheath is formed (Merlino, 2007:1081). This sheath is formed as a result of a concentration of charged particles around the probe (section 2.5.1.3). The charged particles that are extracted from the plasma contribute to shielding the surrounding electric field near the probe surface (Sinclair, 2005:2; Asselin, 2011:20). Actually, the probe is constantly exposed to the surrounding electrons and ions when immersed in the plasma. However, electrons reach the probe faster, because of their smaller mass and higher velocity, when compared to ions. As a result, the probe is initially negatively charged and its potential is below the potential of the surrounding plasma.

- When the applied probe voltage is less than the floating probe potential, $V_b < V_f$, electrons (negatively charged) are repelled from the probe and ions are attracted to the probe over a given time. As a result, the ion current becomes stronger as the probe voltage decreases along the *I−V* characteristic curve, with the current defined in the conventional direction that positive charge flows. Therefore, the probe current becomes negative and the probe produces an ion-saturation current, I_{isat} (Lyons, 2007:16−17; Deline, 2008:16; Hannum, 2010:31−32; Asselin, 2011:20). The region where there is only ion current is called the ISR (Figure 2.7) (Barjatya, 2007:4; Escobar, 2009:16).

- When the applied probe voltage reaches the floating probe potential, $V_b = V_f$, the number of electrons is equal to the number of ions , i.e., $n_e = n_i$.

- On the other hand, when the probe is positively charged and the applied probe voltage exceeds the floating probe potential, $V_b > V_f$, electrons are attracted to the probe and ions are repelled from the probe. As a result, the ion current becomes weaker as the probe voltage increases along the $I-V$ characteristic curve. Therefore, the probe current becomes positive. The region where the electron current dominates the ion current is called the ERR (Figure 2.7) (Hannum, 2010:31−32).

- When the applied probe voltage reaches the potential of the surrounding plasma, $V_b = V_p$, the electron current almost equals the currents in the surrounding plasma. Hence, the electron current becomes stronger as the probe voltage increases along the $I-V$ characteristic curve. When the applied probe voltage exceeds the plasma potential, $V_b > V_p$, all ions are repelled from the probe and only the electrons are attracted to the probe. Therefore, the probe current is positive and the probe produces an electron-saturation current, I_{esat}. The region where there is only electron current is called the ESR (Figure 2.7) (Escobar, 2009:16; Hannum, 2010:31−32).

2.5.3 Probe current collection

Langmuir probes can be used to collect current if the probe is immersed in the plasma. If a planar probe is positioned along the xz-plane, the current collected will originate from the particles travelling in the y-direction only (Figure 2.9). The collected current depends on the rate at which electrons and ions hit the probe. The electron current generated from the planar probe depends on the average velocity of electrons hitting the probe, the probe surface area, the electron charge and the electron density, as given by equation 2.15 (Sirajuddin, 2007:5),

$$I = A_p \sum_i e n_e v_y \qquad \textbf{Equation 2.15}$$

where A_p [m^2] is the probe surface area and v_y [m/s] is the average velocity of electrons travelling in the y-direction.

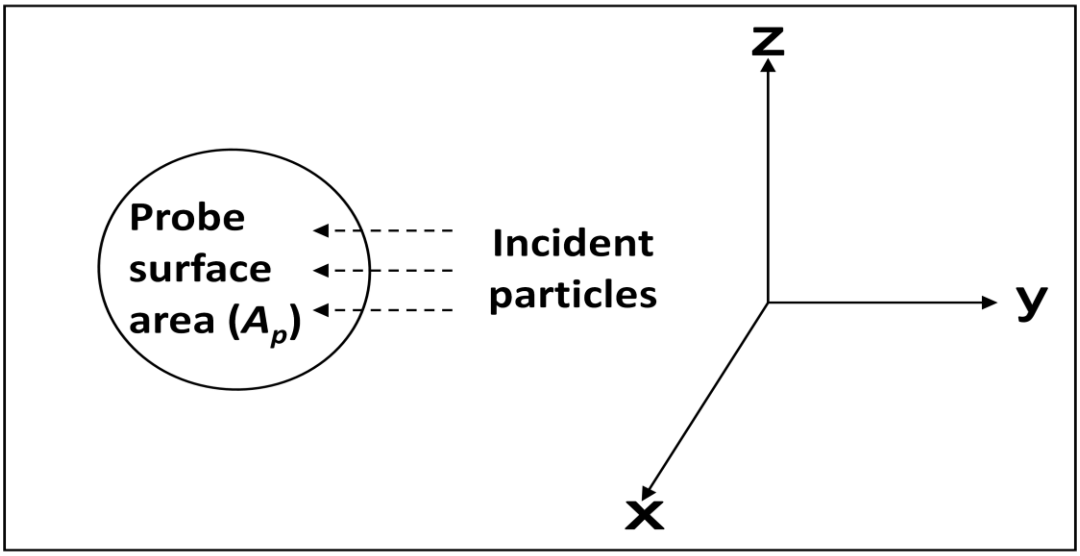

Figure 2.9: Representation of the incident particles travelling in the y-direction towards the probe surface area (Adapted from Sirajuddin, 2007:5)

In order to find the average velocity of electrons flowing towards the planar probe, a normalised Maxwellian electron distribution function describes the velocity of electrons in the plasma, as given by equation 2.16 (Sirajuddin, 2007:5),

$$\mathrm{F}(\vec{v}) = \left(\frac{m_e}{2\pi K_B T_e}\right)^{3/2} \cdot exp\left(-\frac{\frac{1}{2} m_e |\vec{v}|^2}{K_B T_e}\right). \qquad \textbf{Equation 2.16}$$

When the velocity vector, $\vec{v}$, is separated into its Cartesian components, such that $\vec{v} = v\vec{x} + v\vec{y} + v\vec{z}$ and $d\vec{v} = d\vec{v}_x d\vec{v}_y d\vec{v}_z$, the expected velocity of electrons travelling in the y-direction with reference to the xz-plane is given by equation 2.17 (Sinclair, 2005:20; Sirajuddin, 2007:5),

$$v_y = \frac{\int_{-\infty}^{\infty}\int_{-\infty}^{\infty}\int_{v_{min}}^{\infty} \vec{v}_y \, \mathrm{F}(\vec{v}) \, d\vec{v}_y d\vec{v}_x d\vec{v}_z}{\int_{-\infty}^{\infty} \mathrm{F}(\vec{v}) \, d\vec{v}} \qquad \textbf{Equation 2.17}$$

where $\mathrm{F}(\vec{v})$ is the normalised Maxwellian electron velocity distribution function.

Furthermore, the normalised Maxwellian electron distribution function (equation 2.16) becomes y-dependent after integrating with respect to all electron velocities in the x- and z-directions. This function is then multiplied by v_y and integrated over all electron velocities that can reach the probe. However, the energy and the velocity of electrons that can reach the probe surface must be greater than or equal to the potential energy difference created by the probe voltage, V_b, and the plasma potential, V_p, as given by equation 2.18 (Sirajuddin, 2007:6),

$$\frac{1}{2} m_e {v_{min}}^2 = e\left(V_b - V_p\right) . \qquad \textbf{Equation 2.18}$$

Consequently, the required minimum velocity (v_{min}) needed by an electron to reach the probe surface is given by equation 2.19,

$$v_{min} = \left(\frac{2e(V_b - V_p)}{m_e}\right)^{1/2} . \qquad \textbf{Equation 2.19}$$

Since the Maxwellian electron velocity distribution function is normalised, the integral in the denominator of equation 2.17 is reduced to one. Thus, the expected velocity vector of electrons travelling in the y-direction with reference to the xz-plane is given by equation 2.20 (Sirajuddin, 2007:6),

$$v_y = \int_{-\infty}^{\infty} \int_{-\infty}^{\infty} \int_{v_{min}}^{\infty} \vec{v}_y \, \mathrm{F}(\vec{v}) \, d\vec{v}_y d\vec{v}_x d\vec{v}_z \ . \qquad \textbf{Equation 2.20}$$

Substituting equation 2.16 into equation 2.20 and evaluating the final integral over all electron velocities with respect to $\vec{v}_x$ and $\vec{v}_z$ give the expected average velocity of electrons travelling in the y-direction (equation 2.21) (Sirajuddin, 2007:7),

$$v_y = \left(\frac{K_B T_e}{2\pi m_e}\right)^{1/2} \cdot exp\left(-\frac{e(V_b - V_p)}{K_B T_e}\right) . \qquad \textbf{Equation 2.21}$$

Inserting the result of equation 2.21 into equation 2.15, and changing variables give the electron current to probe voltage relationship (equation 2.22) (Sirajuddin, 2007:7),

$$I_e = I_{esat} \cdot exp\left(\frac{e(V_b - V_p)}{K_B T_e}\right) \qquad \textbf{Equation 2.22}$$

where I_{esat} is given by equation 2.23 (Sirajuddin, 2007:7; Hannum, 2010:33),

$$I_{esat} = A_p n_e e \cdot \left(\frac{K_B T_e}{2\pi m_e}\right)^{1/2} . \qquad \textbf{Equation 2.23}$$

Likewise, the ion current to probe voltage relationship is given by equation 2.24 (Merlino, 2007:1079),

$$I_i = -I_{isat} \cdot exp\left(\frac{e(V_p - V_b)}{K_B T_i}\right)$$ **Equation 2.24**

where I_{isat} is given by equation 2.25 (Sirajuddin, 2007:7; Merlino, 2007:1079),

$$I_{isat} = exp(-1/2) A_p n_i e \cdot \left(\frac{K_B T_e}{m_i}\right)^{1/2}$$ **Equation 2.25**

where $exp(-1/2) = 0.6$ is the Bohm ion current coefficient.

Furthermore, since the electron-saturation current can be found along the ERR, the natural logarithm of the electron current to probe voltage relationship (equation 2.22) gives (Sirajuddin, 2007:8),

$$ln(I_e) = ln\left(A_p n_e e \cdot \left(\frac{K_B T_e}{2\pi m_e}\right)^{1/2}\right) + \frac{e(V_b - V_p)}{K_B T_e} .$$ **Equation 2.26**

If two arbitrary current values, say I_1 and I_2, are selected in the ERR, the difference between the two currents, $I_1 - I_2$, allows electron temperature, T_e, to be expressed in units of K and eV as given by equations 2.27 and 2.28 (Sirajuddin, 2007:8),

$$T_e = \frac{e}{K_B} \cdot \frac{V_1 - V_2}{ln(I_1/I_2)}$$ **Equation 2.27**

where T_e is expressed in K, and

$$T_e = \frac{e(V_1 - V_2)}{ln(I_1/I_2)}$$ **Equation 2.28**

where T_e is expressed in eV.

In addition, solving for the electron density, n_e, in equation 2.23, yields (Sirajuddin, 2007:9),

$$n_e = \left(\frac{I_{esat}}{A_p e}\sqrt{\frac{2\pi m_e}{K_B T_e}}\right)$$ **Equation 2.29**

where I_{esat} is expressed in A, T_e is expressed in eV and m_e is expressed in kg.

Likewise, solving for the ion density, n_i , in equation 2.25, yields (Sirajuddin, 2007:9),

$$n_i = \left(\frac{I_{isat}}{exp(-1/2) A_p e} \sqrt{\frac{m_i}{K_B T_e}} \right) \qquad \textbf{Equation 2.30}$$

where I_{isat} is expressed in A, n_i is expressed in m^{-3} and m_i is expressed in kg.

2.6 Langmuir probe measurement methods

The first scientific instrument which was used to measure plasma parameters such as electron density, ion density and electron temperature was an electric probe instrument. The probe was first introduced by Irving Langmuir to measure and analyse the ambient plasma parameters (Lyons, 2007:19; Merlino, 2007:1078). The Langmuir probe instrument operates by applying a voltage to a conducting metal immersed in the plasma and recording the measured *I−V* curve (Barjatya, 2007:3; Lyons, 2007:11). The *I−V* curve can be used for the evaluation of the plasma parameters mentioned above (Hamzavi *et al*., 1996:207).

Based on a Maxwellian electron velocity distribution, a variety of techniques are used to determine the plasma conditions. One of these techniques is the Langmuir single probe technique. In this method, a swept bias voltage is applied to a single probe immersed in the plasma over a range that is comparable to the electron temperature and the current is measured. The single probe current is measured repeatedly at a particular position in space (Lyons, 2007:21). In the second technique, the bias voltages applied to two probes are swept relative to another. This technique is known as the double probe method.

The third technique is the Langmuir triple probe method. This technique includes the double probes and a floating probe, which are operated simultaneously. By applying a fixed bias voltage between the double probes, the electron density is determined. Likewise, the electron temperature is determined by measuring the potential difference between the double probes and the third probe (floating probe) (Lyons, 2007:22). In addition, the ion-saturation current and the floating probe potential outputs can be determined as well. The reason why the Langmuir triple probe technique is commonly used over other methods is because it does not require storage and post processing of *I−V* data after measurement. This technique allows the plasma parameters to be displayed on appropriate display units (Chen & Sekiguchi, 1965:2374). The disadvantage of this method is that all the three probes must have the same plasma conditions, even when there are turbulent fluctuations (Lyons, 2007:22). Figure 2.10 shows the schematic diagram of a single probe system, while Figure 2.11 contains the schematic diagram of the triple probe circuit showing the applied bias voltages.

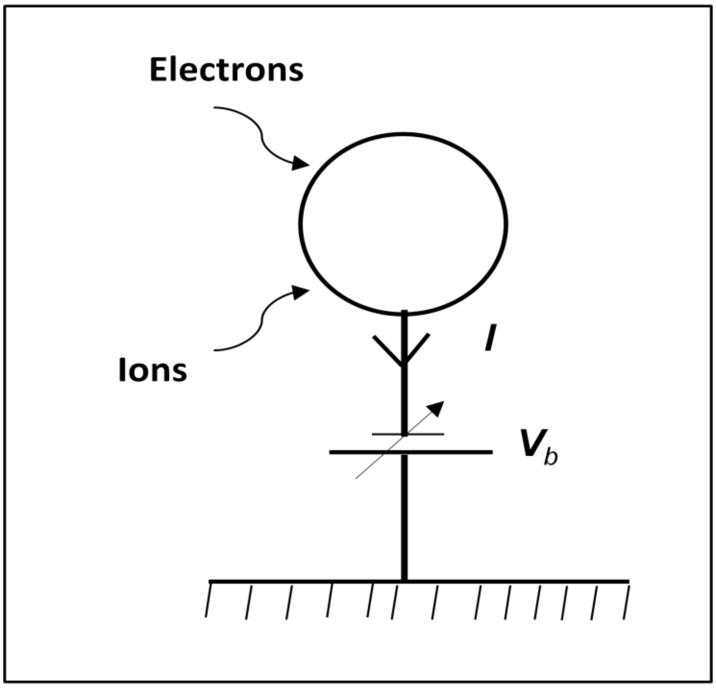

Figure 2.10: Schematic diagram of a single probe with the bias voltage (Adapted from Hamzavi *et al*., 1996:208)

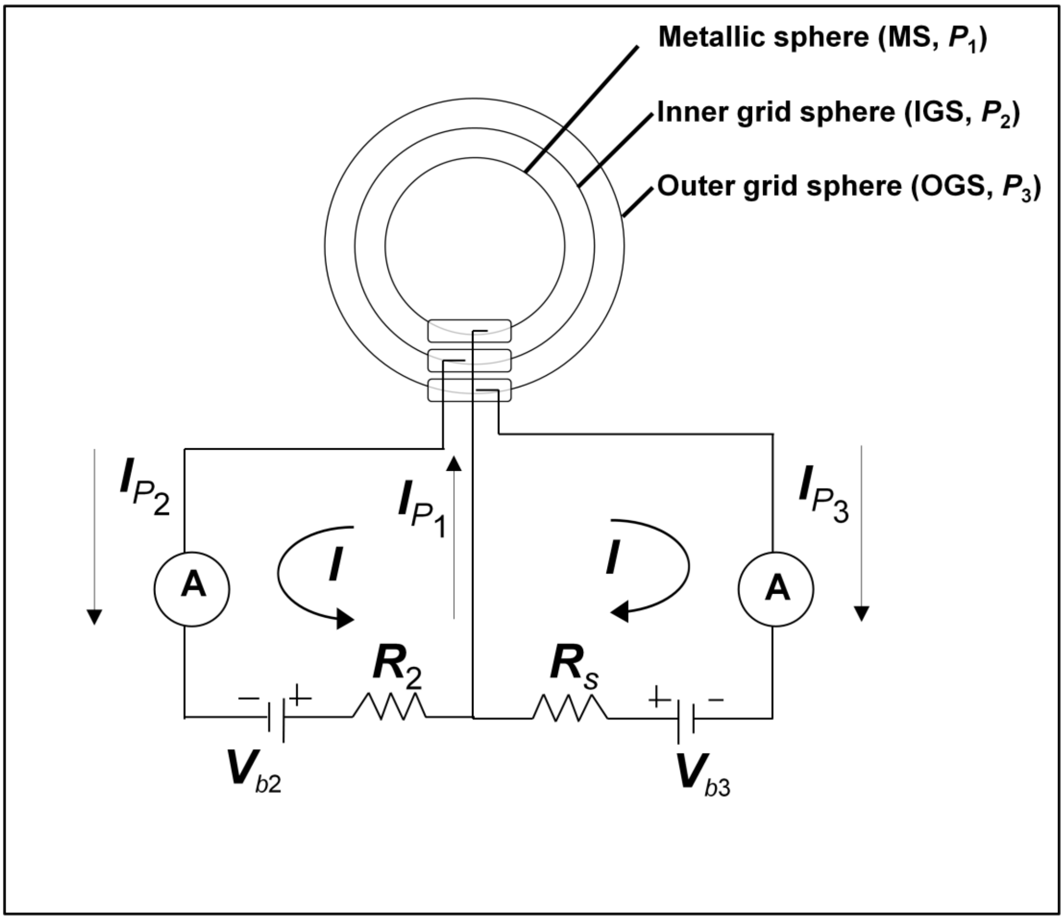

Figure 2.11: Schematic diagram of the triple probe circuit showing the external bias voltages, V_{b2} and V_{b3} (Adapted from Chen & Sekiguchi, 1965:2364; Ji *et al*., 1991:2328)

In the present study, only Langmuir triple probe method is considered, hence, the single or double probe methods are not described.

- **Langmuir triple probe method**

Chen & Sekiguchi (1965:2366) describe the Langmuir triple probe (symmetric and asymmetric) method as a direct technique for the measurement of plasma parameters. In this study, the asymmetric triple probe technique is the underlying theory considering that the spherical probes had different diameters. Applying this technique, a plasma sheath is formed when a probe surface is immersed in the plasma. The formation of this sheath is due to the attraction of unlike charges and the repulsion of like charges. The Langmuir asymmetric triple probe technique can be implemented when placing the metallic sphere (MS), the inner grid sphere (IGS) and the outer grid sphere (OGS) in close proximity in the plasma. These probes (spheres) consist of unequal surface areas ($A_{p1} \neq A_{p2} \neq A_{p3}$) and are, respectively, represented by P_1, P_2 and P_3 (Figure 2.11). In order to determine the plasma parameters such as electron temperature and electron density with the asymmetric triple probe, the following scenarios are considered.

- ***V_{b2}, V_{b3}* = 0**

Considering Figures 2.11 and 2.12, if no external bias voltage is applied to probes P_2 and P_3, their potentials will be at the floating probe potential and no current will flow into them. As a result, plasma parameters cannot be measured (Chen & Sekiguchi, 1965:2364).

- ***V_{b2}, V_{b3}* ≠ 0**

When two external negative bias voltages, V_{b2} and V_{b3}, are applied to probes P_2 and P_3 and the probe currents (I_{P_1}, I_{P_2} and I_{P_3}) flow in the direction of probe P_1, as shown in Figure 2.11, the potentials of probes P_2 and P_3 (negative) will be below the floating probe potential (Figure 2.12) and the current flowing into these probes (P_2 and P_3) will mainly be the ion current. Conversely, the potential of probe P_1 (positive) will be above the floating probe potential. In this case, the conventional current direction is considered and the current flowing into probe P_1 will mainly be the electron current (Chen & Sekiguchi, 1965:2364). Figure 2.12 illustrates the voltage potentials of the three probes (P_1, P_2 and P_3).

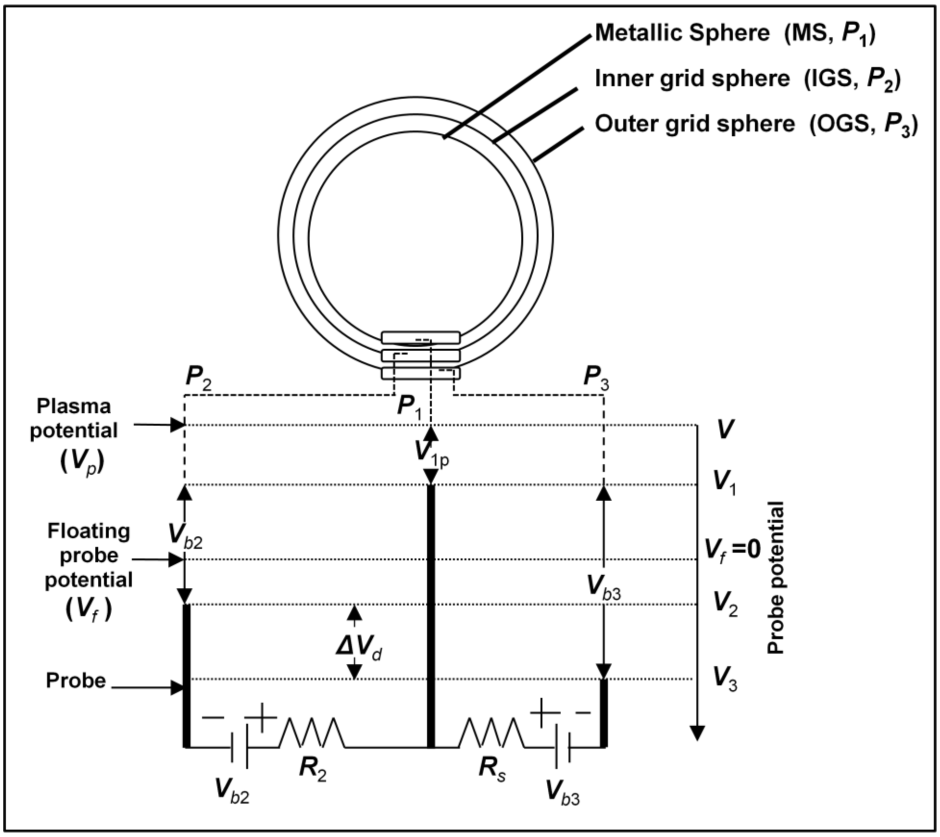

Figure 2.12: Schematic diagram describing the voltage potentials of the three probes (Adapted from Chen & Sekiguchi, 1965:2364; Ji *et al*., 1991:2328)

- **Probe voltage**

Considering Figures 2.11 and 2.12, there will be a voltage drop over resistors R_s and R_2 when current flows through them. However, these resistors are very small, and with small current, the voltage drop over them will be much smaller than the bias voltages. As a result, the voltages across the resistors can be ignored. Therefore, the potential differences of the externally applied probe voltages, V_{b2} and V_{b3}, are given by equations 2.31 and 2.32 (Chen & Sekiguchi, 1965:2364; Ji *et al*., 1991:2328),

$$V_{b2} = V_1 - V_2 \qquad \textbf{Equation 2.31}$$

$$V_{b3} = V_1 - V_3 \qquad \textbf{Equation 2.32}$$

where V_1 is the voltage potential at probe P_1, V_2 is the voltage potential at probe P_2 and V_3 is the voltage potential at probe P_3.

- **Probe current**

Considering Figure 2.11, the current at probe P_1 is given by equation 2.33 (Chen & Sekiguchi, 1965:2364),

$$I_{P_1} = I_{P_2} + I_{P_3} \qquad \textbf{Equation 2.33}$$

where I_{P_1} is the MS current, I_{P_2} is the IGS current and I_{P_3} is the OGS current.

The current entering each probe is given by equations 2.34, 2.35 and 2.36 (Chen & Sekiguchi, 1965:2365; Kelly *et al*., 1990:2; Deline, 2008:21),

$$I_{P_1} = I_1 = A_{p_1} J_{esat} exp\left(-\phi V_1\right) - A_{p_1} J_{isat}\left(V_1\right) \qquad \textbf{Equation 2.34}$$

$$I_{P_2} = I_2 = -A_{p_2} J_{esat} exp\left(-\phi V_2\right) + A_{p_2} J_{isat}\left(V_2\right) \qquad \textbf{Equation 2.35}$$

$$I_{P_3} = I_3 = -A_{p_3} J_{esat} exp\left(-\phi V_3\right) + A_{p_3} J_{isat}\left(V_3\right) \qquad \textbf{Equation 2.36}$$

where $\phi = e/K_B T_e$, and A_{p_1}, A_{p_2} and A_{p_3} are the surface areas of probes P_1, P_2 and P_3, expressed in m^2, J_{isat} is the ion-saturation current density and J_{esat} is the electron-saturation current density. The electron-saturation current density can be determined by equation 2.37 (Chen & Sekiguchi, 1965:2365; Eckman, 1999:22; Deline, 2008:21),

$$J_{esat} = n_e e \left(\frac{K_B T_e}{2\pi m_e}\right)^{1/2} . \qquad \textbf{Equation 2.37}$$

The ion-saturation current density is given by equation 2.38 (Chen & Sekiguchi, 1965:2366),

$$J_{isat} = \exp\left(-1/2\right) e n_e \left(\frac{K_B T_e}{m_i}\right)^{1/2} . \qquad \textbf{Equation 2.38}$$

- **$V_{b3} \neq 0$ and $I_{p2} = 0$**

As shown in Figure 2.13, an external negative voltage, V_{b3}, is applied to probe P_3 to collect ion-saturation current, with most of the electrons being repelled. The current flowing from probes P_3 to P_1, can be determined by measuring the voltage across the shunt resistor (R_s). When measuring this current, there may be a possibility of some voltage offset. Furthermore, probe P_2 is electrically floating because there is no external voltage applied to the probe. When probes P_1 and P_2 are at the same potential, they will collect the same number of electrons and ions (Mackel *et al*., 2013:2).

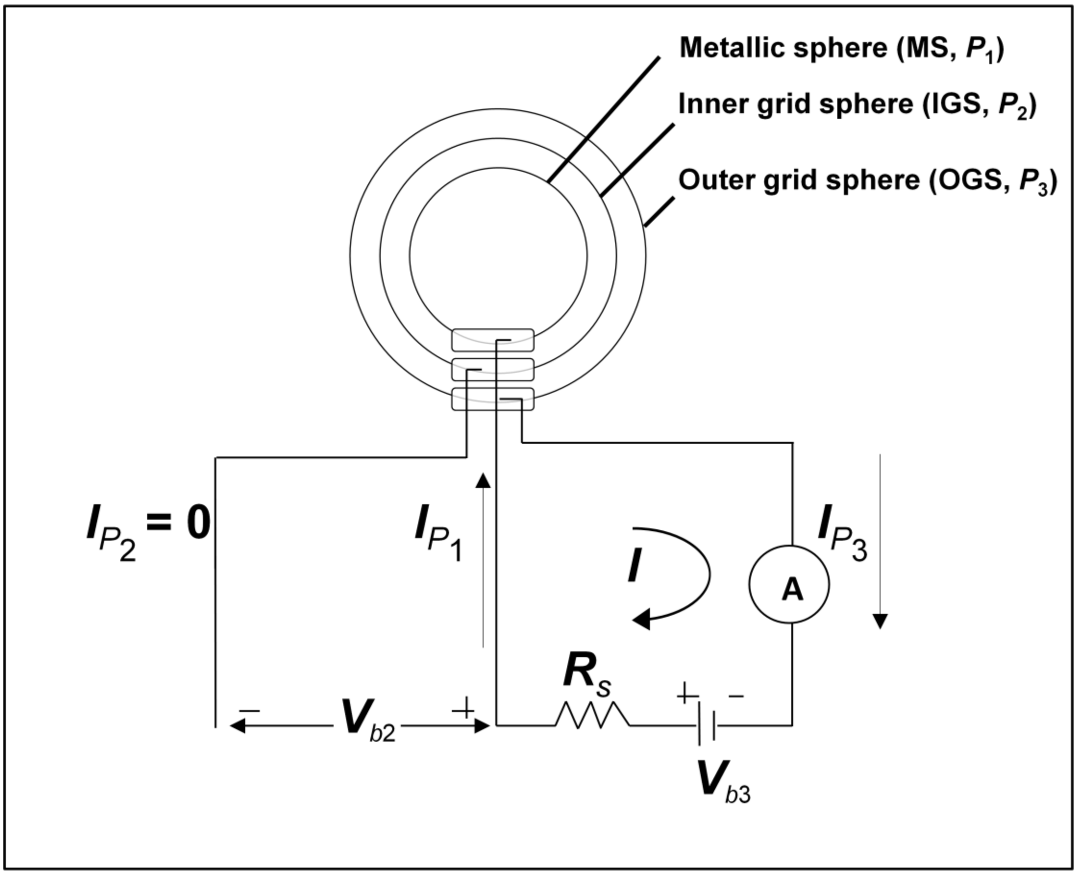

Figure 2.13: Schematic diagram of the Langmuir triple probe direct display system (Adapted from Chen & Sekiguchi, 1965:2366; Tilley *et al*., 1994:679; Eckman, 1999:21; Pace, 2009:26)

- **Probe current**

From Figure 2.13, the probe voltage at probe P_2 is electrically floating and no current will flow into the probe i.e., $I_{P_2} = 0$. Substituting I_{P_2} by its value into equation 2.33, the current flowing through probes P_3 and P_1 becomes equal, i.e., $I_{P_1} = I_{P_3} = I$ (Chen & Sekiguchi, 1965:2366; Ji *et al*., 1991:2328; Eckman, 1999:22). Furthermore, the current entering each probe is given by equations 2.39, 2.40 and 2.41,

$$I_{P_1} = I_1 = A_{p_1} J_{esat} exp\left(-\phi V_1\right) - A_{p_1} J_{isat}\left(V_1\right)$$ **Equation 2.39**

$$I_{P_2} = I_2 = -A_{p_2} J_{esat} exp\left(-\phi V_2\right) + A_{p_2} J_{isat}\left(V_2\right) = 0$$ **Equation 2.40**

$$I_{P_3} = I_3 = -A_{p_3} J_{esat} exp\left(-\phi V_3\right) + A_{p_3} J_{isat}\left(V_3\right)$$ **Equation 2.41**

where V_1 and I_{P_1} are the bias voltage and collected current of the positive probe; V_2 and I_{P_2} are the bias voltage and collected current of the floating probe; V_3 and I_{P_3} are the bias voltage and collected current of the negative probe.

- **Determination of the electron temperature using asymmetric triple probe**

The asymmetric triple probe depicted in Figure 2.13 allows the measurement of electron temperature by measuring the voltage difference (V_{b2}) between probes P_2 and P_1 directly with an oscilloscope. In this figure, the surface area of probe P_3 is larger than the surface areas of probes P_2 and P_1. As a result, more ion current is collected and has to be compensated for by a higher electron current flowing to probe P_2 (floating probe). This leads to a higher measured voltage V_{b2} between probes P_2 and P_1. For an asymmetric triple probe, the relation between the measured voltage, V_{b2}, and the electron temperature, T_e, is given by equation 2.42 (Mackel *et al*., 2013:2),

$$\frac{1}{1+\frac{1}{r_p}} = \frac{exp\left(-\frac{eV_{b2}}{K_B T_e}\right)-1}{exp\left(-\frac{eV_{b3}}{K_B T_e}\right)-1} \qquad \textbf{Equation 2.42}$$

where $r_p = \frac{A_{p3}}{A_{p1}}$ is the ratio of the asymmetric triple probe areas.

- **Determination of the electron density using asymmetric triple probe**

For an asymmetric triple probe, the estimated electron density from the ion-saturation current is given by equation 2.43 (Mackel *et al*., 2013:2),

$$n_e = \left(\frac{I}{\left(A_{p_1} 0.5e\sqrt{\frac{K_B T_e}{m_i}}\right)\left(exp\left(\frac{eV_{b2}}{K_B T_e}\right)-1\right)} \right). \qquad \textbf{Equation 2.43}$$

In conclusion, the asymmetric triple probe technique discussed above can be used for the determination of plasma parameters such as electron temperature and electron density.

2.7 Ultraviolet radiation

The UV spectra consist of wavelengths from 10 nm to 400 nm and are subdivided into UVA, UVB, UVC, VUV and EUV, according to their wavelength, as shown in Table 2.2.

Table 2.2: Types of UV radiation (From Tobiska & Nusinov, 2000:388; Tobiska & Nusinov, 2005:5−10; Tobiska & Bouwer, 2006:347)

UV Types	Wavelength range (nm)	Energy per photon (eV)
UVA	315 to 400	3.94 to 3.10
UVB	280 to 315	4.43 to 3.94
UVC	100 to 280	12.4 to 4.43
VUV	10 to 200	124 to 6.20
EUV	10 to 121	124 to 10.25

The photoelectric effect is the process of emitting electrons from a metallic material surface when exposed to radiation of sufficient energy (Millikan, 1916:355−356; Aristov, 2009:171). When this material is bombarded with UV radiation, the factors that need to be considered are the frequency of the UV spectra, the intensity of the light (photons) and the type of material that is being radiated. However, the effect of UV radiation on the surface of a material mainly depends on the frequency of the UV light (quantum theory). In addition, the intensity of the UV light only increases the amount of electrons that are being knocked out of the surface of the material (Millikan, 1916:355−356; Cox, 1996:9; Zettili, 2009:10−11).

The energy of light (photon energy) depends on its frequency (Millikan, 1916:355). This energy must exceed the binding energy of electrons inside the material. The binding energy is the minimum energy needed for electrons to escape the surface of a material and it is called the work function, Φ (Cox, 1996:9; Rae, 2002:2; Zettili, 2009:11−12). Table 2.3 lists the work function of metals and the maximum wavelength required for the onset of the photoelectric effect.

Table 2.3: Work function of metals and the maximum wavelength required for the onset of the photoelectric effect (Bell, 2013; HyperPhysics, 2013)

Metals	Work Function (eV)	Wavelength (nm)
Aluminium	4.08	304
Beryllium	5	248
Cadmium	4.07	305
Calcium	2.9	428
Carbon	4.81	258
Cesium	2.1	591
Cobalt	5	248
Copper	4.7	264
Gold	5.1	243
Iron	4.5	276
Lead	4.14	300
Magnesium	3.68	337
Mercury	4.5	276
Nickel	5.01	248
Niobium	4.3	289
Potassium	2.3	540
Platinum	6.35	196
Selenium	5.11	243
Silver	4.73	263
Sodium	2.28	545
Uranium	3.6	345
Zinc	4.3	289

- **Kinetic energy of the electrons**

When the UV light has more than the required minimum photon energy, E_{photon}, the additional energy is transferred to the ejected electrons as kinetic energy, $E_{K\ electrons}$, as given by equation 2.44 (Liboff, 1980:36; Cox, 1996:9; Rae, 2002:2),

$$E_{K\ electrons} = E_{photon} - \Phi_{material} = hf - \Phi_{material}$$ **Equation 2.44**

where $f = c/\lambda$ [Hz] is the photon frequency, $c = 3\ x\ 10^8$ [m/s] is the speed of light, λ [nm] is the wavelength, Φ [eV] is the work function and $h = 6.63 \times 10^{-34}$ is Planck's constant.

- **Stopping potential**

The stopping potential, V_{stop}, is the minimum applied voltage that exactly stops electrons from reaching the collector surface (Figure 2.14). When a source material is exposed to radiation of sufficient energy, electrons are ejected from the source material, and are collected by another conducting material. The stopping potential is applied to the collector with reference to the source material from which the electrons are ejected. This potential reduces the kinetic energy of the electrons to zero and is given by equation 2.45 (Millikan, 1916:356; Liboff, 1980:35),

$$V_{stop} = \frac{E_{K\ electrons}}{e} \qquad \textbf{Equation 2.45}$$

where $E_{K\ electrons}$ $[\mathrm{eV}]$ is the kinetic energy of the emitted electrons when ejected from the source material.

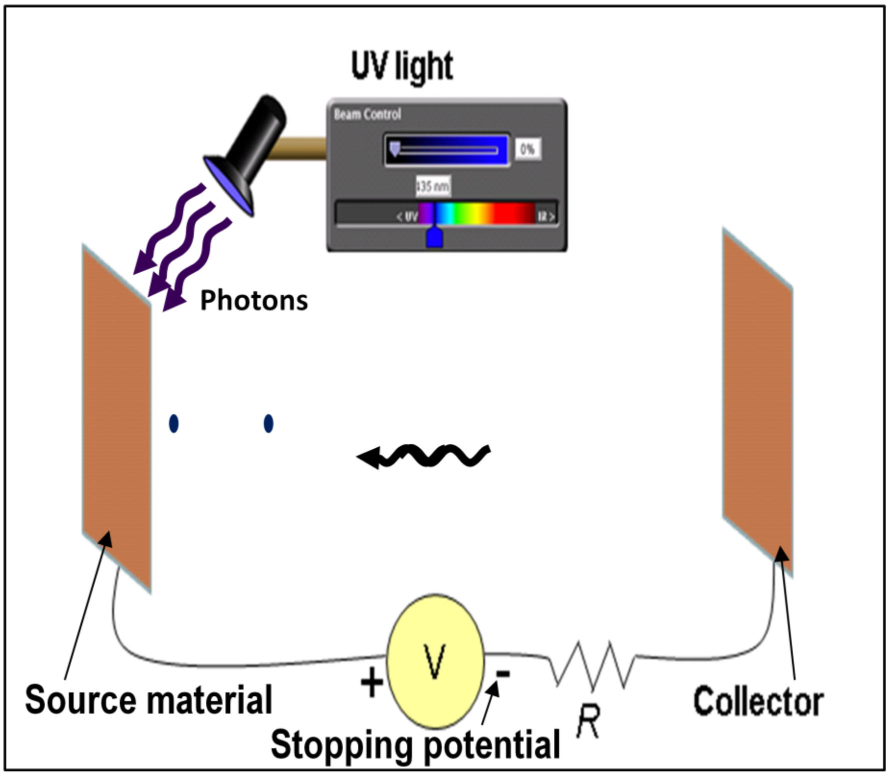

Figure 2.14: Schematic diagram describing incoming photons to the source material with a stopping potential applied to the collector and electrons are repelled

2.8 Spherical extreme ultraviolet and plasma spectrometer

2.8.1 Measurement principle of the SEPS sensor

The spherical extreme ultraviolet and plasma spectrometer (SEPS) sensor can be used to study the impact of solar activity events and the reactions of charged particles within the ionosphere and the Earth's upper atmosphere (Brunner *et al.*, 2011:3−5). The sensor designed by Brunner *et al*. (2011) implements the principle of the Langmuir probe and the principle of the photoelectric effect for the measurement of particles in the Earth's upper atmosphere. This sensor consists of three sets of isolated spheres, which are the MS, the IGS and the OGS. Each of these spheres is biased at different potentials by a variable DC power supply. For EUV radiation measurements, current is measured with different bias voltages applied to the MS, IGS and OGS. When a negative stopping voltage is applied to the IGS, the emitted electrons repelled by the MS are slowed down and when a positive voltage is applied to the OGS, these electrons are collected. The stopping voltage that slows down most of the emitted electrons reduces their kinetic energy. This voltage is again linked to the work function of the source material and the energy of the incoming photons. Therefore, when the stopping voltage is applied to the IGS and the attractive voltage applied to the OGS is swept, one can determine the particle flux and temperature. Figure 2.15 represents the schematic diagram describing incoming photons to the source material (MS) and electrons being dislodged and attracted to the positive bias collector (OGS).

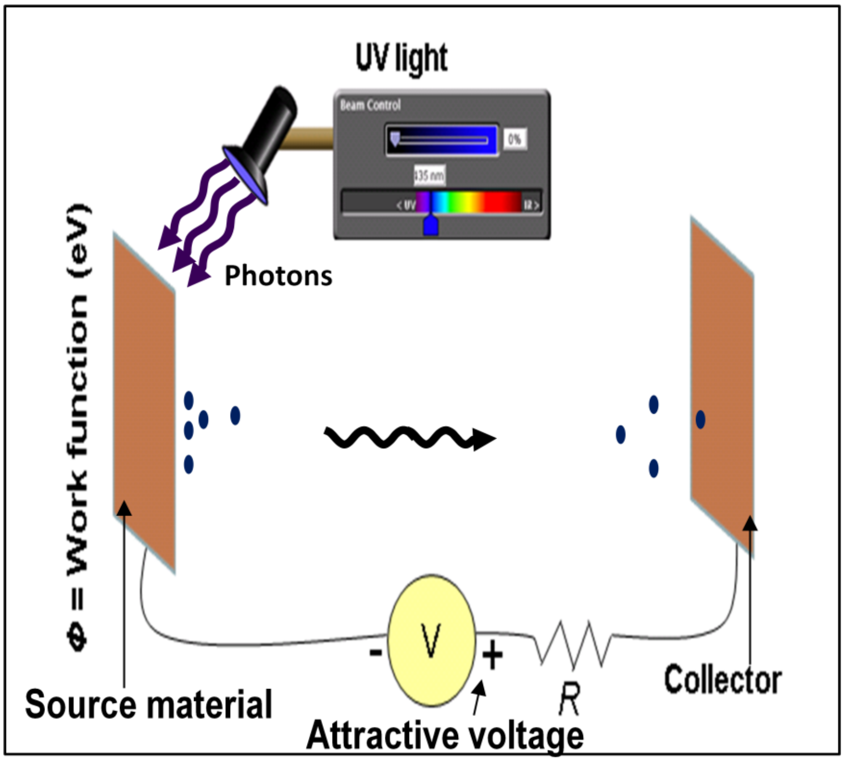

Figure 2.15: Schematic diagram describing incoming photons and electrons being dislodged from the source material and attracted to the collector

2.8.2 The SEPS sensor under EUV radiation

The SEPS sensor experimental setup reported in Brunner *et al*. (2011:5) uses a sensitive floating electrometer to measure current ranging between 100 pA and 10 µA. For EUV radiation measurements, the MS was biased from -70 V to +70 V so that when a high energy EUV light strikes the MS surface, the negative voltages would repel electrons and the positive voltages would re-attract the electrons to the MS. The IGS was biased at -50 V to slow down most of the electrons repelled by the MS and the OGS was biased at +50 V to collect these electrons (Brunner *et al.,* 2011:6). Photo electron current measurements are recorded as these electrons reach the OGS. Furthermore, the electron current obtained as a result of the absorption of photons in the MS helps in generating UV and EUV irradiance data (Brunner *et al.,* 2009:9). In the present study, the main goal is to investigate the flux and energy of electrons (0 to 25 eV) in the SAMA region. Additionally, the sensor prototypes developed are biased at voltages ranging between -25 V and +25 V. Figure 2.16 represents the schematic design of the SEPS sensor.

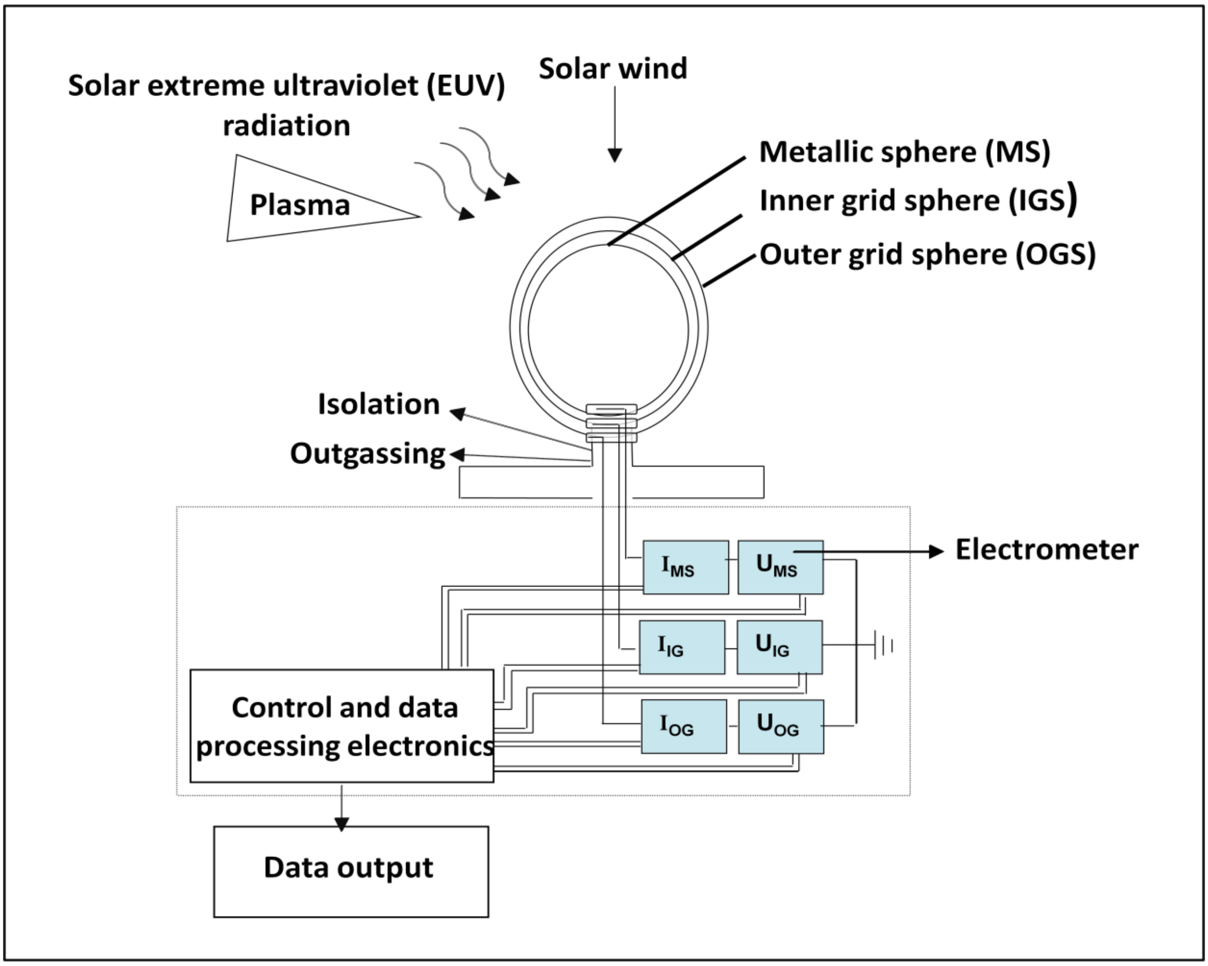

Figure 2.16: Schematic design of the SEPS sensor (Adapted from Brunner *et al.,* 2011:5)

2.9 Conclusion

The fundamental theories of plasma probe and UV radiation are discussed in this chapter. Several probe techniques, specifically the triple probe technique and other methods that can be used for the development of the SEPS and planar sensor prototypes are discussed. The next chapter focuses on simulations of the measurement of plasma in the ionosphere and the behaviour of a copper plate exposed to extreme UV radiation.

CHAPTER THREE: MODELLING AND SIMULATION

3.1 Introduction

This chapter covers the modelling and simulation of plasma in the ionosphere's F-layer region and UV radiation in a vacuum system. The simulations of plasma are implemented based on the principle of Langmuir single probe theory and UV radiation simulations are implemented based on the photoelectric effect principle. These principles describe the behaviour of a probe when immersed in plasma or UV radiation. In a previous study, Merlino (2007:1078) applied the Langmuir single probe theory to generate the *I−V* characteristics and plasma parameters of an ideal planar disk probe using argon ion plasma. Also, Brunner *et al*. (2011) utilised the photoelectric effect to generate photocurrent of spherical probes using EUV radiation. The aim of this chapter is to describe how the *I−V* characteristics and the plasma parameters of an ideal single spherical probe are obtained using atomic oxygen ion plasma. All simulations are carried out in conditions typical of the SAMA region with a particular focus on the ionosphere. Another aim of the chapter is to describe how the photocurrents of a copper plate are generated using UV radiation.

3.2 Plasma simulation

In the present study, the ionosphere parameters (electron temperature, ion temperature, electron density and ion density) are modelled. As shown in Figure 2.6, the peak electron density in the ionosphere's F-layer region is 10^{12} m^{-3} and the peak electron temperature is approximately 3000 K (Hunsucker & Hargreaves, 2003:13−14; Barjatya, 2007:2; Escobar, 2009:27). The single spherical probe sensor is schematically presented in Figure 3.1.

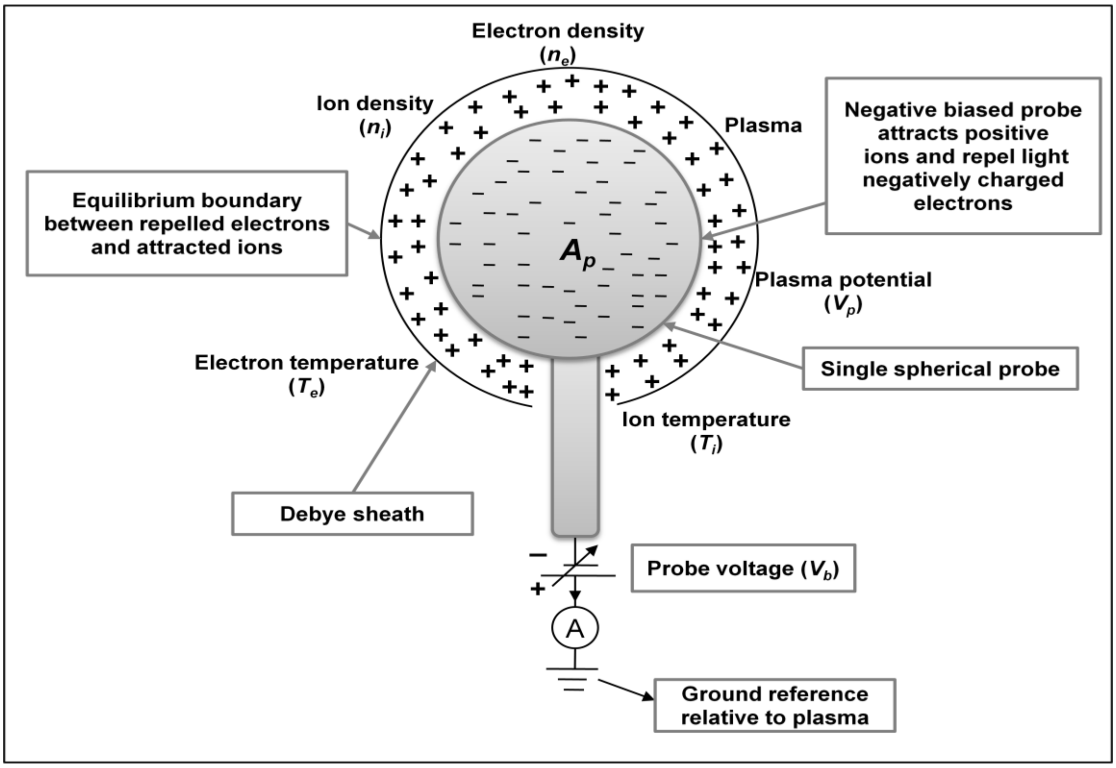

Figure 3.1: Schematic representation of a single spherical probe immersed in the plasma (Adapted from Hamzavi *et al*., 1996:208)

The modelling of the $I\!-\!V$ characteristics of an ideal Langmuir single spherical probe is presented in the following sections.

3.2.1 The ion current flowing to the single spherical probe

From Figure 3.1 the probe voltage, V_b, applied to the spherical probe is negative with reference to the plasma potential, V_p. As a result, the spherical probe will attract positively charged ions to generate negative ion current, I_i. Considering the Maxwellian distribution of ions given by equation 2.24, the ion current flowing from the plasma to the spherical probe with respect to the probe voltage is given by equations 3.1 and 3.2 (Merlino, 2007:1079),

$$I_i(V_b) = \left[-I_{isat} exp\left(\frac{e(V_p - V_b)}{K_B T_i} \right) \right] , \quad V_b \geq V_p \qquad \textbf{Equation 3.1}$$

$$I_i(V_b) = \left[-I_{isat} \right] . \qquad V_b < V_p \qquad \textbf{Equation 3.2}$$

When the ion temperature is equal to the electron temperature, i.e., $T_i = T_e$, the ion-saturation current, I_{isat}, is given by equation 3.3 (Merlino, 2007:1079),

$$I_{isat} = \frac{1}{4} A_p n_i e \cdot \left(\frac{8K_B T_i}{\pi m_i} \right)^{1/2} . \qquad \textbf{Equation 3.3}$$

Furthermore, when the ion temperature is much smaller than the electron temperature, i.e., $T_i << T_e$, the ion-saturation current is determined as the Bohm ion-saturation current (equation 2.25) (Merlino, 2007:1079),

3.2.2 The electron current flowing to the single spherical probe

When the probe voltage, V_b, applied to the spherical probe in Figure 3.1 is positive with reference to the plasma potential, the spherical probe will attract negatively charged electrons to generate an electron current, I_e. Considering the Maxwellian distribution of electrons given by equation 2.22, the electron current flowing from the plasma to the spherical probe with respect to the probe voltage is given by equations 3.4 and 3.5 (Merlino, 2007:1080),

$$I_e(V_b) = \left[I_{esat} exp\left(-\frac{e(V_p - V_b)}{K_B T_e} \right) \right] , \quad V_b \leq V_p \qquad \textbf{Equation 3.4}$$

$$I_e(V_b) = \left[I_{esat} \right] . \qquad V_b > V_p \qquad \textbf{Equation 3.5}$$

When the electron temperature is greater than the ion temperature, i.e., $T_e >> T_i$, the electron-saturation current, I_{esat}, is given by equation 3.6 (Merlino, 2007:1080),

$$I_{esat} = \frac{1}{4} A_p n_e e \cdot \left(\frac{8 K_B T_e}{\pi m_e} \right)^{1/2} . \qquad \textbf{Equation 3.6}$$

Considering equations 2.25, 3.3 and 3.6, the electron-saturation current is greater than the ion-saturation current when the electron density equals the ion density, $n_e = n_i$, and when the electron mass, m_e, is much smaller than the ion mass, m_i.

Furthermore, the ratio of the electron-saturation current and the ion-saturation current when $T_i << T_e$, is given by equation 3.7 (Merlino, 2007:1080),

$$\frac{I_{esat}}{I_{isat}} = \frac{\sqrt{m_i / m_e}}{0.6\sqrt{2\pi}} . \qquad \textbf{Equation 3.7}$$

3.3 Typical plasma parameters of the ionosphere's F-layer region

Table 3.1 describes some of the plasma parameters of the ionosphere's F-layer region. These parameters are required for calculating each individual electron and ion current flowing from the plasma to the spherical probe.

Table 3.1: Typical plasma parameters of the ionosphere's F-layer region (Adapted from Barjatya, 2007:2; Escobar, 2009:38)

Parameters	Symbol	Value	Units
Ion type	O^+	Atomic oxygen	
Ion mass	m_i	2.64×10^{-26}	kg
Electron density	n_e	1×10^{12}	m^{-3}
Ion density	n_i	1×10^{12}	m^{-3}
Electron temperature	T_e	3017	K
Ion temperature	T_i	1160	K
Plasma potential	V_p	1.0	V

3.4 Simulated current-voltage characteristic curve of single spherical probe

Figure 3.2 depicts the simulated $I-V$ curve of the probe current with respect to the probe voltage, V_b. The applied probe voltage is swept until the probe current becomes independent of changes in the voltage, i.e., reaches saturation. The variation of the probe voltage is between -15 V and 10 V. Atomic oxygen ion plasma is used during the simulation of the probe current. The oxygen ion is chosen because it is one of the principal atoms that usually dominate the ionosphere region (Hunsucker & Hargreaves, 2003:26; Escobar, 2009:13). The sphere diameter (d_{sphere}) used for the simulation is 8 cm. This size is chosen to fit inside a 1-unit CubeSat. The sphere diameter is also used to calculate the probe surface area, A_p, as given by equation 3.8,

$$A_p = 4\pi\left(\frac{d_{sphere}}{2}\right)^2 = 0.0201 \text{ m}^2 .$$ **Equation 3.8**

The electron current, I_e, ion current, I_i, and probe current, I_{probe}, are graphically presented using the MATLAB Code in Appendix A.1. The ion and electron currents are, respectively, calculated from equations 3.1 and 3.2 and equations 3.4 and 3.5. The probe current is determined by summing the electron current and the ion current, i.e., $I_{probe}(V_b) = I_e(V_b) + I_i(V_b)$.

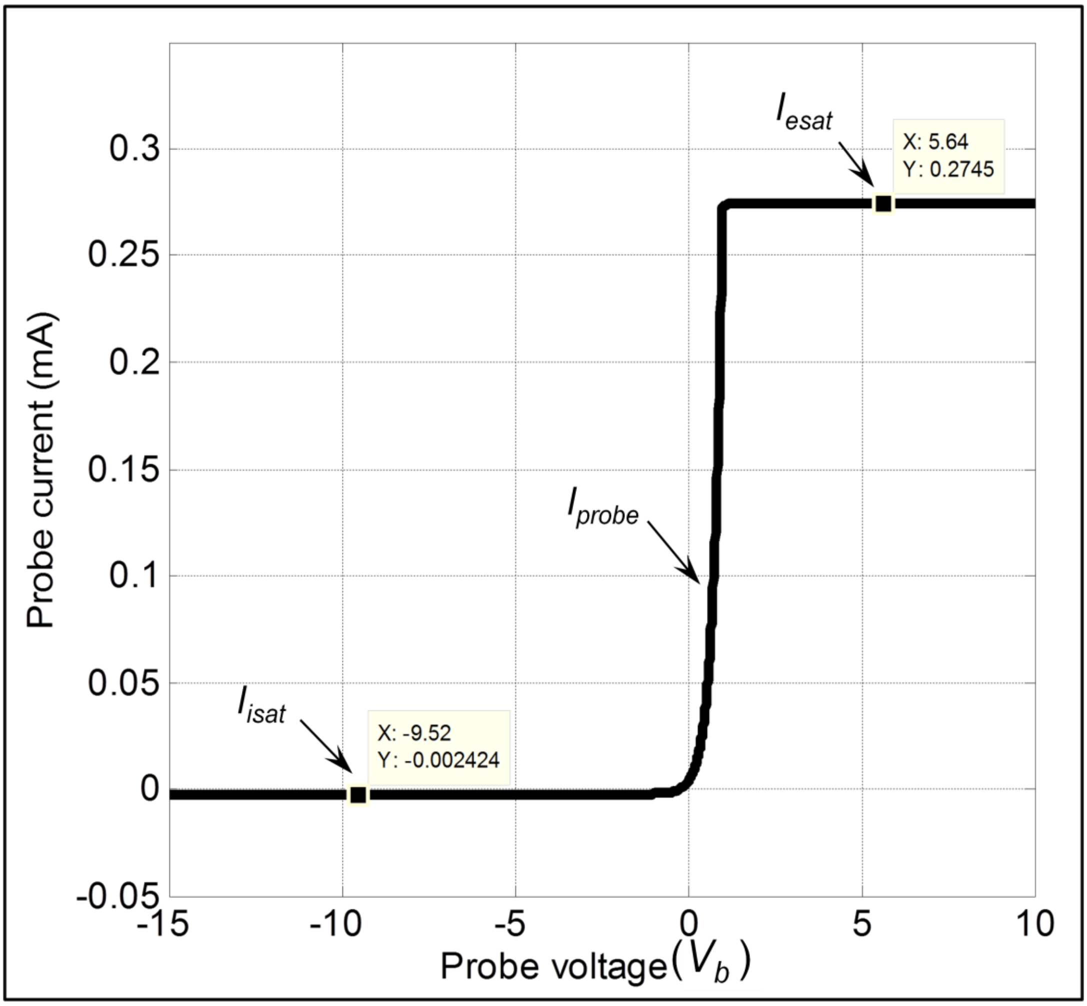

Figure 3.2: Simulated *I−V* characteristic curve of the ideal single spherical probe

The *I−V* characteristic curve corresponding to the typical plasma parameters of the ionosphere's F-layer region using an ideal single spherical probe are illustrated in Figure 3.2. In this figure, the electron current increase gradually to saturation with increased probe voltage, V_b , and also decrease exponentially with decreased probe voltage.

The sharp knee curve obtained after the simulation of the probe current is comparable to the Langmuir probe *I−V* characteristic curve. The theoretical modelling of the ideal *I−V* curve under typical ionospheric F-layer conditions will now be used to illustrate the analyses thereof to determine the measured ionospheric parameters. This was necessary in the absence of real experimental measurements due to the unavailability of testing facilities.

3.5 Extraction of ionospheric plasma parameters from the modelled probe *I−V* characteristic curve

Analysing the $I-V$ characteristic curve depicted in Figure 3.2, the expected ionospheric plasma parameters such as electron temperature and electron density can be determined.

- **Determination of the electron temperature**

As shown in Figure 3.3, the probe current in Figure 3.2 is magnified by a factor of 13 in order to observe the floating probe potential, V_f , at the zero crossing of the curve.

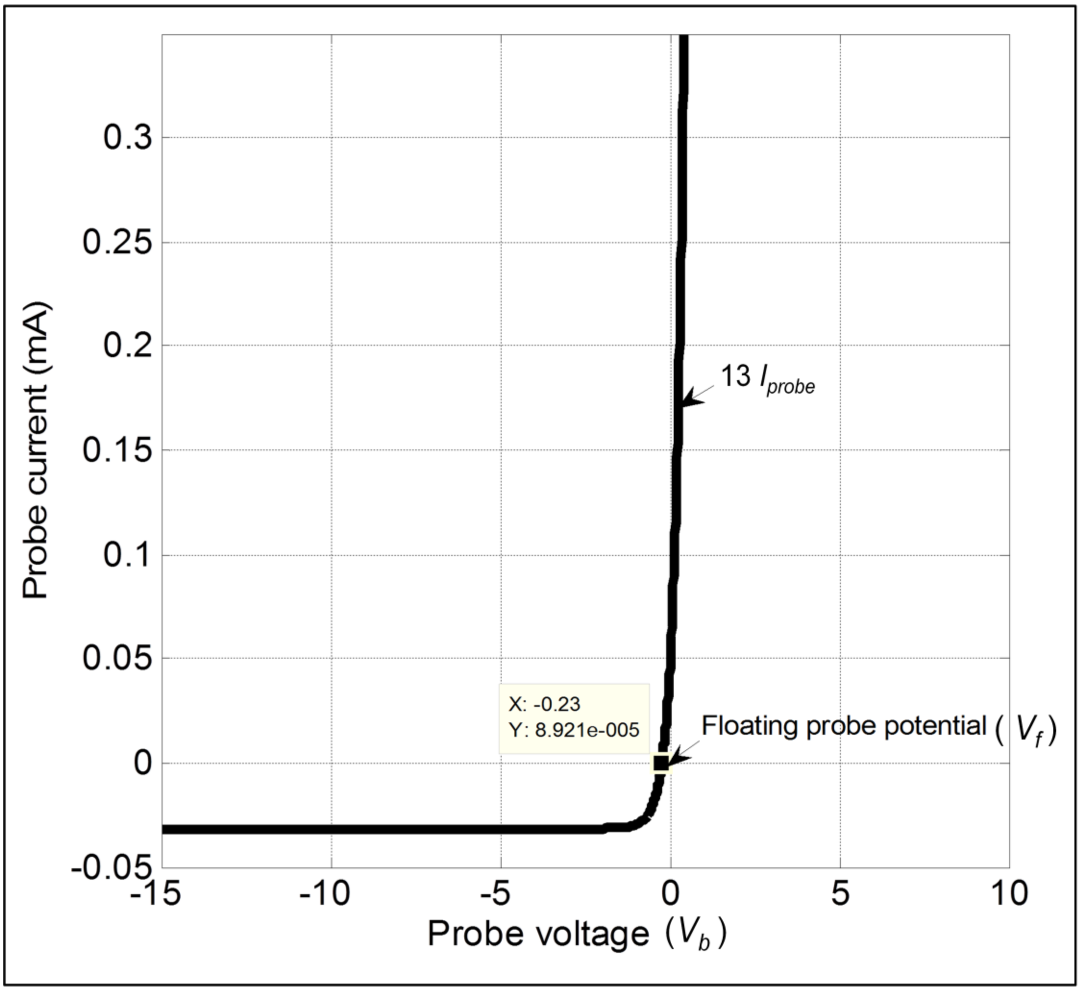

Figure 3.3: Magnified *I−V* characteristic curve of the ideal single spherical probe illustrating the floating probe potential

Furthermore, the semi-logarithmic plot of the $I-V$ characteristic curve illustrated in Figure 3.4 shows that the plasma potential, V_p , can be found between the ERR and the ESR.

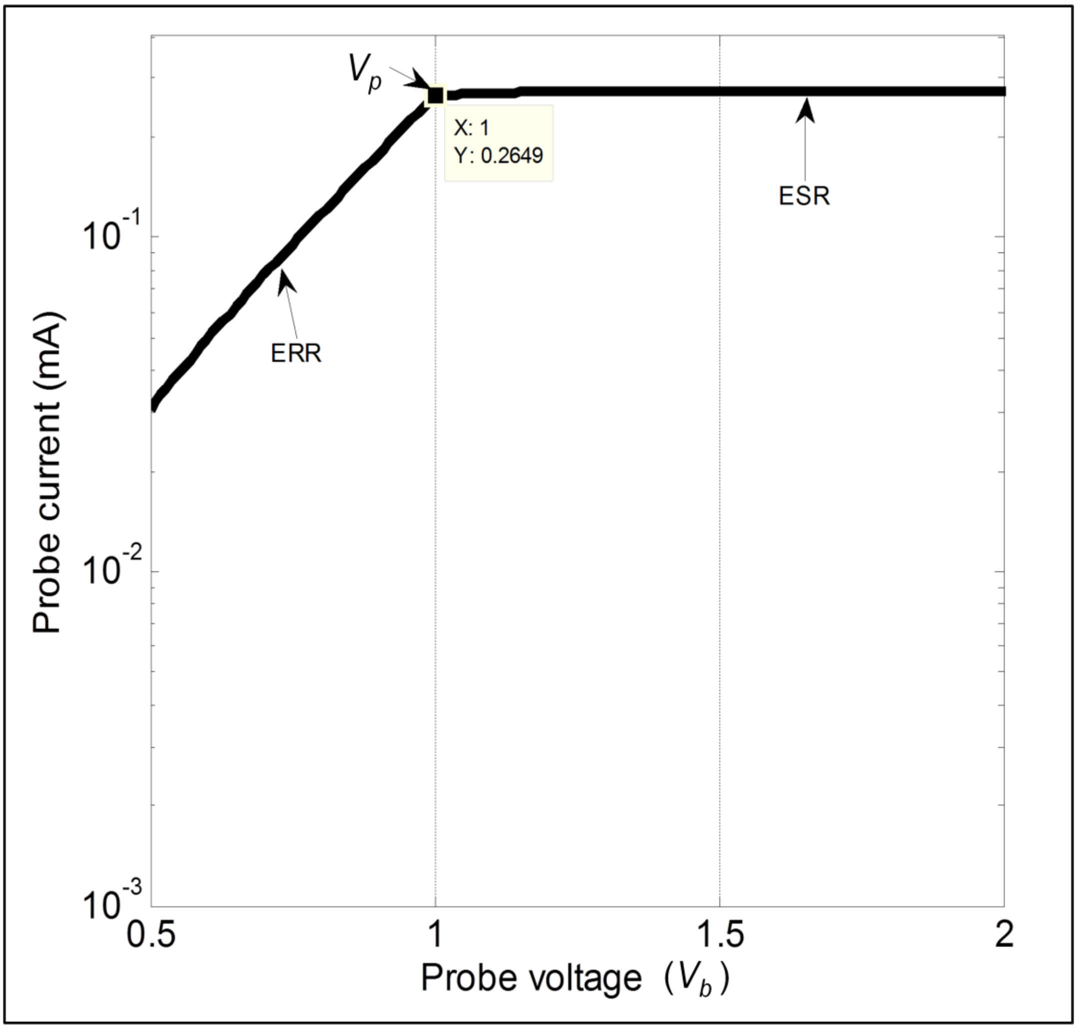

Figure 3.4: Semi-logarithmic plot of the probe *I−V* characteristic curve illustrating the plasma potential

Using the values of V_f (-0.23 V) and V_p (1 V) from the previous graphs, the expected electron temperature, T_e, can be determined analytically using equation 3.9 (Merlino, 2007:1080),

$$T_e = \frac{e \cdot \left(V_f - V_p\right)}{K_B \cdot ln\left(\frac{2\pi m_e}{m_i}\right)} , \qquad \textbf{Equation 3.9}$$

$$T_e = 3017 \text{ K} .$$

This result shows that the peak electron temperature (3017 K) in the ionosphere's F-layer region can be determined using the measured floating probe potential, V_f, from the *I−V* curve (Figure 3.3).

- **Determination of the electron density**

The expected electron density, n_e , can be determined analytically using equation 3.6,

$$n_e = \frac{I_{esat} \times 4}{A_p e} \cdot \sqrt{\frac{\pi m_e}{8 K_B T_e}} ,$$

$$n_e = 1 \times 10^{12} \text{ m}^{-3} .$$

This result shows that the peak electron density (1×10^{12} m^{-3}) in the ionosphere's F-layer region can be determined using the measured electron-saturation current, I_{esat} , from the $I-V$ curve (Figure 3.2).

3.6 Ultraviolet radiation simulation

3.6.1 Determination of the incident photon energy and wavelength

The material used in the present study is copper. Considering the metal's properties listed in Table 2.3, the work function of copper is approximately 4.7 eV and the minimum photon energy needed to eject electrons from its surface is

$$\Phi_{copper} = (4.7) \times \left(1.6 \times 10^{-19}\right) = 7.52 \times 10^{-19} \text{ J} .$$

The maximum UV light wavelength that corresponds to this energy can be determined using equation 3.10,

$$\Phi_{copper} = \frac{hc}{\lambda} , \qquad \textbf{Equation 3.10}$$

$$\lambda = \frac{\left(6.63 \times 10^{-34}\right) \times \left(3 \times 10^{8}\right)}{7.52 \times 10^{-19}} ,$$

$$\lambda = 2.6449 \times 10^{-7} \text{ m} = 264 \text{ nm}.$$

3.6.2 Determination of photocurrents and stopping potentials with copper plate

As previously discussed in section 2.7, the photoelectric effect produces the probe current when a metal plate surface is exposed to UV radiation. Figures 3.5 to 3.13 depict a series of qualitative simulations of a copper plate exposed to UV radiation. The Photoelectric Effect 1.10 Applet software is used for the simulations (Phet, 2011). The wavelength range of the UV spectra used in this simulation is 100 nm to 400 nm. The applied voltage is varied from -8.0 V to 8.0 V.

- **Ultraviolet light wavelengths between 262 nm and 240 nm**

The results obtained from Figures 3.5 and 3.6 show that with UV wavelengths between 262 nm and 240 nm, electrons are ejected from the plate A (copper cathode) but no current is flowing from plate B (collector). Therefore, a copper plate (Φ_{copper} = 4.7 eV) may generate photocurrent at the UV light wavelengths below 240 nm (Figure 3.7).

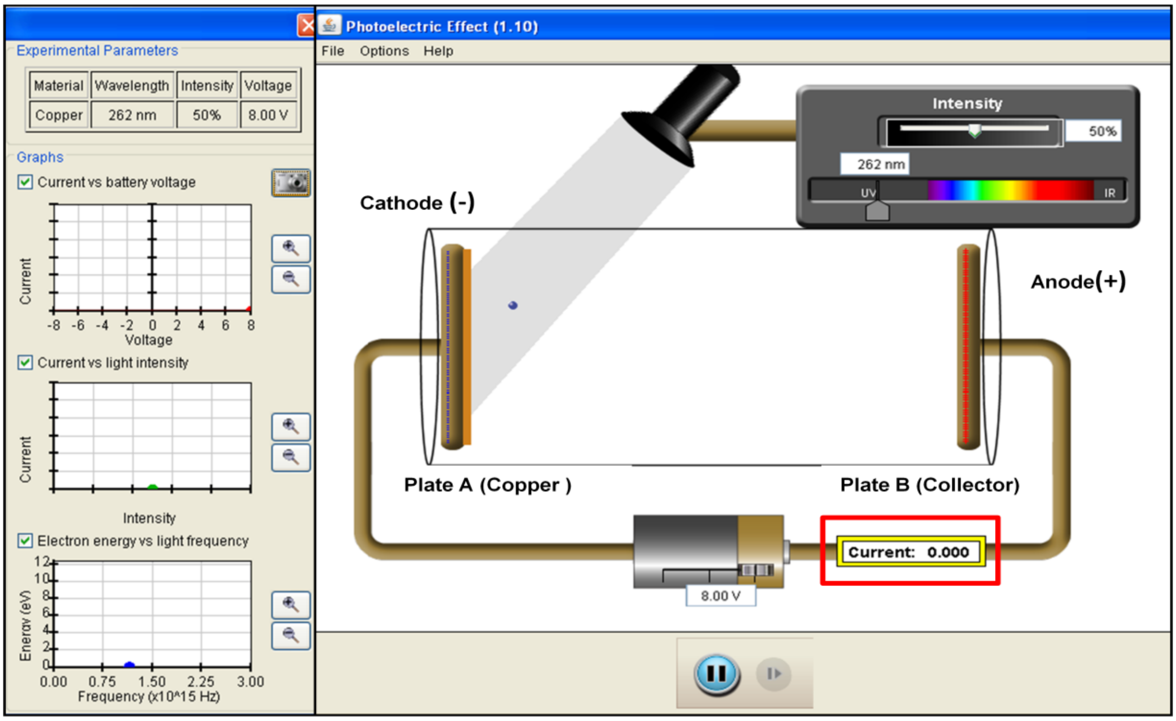

Figure 3.5: Ultraviolet light wavelength of 262 nm with accelerating voltage of 8.0 V

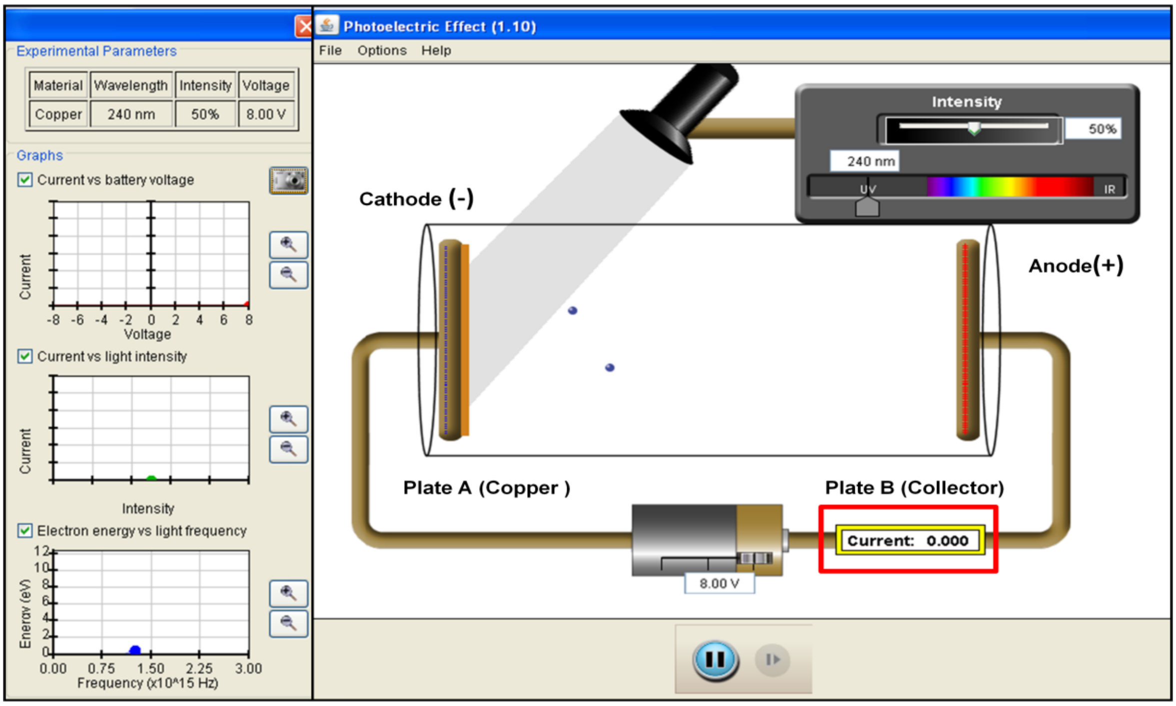

Figure 3.6: Ultraviolet light wavelength of 240 nm with accelerating voltage of 8.0 V

- **Ultraviolet light wavelength of 237 nm**

When the applied UV light wavelength is set at 237 nm and the accelerating voltage of the plate B (collector) is varied from 0 V to 8.0 V, the current obtained is 0.018 A (Figure 3.7). The current remains constant for positive bias since the number of electrons released from the copper is only a function of the radiation intensity. Alternatively, when the applied voltage is varied from -0.2 V to -8.0 V, no current is measured (Figure 3.8). From these observations, the simulated stopping voltage of copper for 237 nm UV light is -0.2 V. These conditions are summarised in Figure 3.9 using the Matlab code in Appendix A.2.

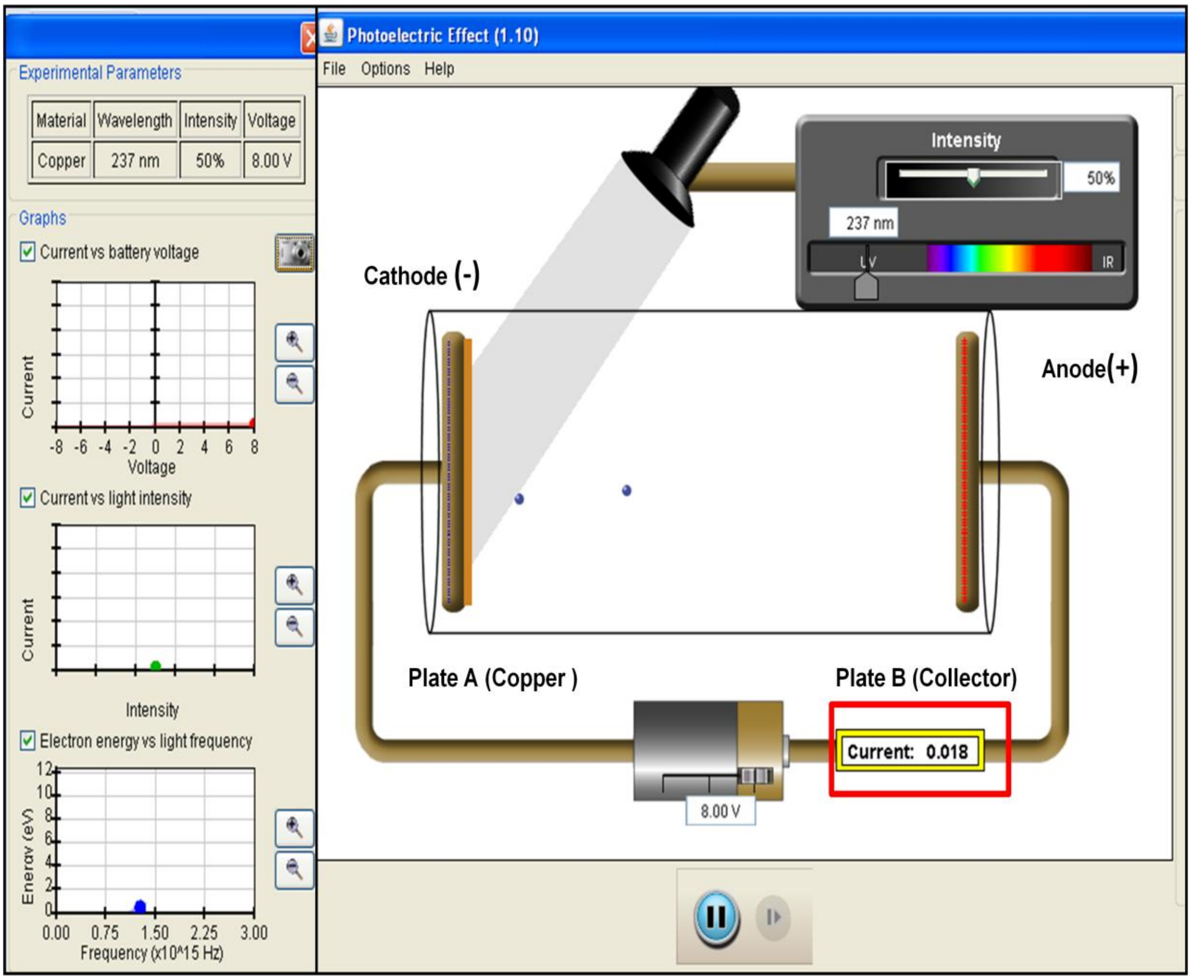

Figure 3.7: Ultraviolet light wavelength of 237 nm with accelerating voltage of 8.0 V

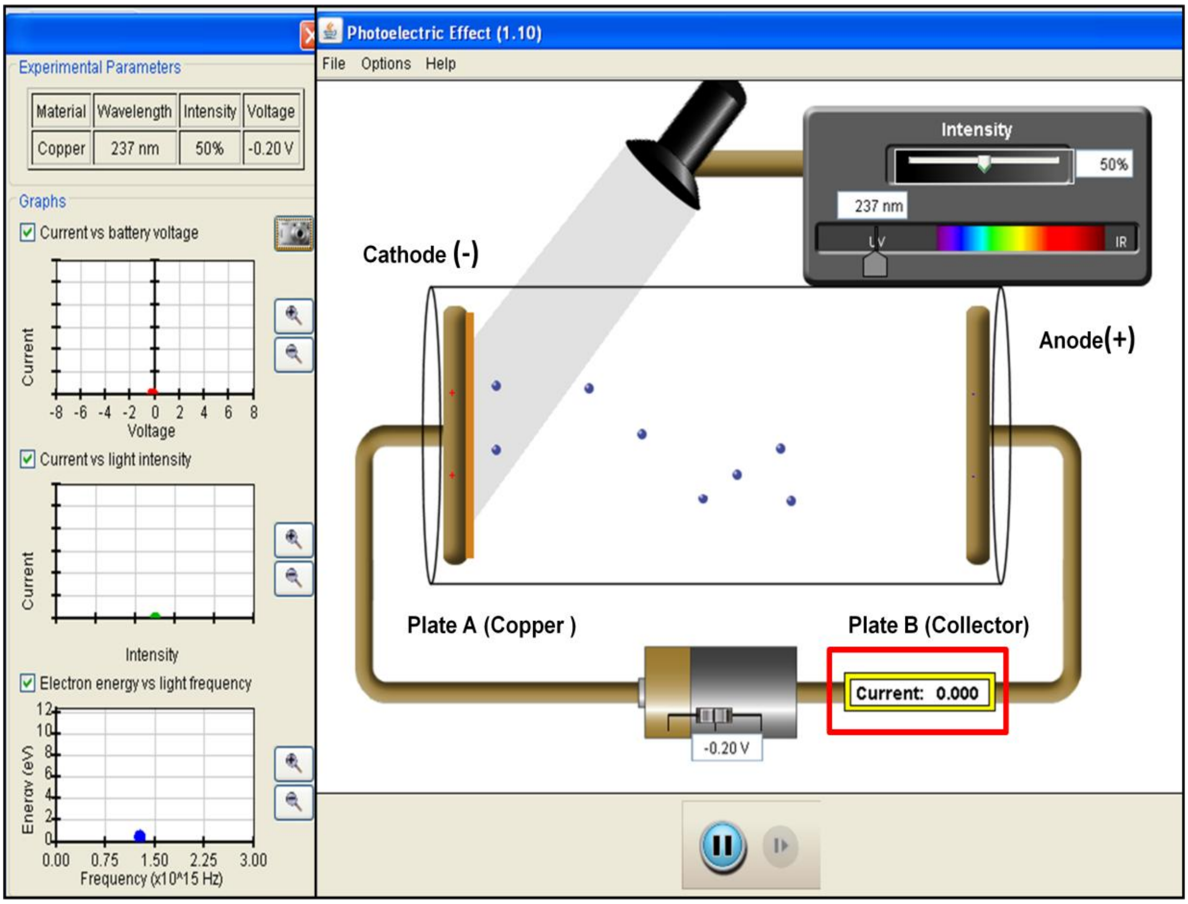

Figure 3.8: Ultraviolet light wavelength of 237 nm with stopping voltage of - 0.2 V

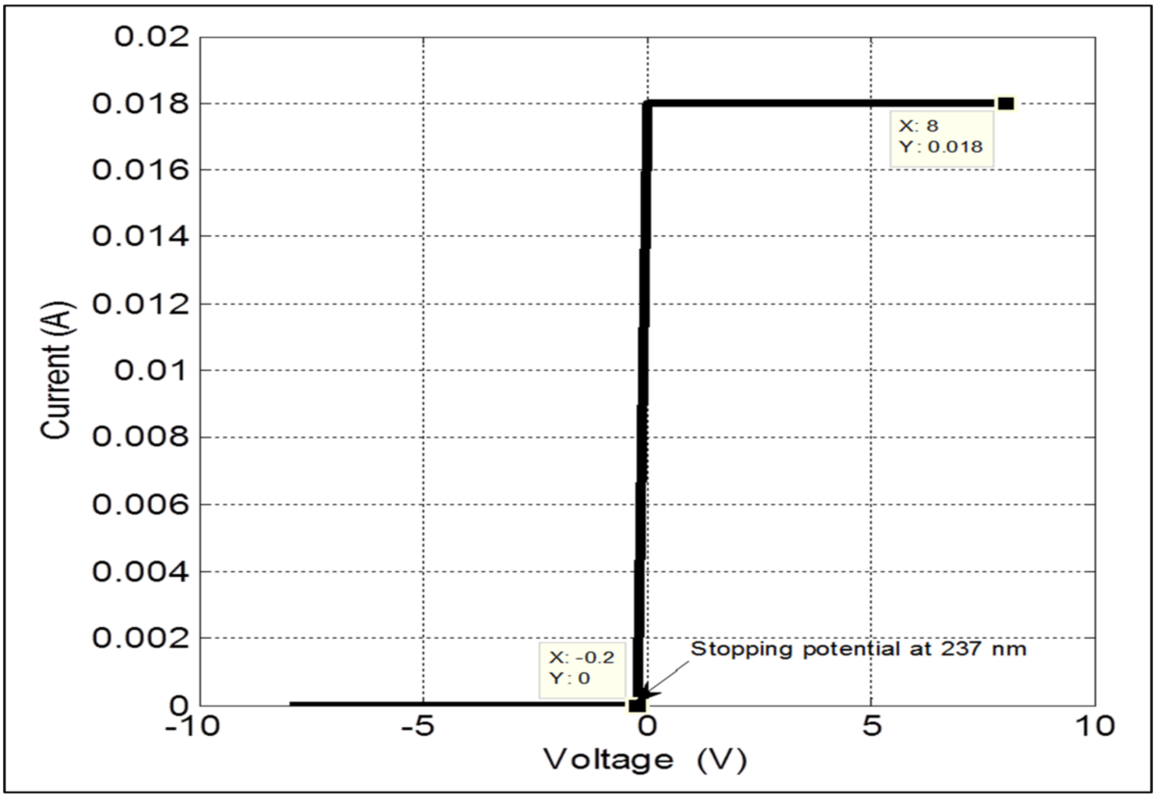

Figure 3.9: Simulated photocurrent versus collector bias voltage at 237 nm wavelength

- **Ultraviolet light wavelength of 141 nm**

When the applied UV light wavelength is set at 141 nm and the accelerating voltage of the plate B (collector) is varied from 0 V to 8.0 V, electrons flow toward plate B and the current obtained remained at 0.622 A (Figure 3.10). This is higher than for 237 nm UV radiation since the photons are more energetic and require more deceleration to be stopped. Alternatively, when the applied voltage is varied from -0.2 V to -3.8 V, the current obtained is between 0.605 A and 0.046 A (Figure 3.11). However, when the applied voltage is varied from -4.0 V to -8.0 V, no current is obtained (Figure 3.12). From these observations, the simulated stopping voltage of copper for 141 nm UV light is -4.0 V. These conditions are also summarised in Figure 3.13 using the Matlab code in Appendix A.3.

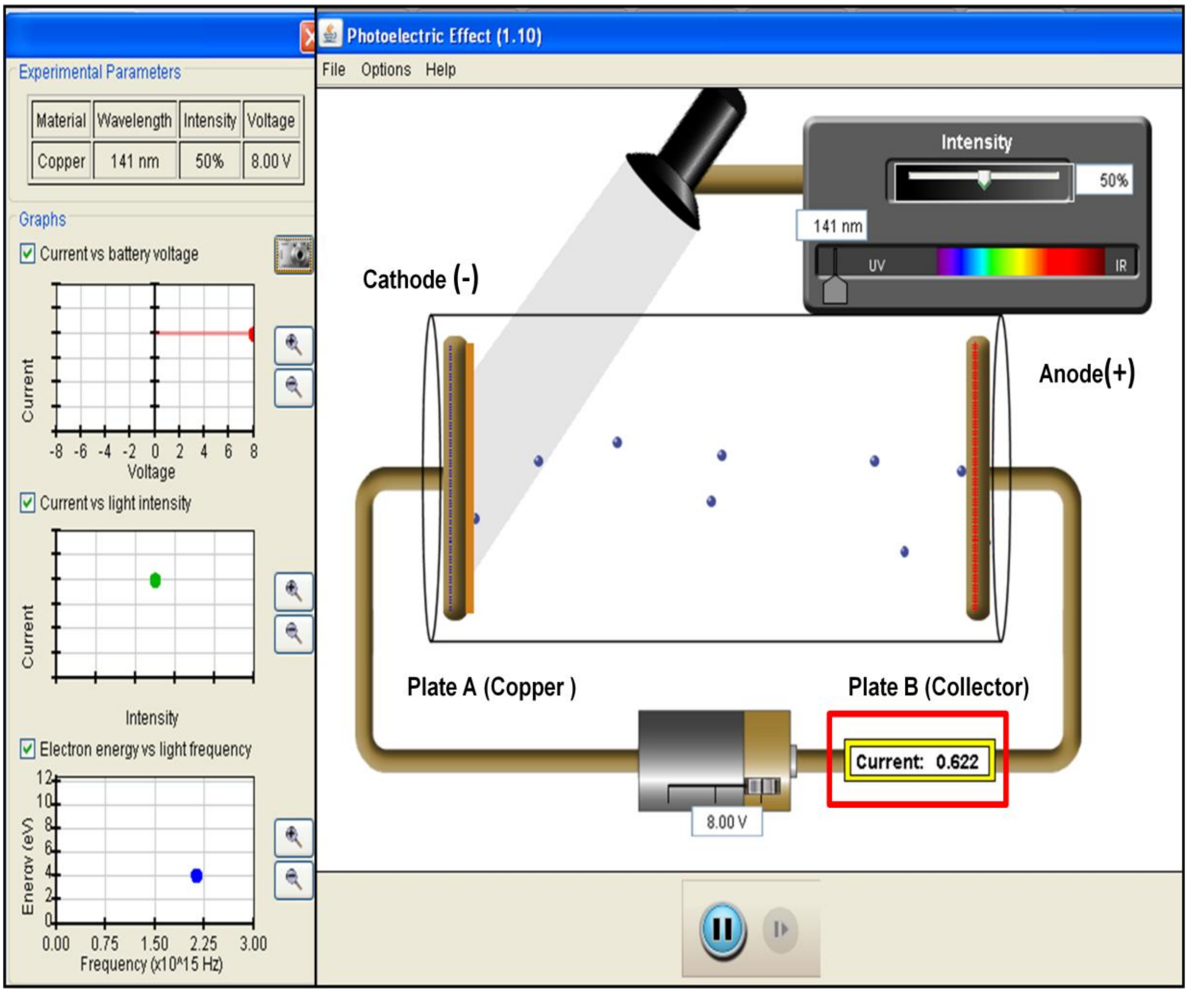

Figure 3.10: Ultraviolet light wavelength of 141 nm with accelerating voltage of 8.0 V

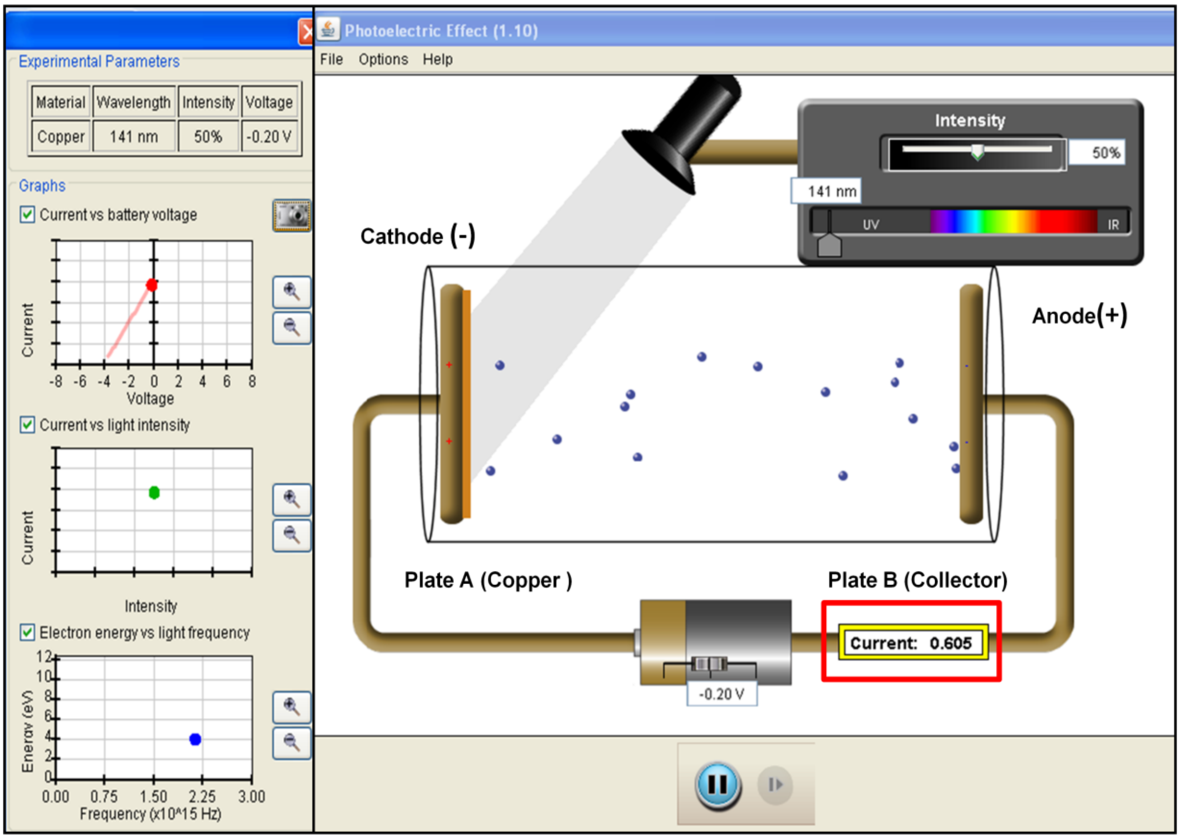

Figure 3.11: Ultraviolet light wavelength of 141 nm with decelerating voltage of - 0.2 V

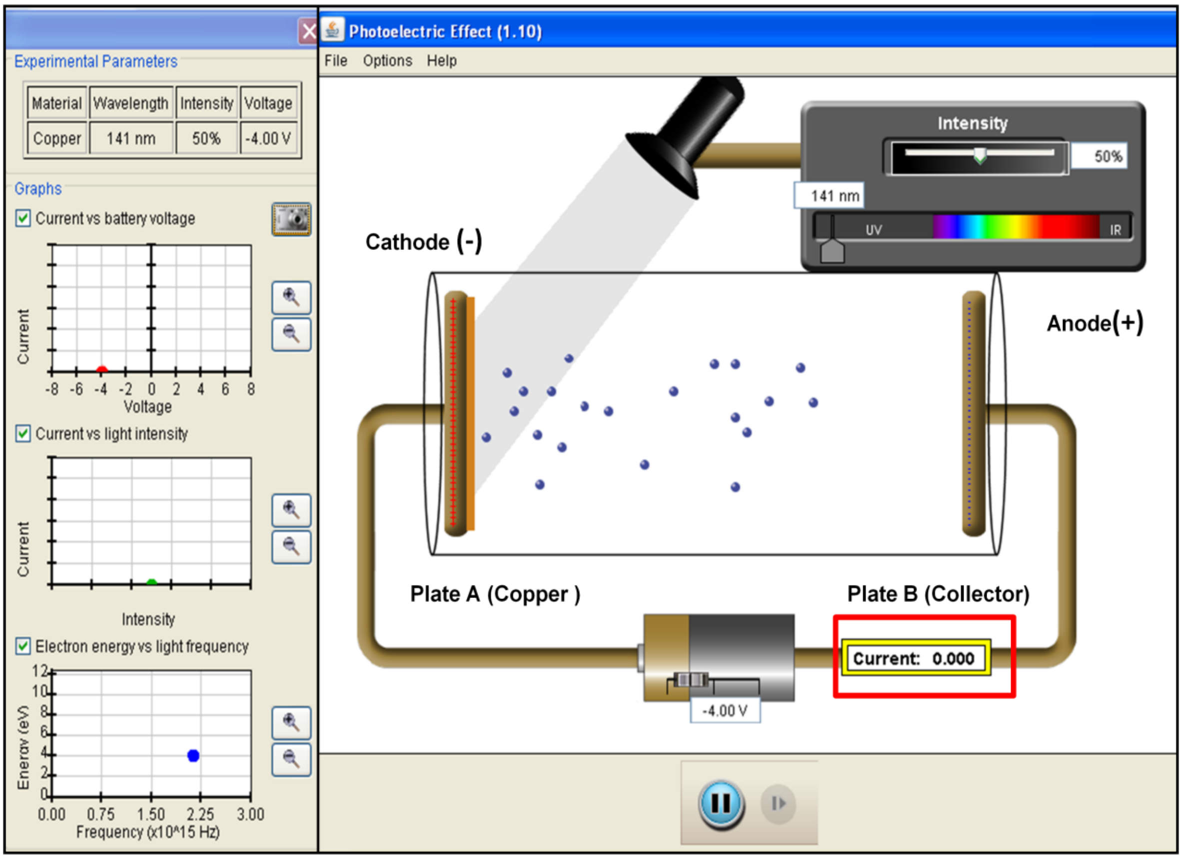

Figure 3.12: Ultraviolet light wavelength of 141 nm with stopping voltage of - 4.0 V

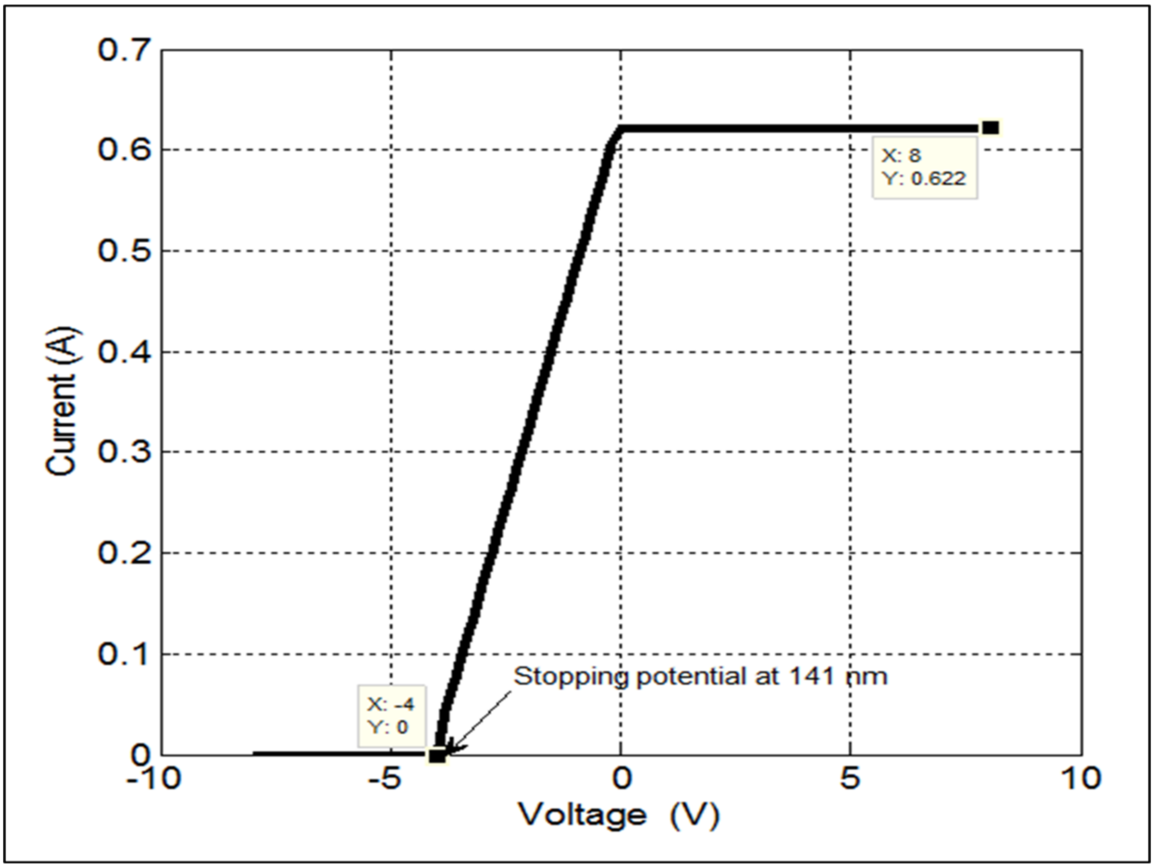

Figure 3.13: Simulated photocurrent versus collector bias voltage at 141 nm wavelength

Table 3.2 shows the complete summary of the calculated copper stopping potentials from equation 2.45 and the simulated copper stopping potentials for UV wavelengths ranging from 100 nm to 400 nm. These simulated stopping potentials will guide the selection of stopping potentials used in the VUV experiments described in the following chapter.

Table 3.2: Comparison of the calculated copper stopping potentials and the simulated copper stopping potentials for UV wavelengths ranging from 100 nm to 400 nm

UV Type	Light wavelength (nm)	Calculated copper stopping potential (V)	Simulated copper stopping potential (V)
UVA – UVB	265 to 400	None	None
UVC	264	-0.01	None
UVC	263	-0.03	None
UVC	262	-0.04	None
UVC	240	-0.48	None
UVC	237	-0.54	-0.20
UVC	204	-1.39	-1.20
UVC	180	-2.21	-2.20
UVC	160	-3.07	-3.00
UVC	141	-4.12	-4.00
UVC	116	-6.01	-6.00
UVC	100	-7.73	-7.60

3.7 Conclusion

From the plasma simulations, ionospheric plasma parameters such as electron temperature and electron density are extracted from the $I-V$ characteristic curve obtained from an ideal single spherical probe. From the UV radiation simulations, the photocurrents are obtained. UV light with wavelengths shorter than 237 nm produced photocurrents.

After calculations and simulations, the stopping potentials that could decelerate electrons emitted with UV radiation wavelengths between 100 nm and 237 nm are, respectively, between -7.6 V and -0.2 V. When comparing the calculated copper stopping potentials with the simulated copper stopping potentials, the results converge for shorter wavelengths. In the present study, these results are used in the experimental design and VUV radiation testing of the sensor prototypes (SEPS and planar).

CHAPTER FOUR: EXPERIMENT DESIGN, IMPLEMENTATION AND MEASUREMENT

4.1 Introduction

In this chapter, the design and fabrication of the sensor prototypes (SEPS and planar) are discussed. The planar sensor is designed to minimise the experimental uncertainty observed with the complex structure of the SEPS sensor. The SEPS sensor is tested under vacuum ultraviolet (VUV) pulsed laser radiation conditions while the planar sensor is tested with both a VUV pulsed laser and a VUV deuterium lamp with continuous radiation.

4.1.1 Fabrication of the SEPS sensor prototype

The prototype is made of three spherical probes, which are the metallic sphere (MS), the inner grid sphere (IGS) and the outer grid sphere (OGS). These probes are isolated and separated from one another by a distance of 5 mm. The probes' diameters are chosen such that the prototype will fit in a 1U CubeSat form factor and are, respectively, 60 mm, 70 mm and 80 mm. Copper is used for the construction of the probes due to its good work function and high conductivity. Materials like titanium are not considered because of cost. Pictures of the three spheres and the SEPS sensor prototype are shown in Figures 4.1 and 4.2.

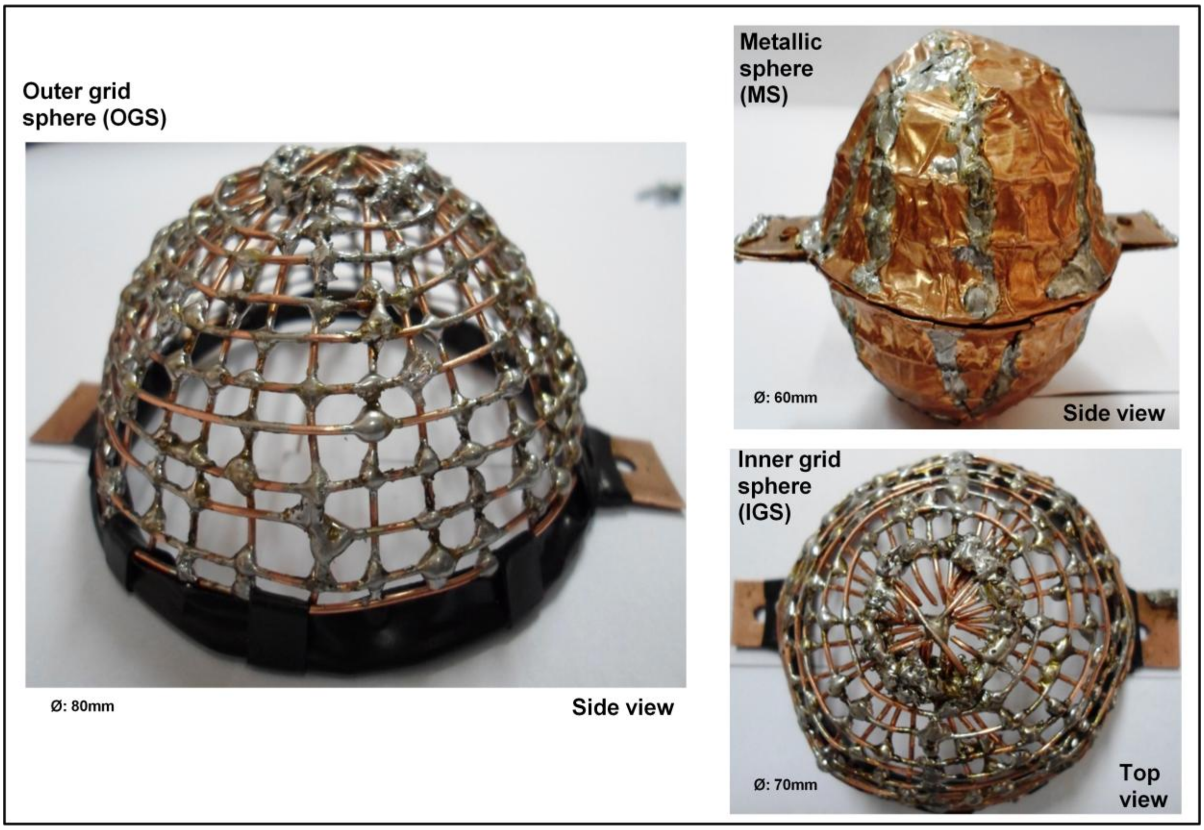

Figure 4.1: Photos of the spherical probe prototypes

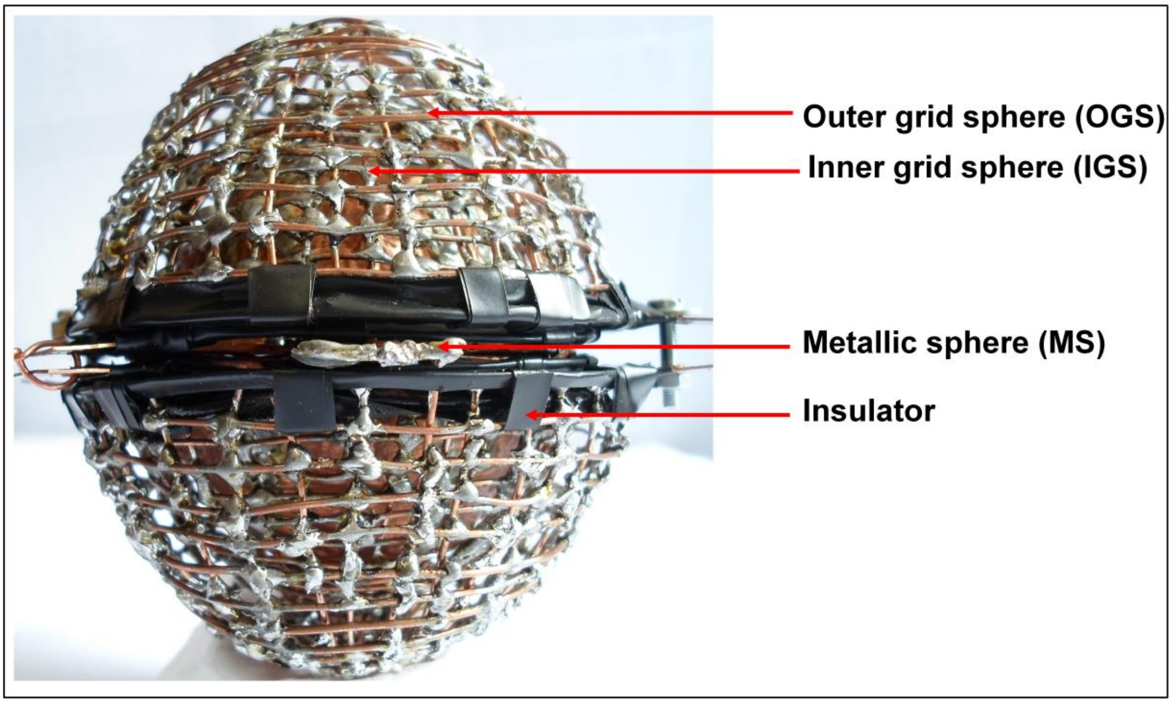

Figure 4.2: Photo of the SEPS sensor prototype

4.1.2 Fabrication of the planar sensor prototype

The planar sensor prototype is fabricated based on the design structure of the SEPS sensor. The sensor consists of three planar copper probes, namely a metallic plate (MP), an inner grid (IG) and an outer grid (OG). These probes are separated from one another by a distance of 10 mm (Figure 4.3). Furthermore, the probes' dimensions are chosen to enable mounting the sensor on one side of a 1U CubeSat. The side dimension of the square plates is 50 mm.

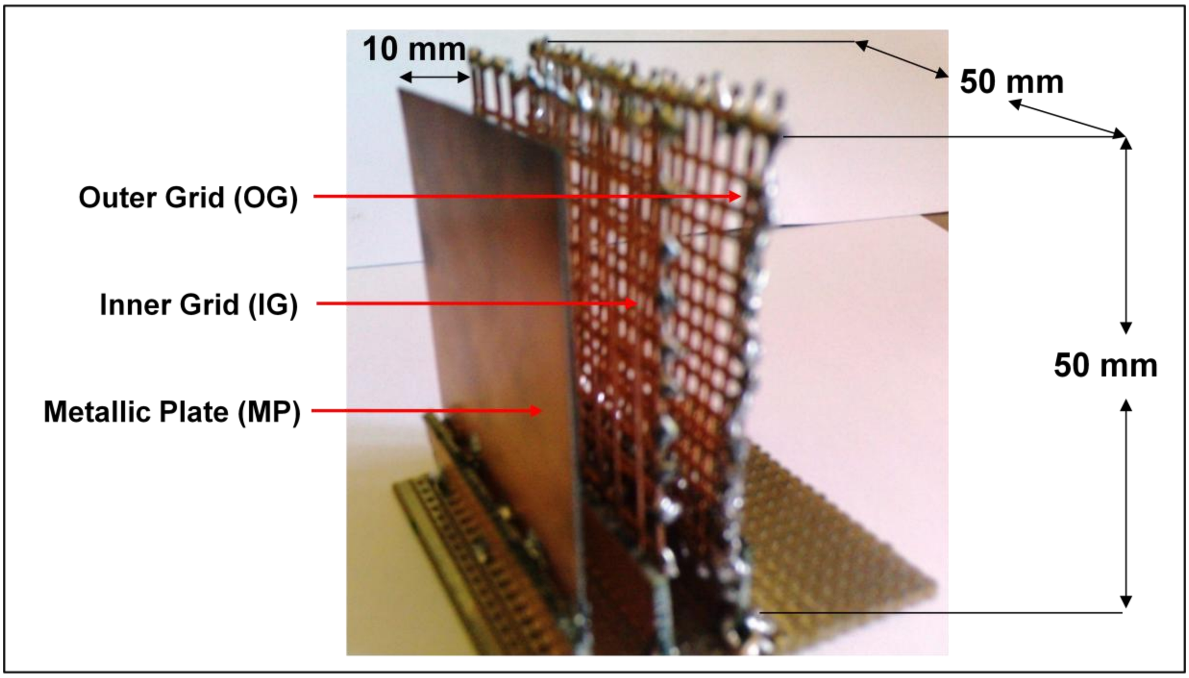

Figure 4.3: Photo of the planar sensor prototype

4.2 Setup of the VUV pulsed laser and deuterium lamp radiation experiments

A VUV radiation source is used to create an actual EUV environment. The VUV radiation experiments are conducted at the Laser Research Institute within the Department of Physics at the University of Stellenbosch (South Africa). In these experiments, the aim is to measure the terminal voltage of the SEPS and planar sensors under VUV radiation from a pulsed laser source. In another experiment, the planar sensor is subjected to continuous radiation from a VUV deuterium light source.

4.2.1 VUV pulsed laser radiation experiment

VUV radiation is obtained from a VUV pulsed laser beam which has a visible 430 nm light source and a VUV 140 nm light source. The VUV pulsed laser beam produces 10 nJ of energy per pulse. Each pulse width is 5 ns and has a repetition rate of 10 Hz. The laser radiation source produces a beam spot size of approximately 2 to 3 mm in diameter. This spot size is enlarged by a defocusing lens in order to increase the beam coverage area and to ensure that the sensor is well-radiated. The laser beam passes through a pipe to a vacuum chamber which is connected with a standard O-ring sealed KF-40 flange. The sensor's wire passages are sealed to avoid air leakage. A base pressure of the order 10^{-5} mbar is maintained in the chamber. The SEPS or planar sensor prototypes are placed in the vacuum chamber before the start of the experiments. The VUV pulsed laser radiation experimental setup is pictured in Figure 4.4. In this figure, the radiation source is out of view.

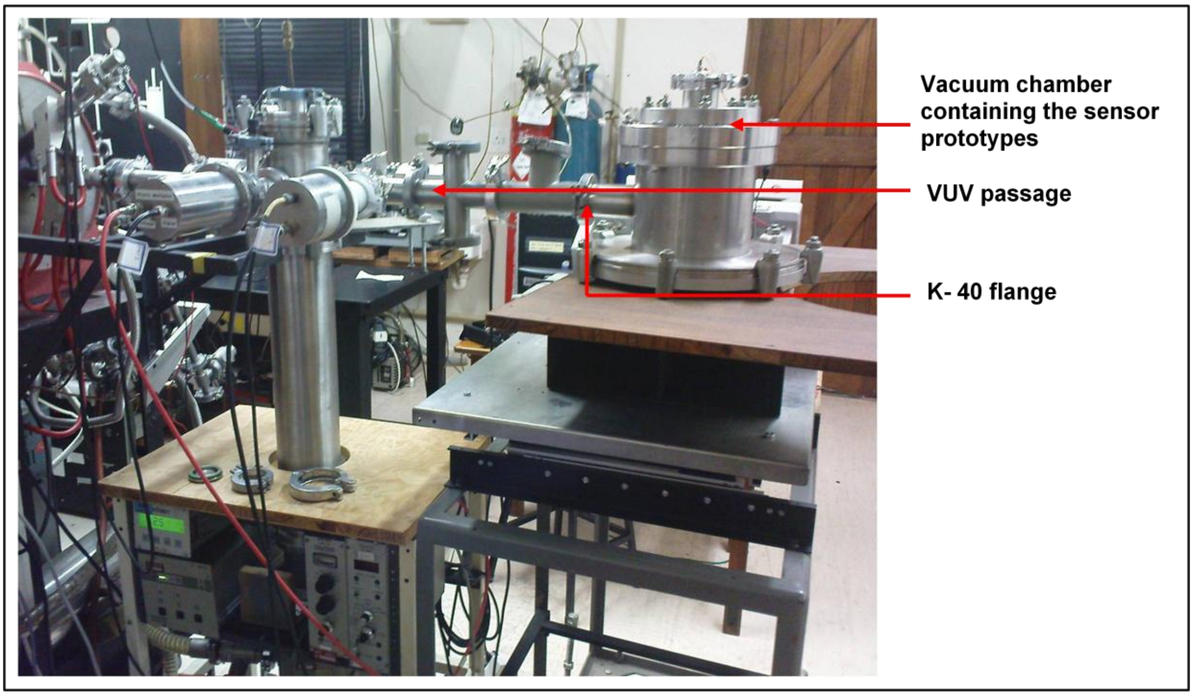

Figure 4.4: The VUV pulsed laser radiation experimental setup at the Laser Research Institute within the Department of Physics at the University of Stellenbosch (South Africa)

4.2.2 VUV deuterium lamp radiation experiment

Continuous VUV radiation is obtained from a McPherson Model 632 deuterium lamp (McPherson Inc, USA) which is calibrated for wavelengths ranging from 116 nm to 410 nm. The source has an emitting area of 1 mm in diameter and a 30 W lamp. Radiation is emitted through a magnesium fluoride window to a VUV monochromator before reaching the vacuum chamber (Figure 4.5). The monochromator is used to filter a selectable band of the VUV light spectrum (116 nm to 410 nm). The sensor's wire passages are sealed to avoid air leakage. The base pressure of the vacuum chamber is again maintained at about 10^{-5} mbar. The planar sensor prototype is placed in the vacuum chamber before the start of the experiments. The probe plates are orthogonal to the radiation to ensure optimal exposure. The VUV deuterium lamp radiation experimental setup is pictured in Figure 4.5.

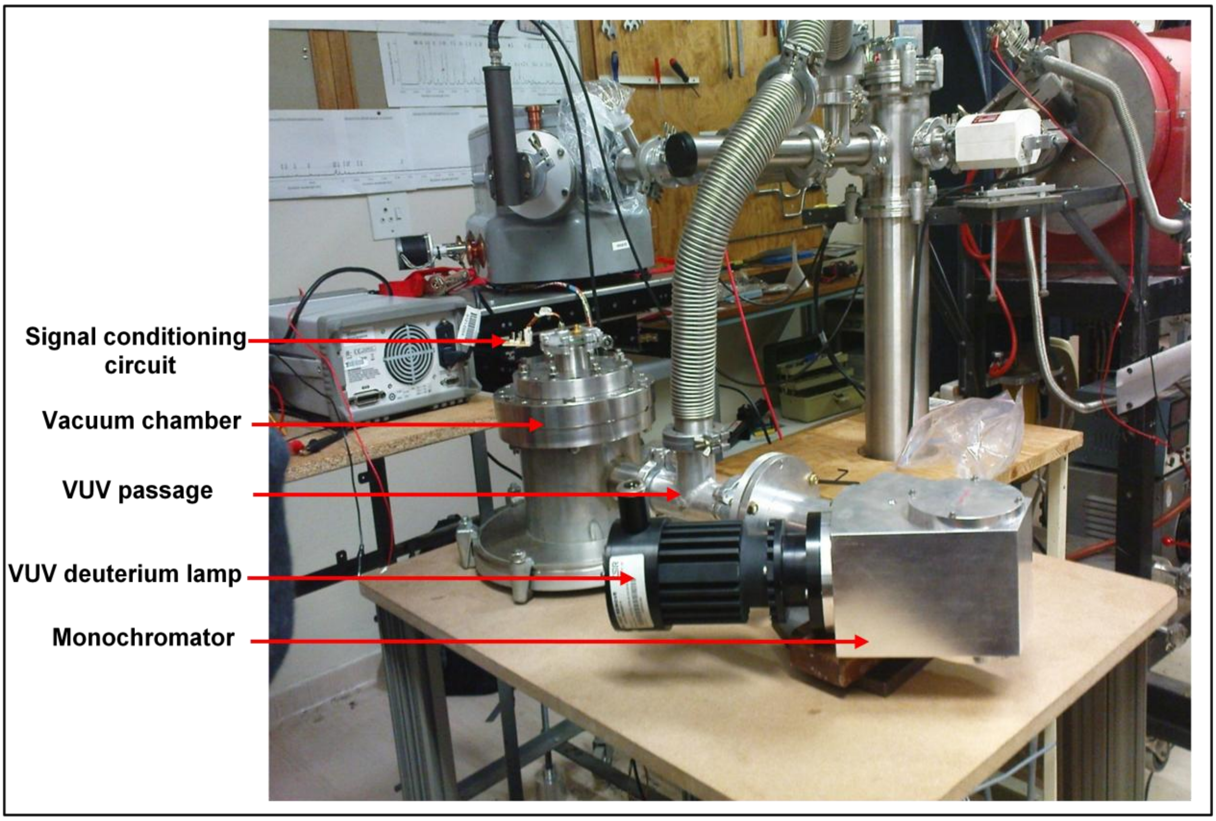

Figure 4.5: The VUV deuterium lamp radiation experimental setup at the Laser Research Institute within the Department of Physics at the University of Stellenbosch (South Africa)

4.3 Circuit modelling of SEPS and planar sensors

The SEPS and planar sensors are initially modelled as two plate capacitors by connecting their inner and outer grids. The two plate capacitor model is considered because of its simplicity whilst being representative of the underlying principle of operation of the sensors.

4.3.1 VUV pulsed laser experiment with the SEPS sensor

4.3.1.1 Description of the circuit model

The capacitive measurement setup which is used for the SEPS sensor during the VUV pulsed laser radiation experiment is shown in Figure 4.6. The SEPS sensor probes, MS, IGS and OGS as connected form a two plate spherical capacitor. The MS acts as a spherical conductor of radius "*a*" and the connected IGS and OGS act as a spherical conductor of effective radius "*b*". The IGS and OGS are combined to collect more electrons since both grids are not solid in structure. The capacitive measurement setup is carried out by applying a bias voltage, V_b, to the two plate spherical capacitor through a load resistor as shown in Figure 4.6.

With no radiation the bias voltage, V_b, supports negative charge on the MS and positive charge on the combined IGS and OGS. This charge, Q, is given by

$$Q=CV_b \qquad \textbf{Equation 4.1}$$

where C is the capacitance of the spherical capacitor.

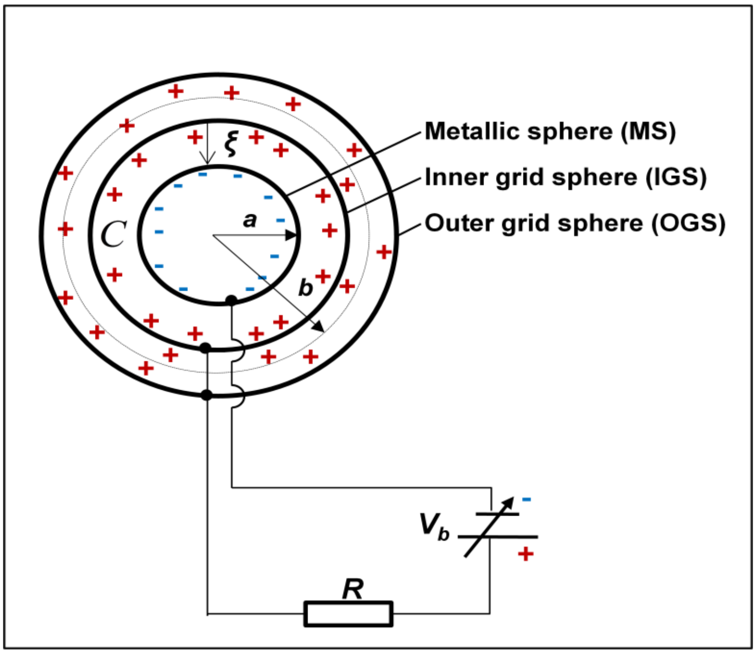

Figure 4.6: Schematic of the two plate spherical capacitor used in the VUV pulsed laser radiation experiment

The corresponding circuit schematic is shown in Figure 4.7.

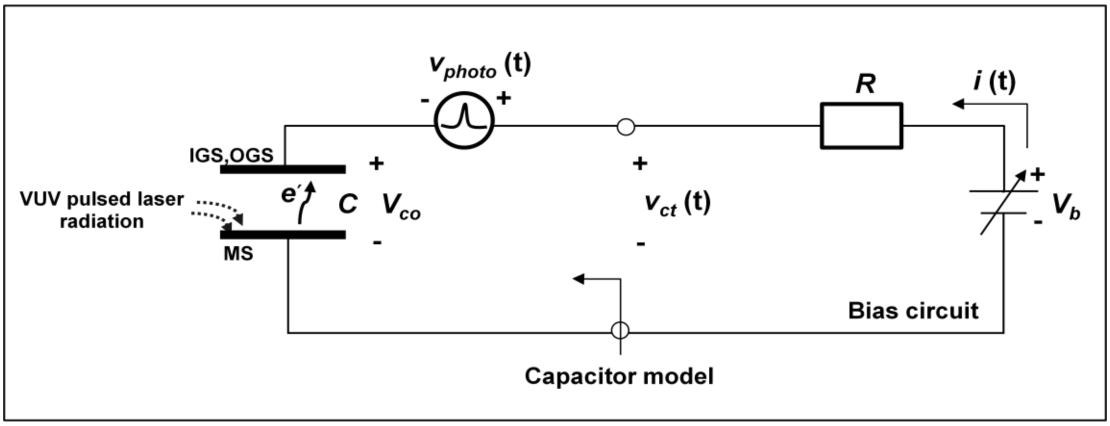

Figure 4.7: Circuit model of the two plate spherical capacitor

Considering Figure 4.7, the capacitor must be modelled according to its expected behaviour.

- **Behaviour of charge on the spherical capacitor**

With no radiation the spherical capacitor is fully charged. The charge, Q, on each plate is given by

$$Q = CV_{co} = CV_b\,. \qquad \textbf{Equation 4.2}$$

The 5 ns radiation pulses eject electrons (e') from the negative plate of the capacitor (MS) through the photoelectric effect. The electrons are attracted towards the positive plate. Under favourable bias conditions, the free electrons will deposit on the positive plate. This causes a change in charge on the positive plate and subsequently a change in terminal voltage, according to $\Delta Q=C\cdot\Delta V$. At the end of the pulse, the charge on the capacitor will revert to its steady state value Q. This happens over a few RC time constants, which is determined by the external R and the C of the capacitor. The charge on the positive plate of the capacitor can therefore be modelled as the signal presented in Figure 4.8.

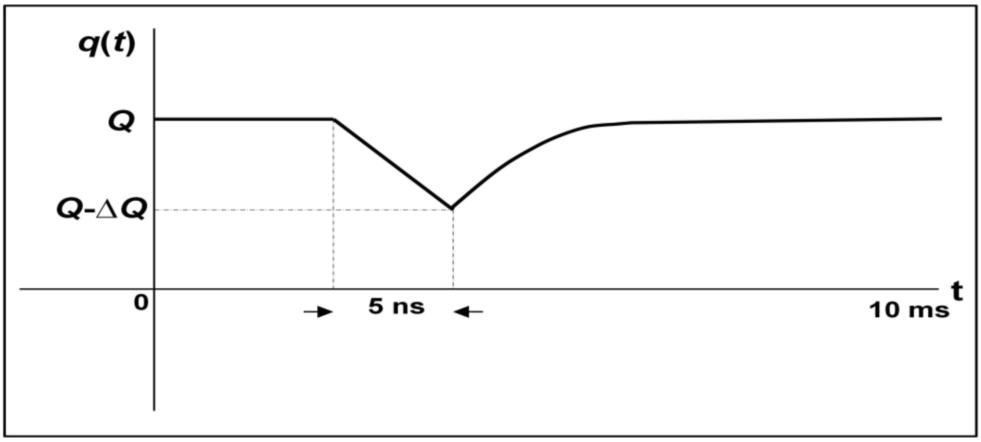

Figure 4.8: Charge on the positive plate of the spherical capacitor under pulsed radiation conditions

During the pulse, the charge is assumed to reduce linearly as the electrons deposit on the positive plate. This repeats every 10 ms. The *RC* time constant must be chosen such that the capacitor will revert to its steady state before the next pulse otherwise the capacitor will discharge. Therefore, *RC* << 10 ms. However, the *RC* time constant must be long enough to stretch the voltage pulses in order to observe them easier in the time domain. As a result, the *RC* time constant must also be greater than the pulse width of the VUV laser, *RC* > 5 ns.

The expected terminal voltage, V_{ct}, measured across the spherical capacitor is shown in Figure 4.9.

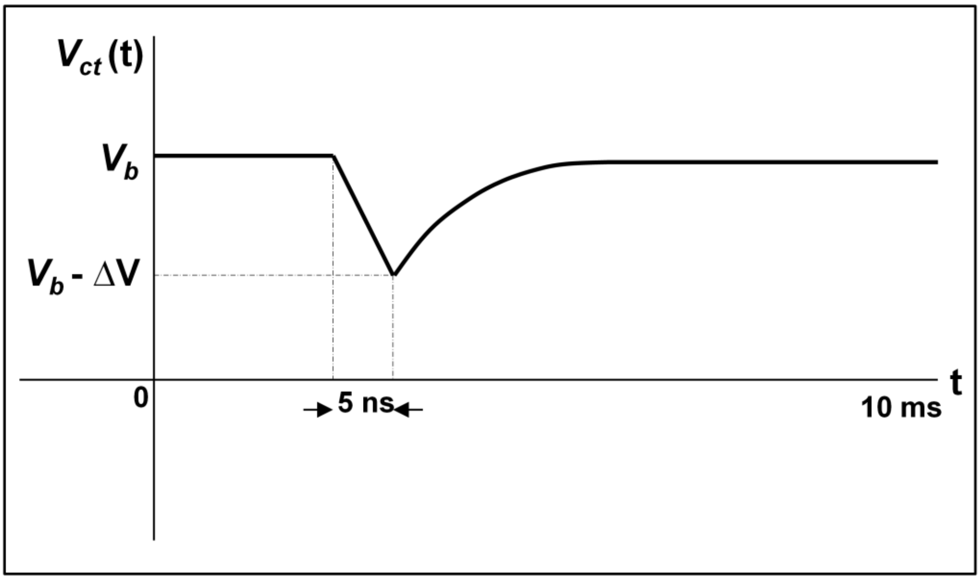

Figure 4.9: Expected voltage measured across the spherical capacitor under pulsed radiation conditions

- **Capacitance of the spherical capacitor**

Applying Gauss' law the radial electric field, ξ, supported between the two spherical plates of the capacitor is given by equation 4.3 (Griffiths, 1999:105; Paul, 2004:80),

$$\xi = \frac{Q}{4\pi\varepsilon_o r^2}$$

Equation 4.3

where r is the radial distance from the origin of the spheres.

The voltage difference between the two plates capacitor, V_{co}, can be determined by integrating the electric field over the distance between the two plates, as given by equation 4.4 (Griffiths, 1999:105),

$$V_{co} = -\frac{Q}{4\pi\varepsilon_o}\int_a^b \frac{1}{r^2} d_r = -\frac{Q}{4\pi\varepsilon_o}\left[\frac{1}{b} - \frac{1}{a}\right] = \frac{Q}{4\pi\varepsilon_o}\cdot\frac{b-a}{ba}.$$

Equation 4.4

From equations 4.2 and 4.4 the capacitance of the two plate spherical capacitor is given by equation 4.5 (Griffiths, 1999:105; Paul, 2004:120),

$$C = \frac{Q}{V_{co}} = 4\pi\varepsilon_o \cdot \frac{ba}{b - a}$$

Equation 4.5

where "*a*" is the radius of the inner sphere (MS) and "*b*" is the effective radius of the outer sphere (combined IGS and OGS).

From equation 4.5 the calculated capacitance of the two plate spherical capacitor is approximately 20 pF. This gives an expected *RC* time constant of 10 ns with an external 500 Ω resistor. This shows that the expected *RC* time constant is longer than the pulse width (5 ns) of the VUV laser radiation. As a result, the terminal voltages pulses are stretched to about 25 ns. In addition, after a few *RC* time constants, the capacitor will fully revert to its steady state condition.

4.3.1.2 Determination of the terminal voltage

For UV light at wavelengths between 140 nm and 180 nm, the estimated quantum efficiency (*QE*) of the copper plate ranges between 10^{-2} and 10^{-3} (Davis *et al*., 1993:2978; Dowell *et al*., 2006:7; Schmerge *et al*., 2007:4076−4077). Consequently, the number of electrons, $N_{electrons}$, dislocated from the copper plate due to the photoelectric effect during each pulse is calculated as follows (Sze, 1981:745; Naderi & Hashim, 2013:361; Saron *et al*., 2013:95)

$$N_{electrons} = \frac{E_{pulse} \times QE}{\hbar\omega} = 7.424 \times 10^{7} \text{ electrons per pulse}$$

Equation 4.6

where $E_{pulse} = 10\,\text{nJ}$ is the energy per pulse, $QE = 10^{-2}$ is the estimated quantum efficiency of copper and $\omega = 2\pi c/\lambda$ is the frequency of the 140 nm laser source.

The expected change in charge on the capacitor is then calculated as

$$\Delta Q = N_{electrons} \times e = 11.9 \times 10^{-12}\text{ C}$$

Equation 4.7

where $e = 1.6 \times 10^{-19}$ [C] is the unit electron charge.

Furthermore, the expected change in voltage, ΔV, of the two plate spherical capacitor can be estimated from equation 4.7 as

$$\Delta V = \left(\frac{\Delta Q}{C}\right) = \frac{11.9\times10^{-12}}{20\times10^{-12}} = 595 \text{ mV} . \qquad \textbf{Equation 4.8}$$

- **Important note**

The initial tests with the effective two plate spherical capacitor (SEPS sensor) did not yield any results due to electrons escaping the MS too fast and not being collected by the combined grids (inner and outer). The inner grid (middle) is instrumental in slowing down the electrons whilst not stopping them completely so that they can be collected by the outer grid (OG). For these purposes, the inner grid is biased at a negative potential and the outer grid is biased at a positive potential. Therefore, the inner and outer grids are not combined in the subsequent experiments. However, the two plate model does provide insight into the fundamental capacitive operation of the SEPS and the order of magnitude of the voltage pulses that can be expected. In the two plate model, it is essentially assumed that all electrons are collected by the outer grid.

4.3.2 VUV pulsed laser experiment with the planar sensor

The planar sensor is designed to minimise the experimental uncertainty observed with the complex structure of the SEPS sensor. The planar sensor is also well suited for fitment on the side of a CubeSat for directional measurement of VUV radiation.

4.3.2.1 Description of the circuit model

Like the SEPS sensor, the planar sensor under pulsed VUV conditions is modelled as the circuit in Figure 4.7. The measurement setup implemented for this sensor is shown in Figure 4.10. In this setup, the MP, IG and OG planar sensor probes form a set of two capacitors connected in series. The negatively biased IG (middle probe) is used to decelerate the electrons from the MP. The IG is required since the two plate approximation depends on ‘catching’ all the electrons at the positive OG.

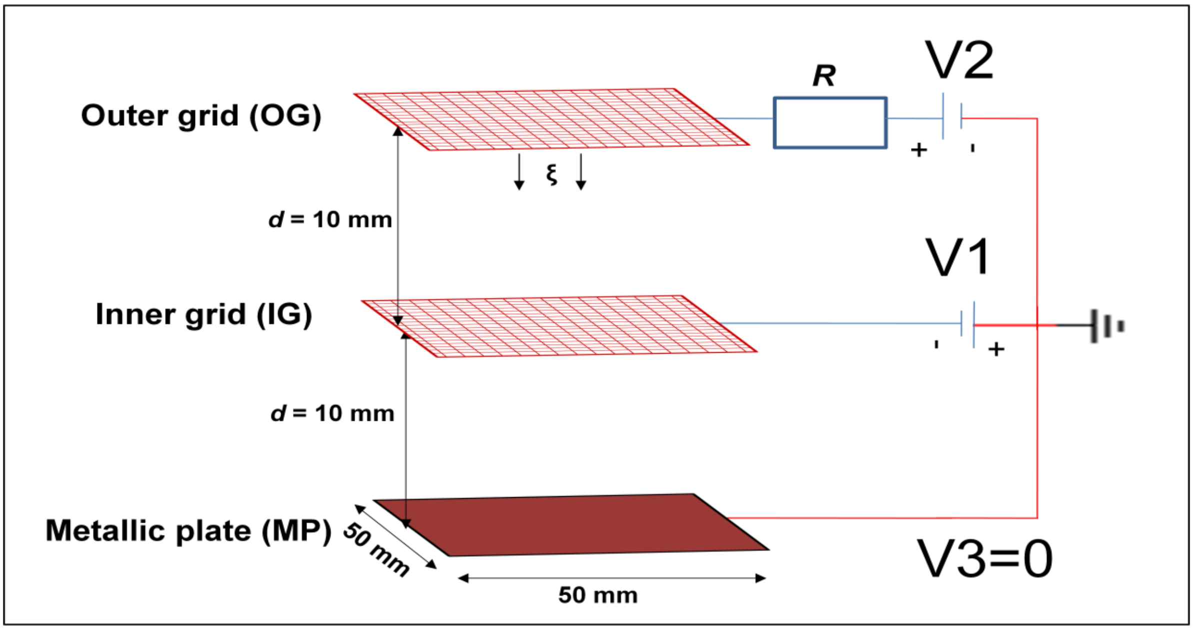

Figure 4.10: Circuit of the planar sensor under exposure to VUV pulsed laser radiation experiment

From equation 2.45 and Table 3.2 the calculated and simulated stopping potential of copper at 140 nm is approximately -4 V. As a result, stopping potentials of -5 V and -10 V are selected as two experimental scenarios. These potentials are chosen because the planar sensor grids are transparent and not all electrons will actually be stopped by the theoretical stopping potential of -4 V. Only those electrons emanating from the MP directly below the individual wires of the grid will be stopped by the -4 V stopping potential. For electrons emanating from the MP in between the individual wires, a higher stopping voltage, V_{stop}, is required due to the lower electric field at those points (Figure 4.11).

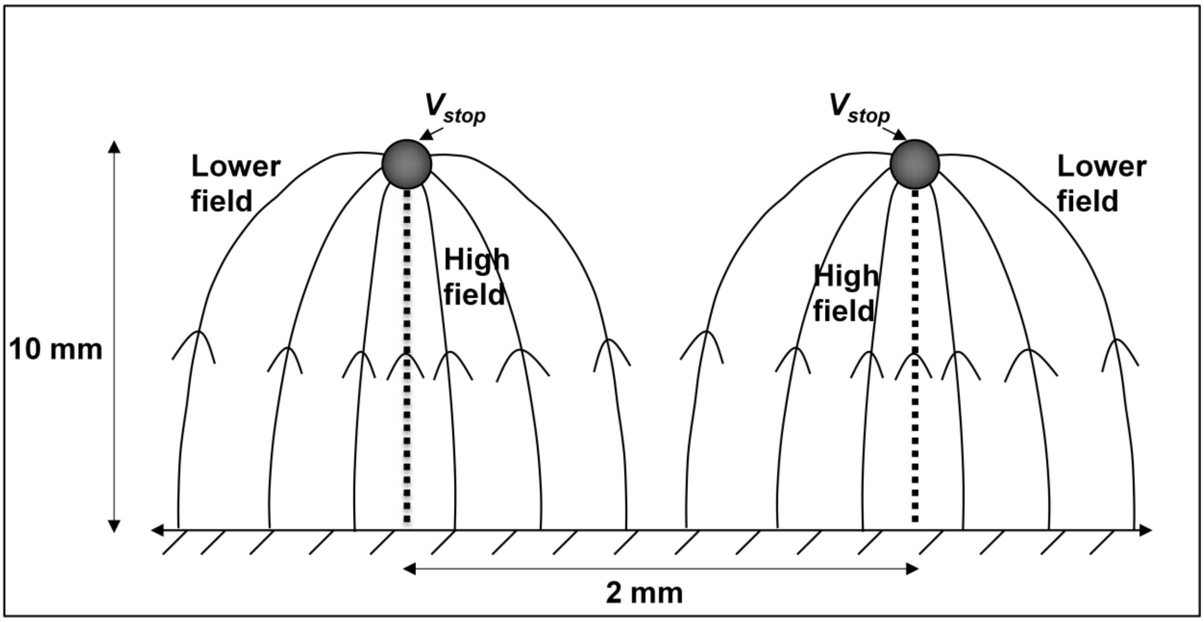

Figure 4.11: Electric field lines between the MP and the IG

In the first experiment the MP electrode (ground electrode), the IG and OG electrodes are biased at V3 = 0 V, V1 = -5 V and V2 = +8 V, respectively. In the second experiment the MP, IG and OG electrodes are biased at V3 = 0 V, V1 = -5 V and V2 = +16 V, respectively. In the third experiment the MP, IG and OG electrodes are biased at V3 = 0 V, V1 = -10 V and V2 = +16 V, respectively. In these experiments, the negative stopping voltage, V1, applied to the IG electrode is used to decelerate the electrons emitted from the MP electrode, while the positive voltage, V2, applied to the OG electrode is used to attract the decelerated electrons.

The output voltage of the sensor is analysed in both the time and frequency domains, as discussed in section 4.4.2.

- **Capacitance of the planar sensor**

The triple probe planar sensor is effectively two series connected capacitors, each with capacitance (Griffiths, 1999:105)

$$C = \frac{\varepsilon_o A}{d} \qquad \textbf{Equation 4.9}$$

$$C = 2.21 \text{ pF}$$

where d is the separation distance between the probes and A is the area of the probes.

The overall capacitance of the sensor is therefore

$$C = \frac{2.21 \times 10^{-12}}{2} = 1.1 \text{ pF}.$$

This gives an expected *RC* time constant of 0.55 ns which will ensure that the capacitor recharges completely after each pulse. The smaller *RC* time constant, than for the spherical probe, means the output voltage pulses will be shorter; of the order 5 ns long.

4.3.2.2 Determination of the terminal voltage

The expected change in voltage, ΔV, of the planar sensor can be determined using equation 4.8,

$$\Delta V = \left(\frac{\Delta Q}{C}\right) = \frac{11.9 \times 10^{-12}}{1.1 \times 10^{-12}} = 11 \text{ V}.$$

Here it is assumed that all electrons dislodged from the MP are deposited on the positive OG. The expected terminal voltage, V_p (t), measured across the planar sensor is shown in Figure 4.12. In the laboratory experiments, the time-averaged output voltage of the sensor is used as an indicator of radiation. With the short time constant, the output voltage can be approximated as a triangular pulse of height 11 V and duration 5 ns. It has a repetition of

10 Hz. The time-averaged output voltage can therefore be expected to be of the order 0.3 µV.

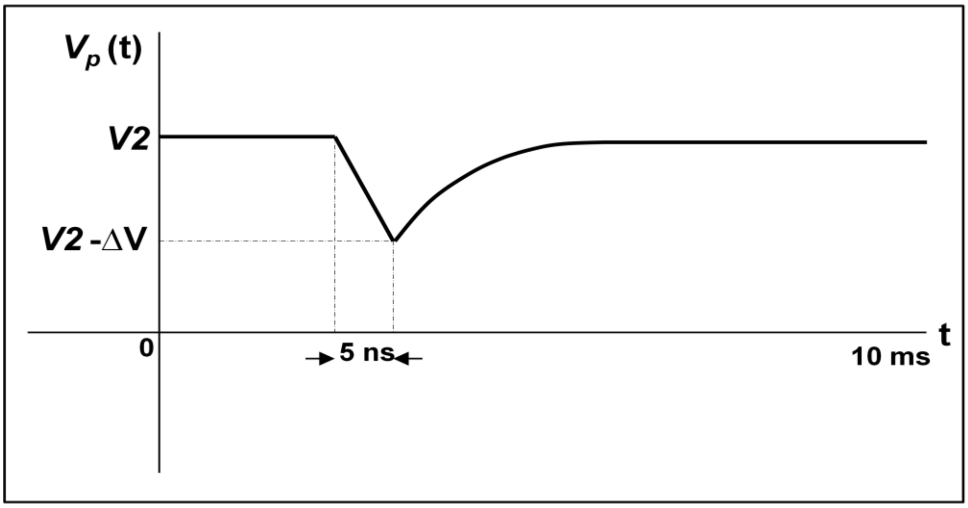

Figure 4.12: Expected terminal voltage of the planar sensor under pulsed laser radiation conditions

4.3.3 VUV deuterium lamp radiation setup for the planar sensor

4.3.3.1 Description of the circuit model

The circuit model is the same as that used for the pulsed laser experiment in Figure 4.10. The metallic plate (MP) is grounded, and the outer grid (OG) is positively biased to collect the electrons. The inner grid (IG) is negatively biased to decelerate the electrons. The aim of the experiment is to measure the terminal voltage across a 500 Ω load resistor when exposed to the VUV deuterium lamp radiation. Similar to the VUV pulsed laser experiment (section 4.3.2.1), the chosen stopping potentials of copper to decelerate electrons in the VUV deuterium lamp radiation experiment are -5 V and -10 V. However, in this case, the spectrum of the VUV deuterium lamp ranges from 116 nm to 410 nm. The stopping potentials of copper corresponding to the spectral content between 116 nm and 264 nm are, respectively, between -6 V and -0.01 V. For UV wavelengths ranging from 265 nm to 410 nm, no stopping potential is required since copper only emit electrons at a UV wavelength below 264 nm (equation 2.45 and Table 3.2).

The first experiment conducted served as a control experiment. In this experiment, no irradiation with VUV is performed and the MP electrode (ground electrode), the IG and OG electrodes are biased at V3 = 0 V, V1 = -10 V and V2 = +15 V, respectively. In the second experiment (irradiation with VUV is performed), the MP, IG and OG electrodes are again biased at V3 = 0 V, V1 = -10 V and V2 = +15 V, respectively. In the third experiment (VUV irradiation performed), the MP, IG and OG electrodes are biased at V3 = 0 V, V1 = -5 V and V2 = +10 V, respectively.

4.3.3.2 Determination of the photocurrent

Under steady radiation, the MP will emit a steady stream of electrons. The determination of this electron 'current' depends on parameters such as the radiation intensity (energy flux) and power received at the sensor. In order to estimate the maximum photocurrent produced by the VUV deuterium light, it is important to determine its spectral radiant intensity (SRI), which varies with wavelength. The effective SRI can be obtained by integrating over the entire wavelength spectrum (116 nm to 410 nm). The SRI results are collected at 0.2 nm increments from 116 nm to 169.8 nm; and at 2 nm increments from 170 nm to 410 nm (McPherson Inc, n.d.). The graphical representation of the SRI of the VUV deuterium light is shown in Figure 4.13.

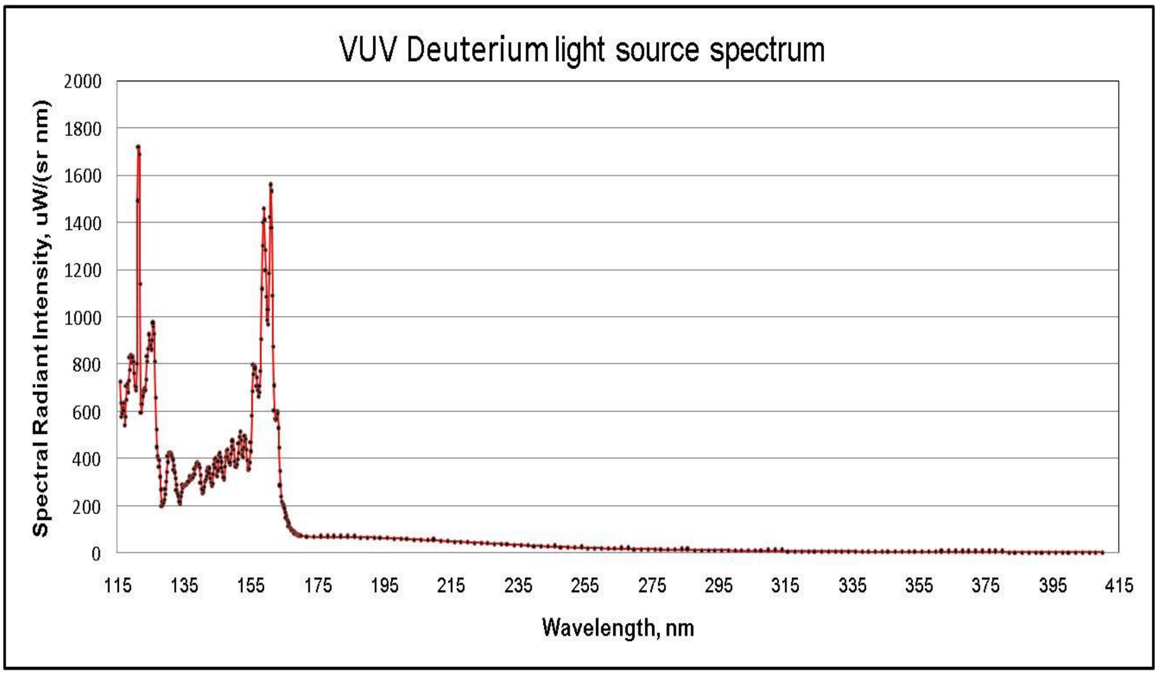

Figure 4.13: The measured SRI of the VUV deuterium lamp (Adapted from McPherson Inc, n.d.)

The effective SRI of the lamp can now be used to determine the photocurrent expected from the sensor terminal. The determination of the photocurrent is based on the solid angle, Ω, of the light from the monochromator that illuminates the copper planar sensor, as shown in Figure 4.14. The solid angle, Ω, is determined using equation 4.10 (Kirkpatrick, 2005:22),

$$\Omega = \frac{A_{spot\ lamp}}{r^2} = \frac{\pi d^2}{4r^2} = 0.038\ \text{sr} \qquad \textbf{Equation 4.10}$$

where Ω is expressed in sr, $A_{spot\ lamp}$ is the light spot area exiting the monochromator, and r is the distance from the monochromator to the clear aperture of the lamp.

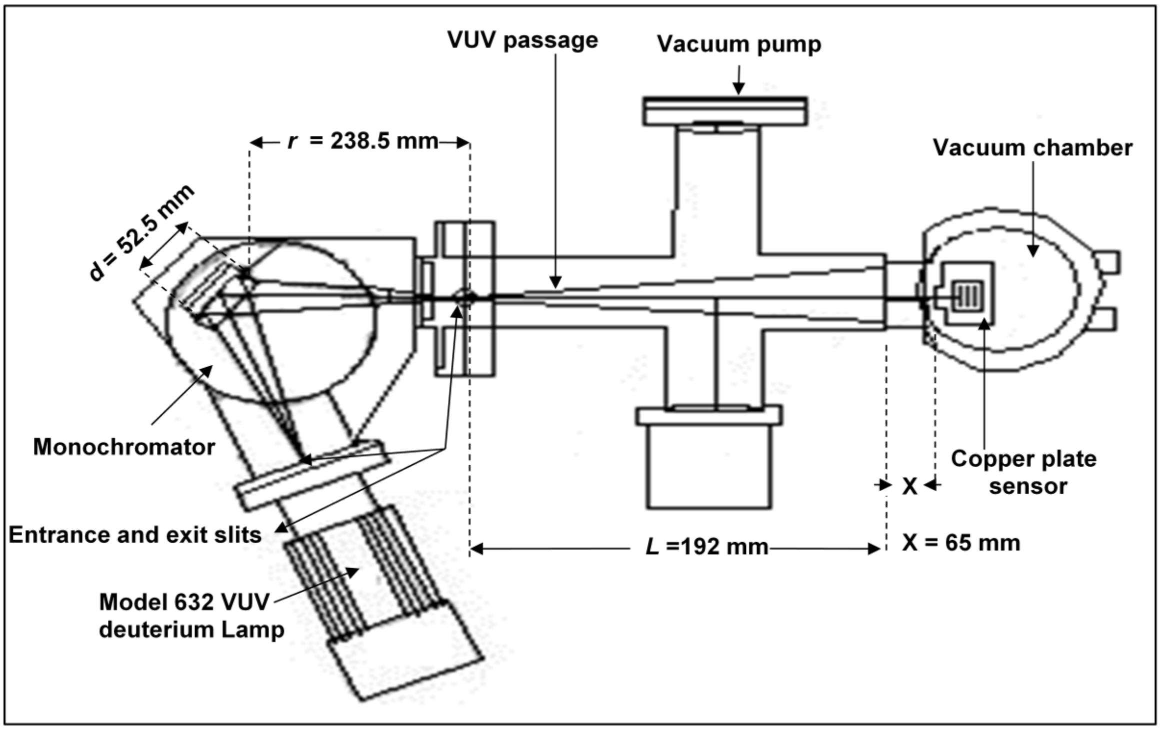

Figure 4.14: Schematic layout of the VUV deuterium light radiation experiment setup

The power, P, received at the sensor is given by equation 4.11 (Yablonovitch & Cody, 1982:302; Lee *et al*., 1990:403; Kirkpatrick, 2005:23),

$$P = \Omega \int_{\lambda = 116\,\text{nm}}^{410\,\text{nm}} \text{SRI}(\lambda)\, d\lambda \qquad \textbf{Equation 4.11}$$

$$= \Omega \sum_{i=1}^{391} \text{SRI}_i \,.\, \Delta\lambda_i$$

$$P = \sum_{i=1}^{391} P_i$$

where $\Delta\lambda_i$ is the increment in wavelength between successive SRI_i measurements of the VUV deuterium lamp, and 'i' is the index of the measured SRI_i data points (1 - 391).

The total number of photons per second, N, associated with the VUV deuterium lamp is then given by equation 4.12 (Watson *et al*., 2013:1731),

$$N = \sum_{i=1}^{391} \frac{P_i \lambda_i}{2\pi\hbar \cdot c}, \qquad \textbf{Equation 4.12}$$

$$N = \sum_{i=1}^{391} N_i \,.$$

Consequently, the expected photocurrent, I, is given by equation 4.13 (Sze, 1981:745; Naderi & Hashim, 2013:361; Saron *et al*., 2013:95),

$$I = \sum_{i=1}^{391} N_i \cdot e \cdot QE_i \qquad \textbf{Equation 4.13}$$

$$I = \sum_{i=1}^{391} I_i$$

where QE_i is the quantum efficiency of copper at wavelength λ_i.

Schmerge *et al*. (2007:4076−4077) states that as the wavelength of light decreases, the quantum efficiency of copper increases. The estimated quantum efficiency of copper at UV wavelengths (116 nm to 260 nm) varies from 10^{-2} to 10^{-3}. Above 260 nm, its quantum efficiency is less than 10^{-3} (Davis *et al*., 1993:2978; Dowell *et al*., 2006:7).

The above calculations are summarised in Table 4.1 below. From this data, the total photocurrent expected to be generated by the VUV deuterium lamp is 0.69 µA.

Table 4.1: Photocurrent calculations for the VUV deuterium lamp experiments

i	**λ_i (nm)**	**$\Delta\lambda_i$ (nm)**	**QE_i**	**SRI_i (µW nm^{-1} sr^{-1})**	**P_i (µW)**	**N_i (per second)**	**I_i (A)**
1	116.0	0.2	10^{-2}	727	5.53	3.40×10^{12}	5.44×10^{-9}
2	116.2	0.2	10^{-2}	638	4.85	2.99×10^{12}	4.78×10^{-9}
3	116.4	0.2	10^{-2}	577	4.39	2.71×10^{12}	4.33×10^{-9}
4	116.6	0.2	10^{-2}	589	4.48	2.77×10^{12}	4.43×10^{-9}
5	116.8	0.2	10^{-2}	614	4.67	2.89×10^{12}	4.63×10^{-9}
. .	. .	. .	. .	. .	. .	. .	. .
270	169.8	0.2	10^{-3}	73.2	0.56	0.50×10^{12}	8.02×10^{-11}
271	170	2	10^{-3}	72.4	5.50	4.96×10^{12}	7.94×10^{-10}
272	172	2	10^{-3}	69	5.24	4.78×10^{12}	7.66×10^{-10}
273	174	2	10^{-3}	67.6	5.14	4.74×10^{12}	7.59×10^{-10}
274	176	2	10^{-3}	67.2	5.11	4.77×10^{12}	7.63×10^{-10}
275	178	2	10^{-3}	67.3	5.11	4.83×10^{12}	7.73×10^{-10}
. .	. .	. .	. .	. .	. .	. .	. .
318	264	2	10^{-4}	18.6	1.41	1.98×10^{12}	3.17×10^{-11}
319	266	2	10^{-4}	17.9	1.36	1.92×10^{12}	3.07×10^{-11}
. .	. .	. .	. .	. .	. .	. .	. .
390	408	2	10^{-8}	2.75	0.21	0.45×10^{12}	7.24×10^{-16}
391	410	2	10^{-8}	2.73	0.21	0.45×10^{12}	7.22×10^{-16}
				Total	**1258**	**1.04×10^{15}**	**0.69×10^{-6}**

4.4 Outcomes of the VUV pulsed laser radiation experiment

4.4.1 SEPS sensor experiment

The initial VUV pulsed laser radiation experiments, with the SEPS sensor used as a two plate spherical capacitor by connecting its outer grids and positively biased, produced no voltage pulses but only significant noise levels. The absence of voltage pulses can be attributed to the fact that electrons escape the metal sphere too energetically, and may fly through the outer combined grids under the additional acceleration of the positive bias and are not collected. The noise is due to the significant ambient noise in the laboratory. A triple probe structure with a negative inner grid is necessary to slow down electrons enough to be captured by the positive outer grid. The outer grid potential also needs consideration, as electrons will again be accelerated too much if this potential is too high. No further experiments were attempted with the SEPS sensor. However, based on the same principle of operation, the simpler planar sensor was used for further experimentation. In so doing, the experimental uncertainties that are compounded by the concentric spherical construction of the SEPS sensors would be avoided. This decision was also motivated for the sake of available time for the research and the experiments.

4.4.2 Planar sensor experiments

The expected change in voltage of the planar sensor under VUV pulsed laser radiation conditions is 11 V (section 4.3.2.2). However, with the VUV pulsed laser switched on, the expected individual triangular output voltage pulses are not observed directly, possibly due to the ambient noise which causes very unstable triggering of the pulse signal. Assuming that the random nature of the ambient noise does not change with time, it should have a constant average value. Therefore, taking the time-average of the output voltage will yield a constant offset due to the noise. Any variation in the average value can then be attributed to the voltage pulses due to radiation. The respective time-averages of the measured voltages obtained from experiments 1, 2 and 3 are listed in Table 4.2. These averages of the measured voltage signals are, respectively, 30 μV, 27 μV and 27 μV.

Table 4.2: Measurement results of the planar sensor exposed to VUV pulsed laser radiation

	Experiment 1 **With VUV laser**	**Experiment 2** **With VUV laser**	**Experiment 3** **With VUV laser**
Stopping potential and accelerating voltage	V1 = -5 V, V2 = +8 V	V1 = -5 V, V2 = +16 V	V1 = -10 V, V2 = +16 V
Time-average of terminal voltage	30 μV	27 μV	27 μV

Considering equation 2.45 and Table 3.2, the stopping potential of copper at 140 nm is approximately -4 V. As a result, -5 V and -10 V are used as stopping potentials while 8 V and 16 V are used as the accelerating potentials in the experiments. Experiment 3 may be viewed as a control experiment, since with the large stopping and accelerating potentials there is negligible electron catchment on the OG. Consequently, a systemic offset of 27 µV seems present, and the output voltage due to the pulsed radiation is of the order 3 µV. Compared to the expected 0.3 µV output voltage (see section 4.3.2.2), there is a factor 10 difference between the theoretical and measured values. The relative small value of the output voltage compared to the ambient noise makes any conclusions difficult. Further calibration will be needed in future sensor development if this laboratory environment is to be used. The challenges with time domain measurement can be expected to be reduced with frequency domain analyses of the output signal, which is expected to have a characteristic spectrum. This is observed through performing a Fast Fourier Transform (FFT) on the time signals. The frequency spectra of the measured voltage signals of experiments 1, 2 and 3 are shown in Figure 4.15. In this figure, significant harmonics are observed in the three experiments at frequencies ranging from 210 MHz to 250 MHz. These frequencies exhibit consistent behaviour when the VUV laser source is switched on. Moreover, the frequency spectra is highly dependent on the shape of the VUV pulsed laser.

In experiment 1, with 8 V accelerating potential applied to the OG electrode, the maximum absolute magnitude of the spectrum obtained is 0.16 (arbitrary units). In experiment 2, with 16 V accelerating potential, the maximum is 0.10. In experiment 3, with 16 V accelerating potential, the absolute magnitude of the spectrum obtained is 0.08. The slight reduction observed in terms of magnitude in the spectrum of experiment 3 compared to experiment 2, can be attributed to the fact that the stopping potential of -10 V may be excessive to decelerate electrons and the accelerating potential (+ve) of 16 V may also be excessive to accelerate the electrons. These observations are consistent with theory where stopping potential of -4 V is predicted.

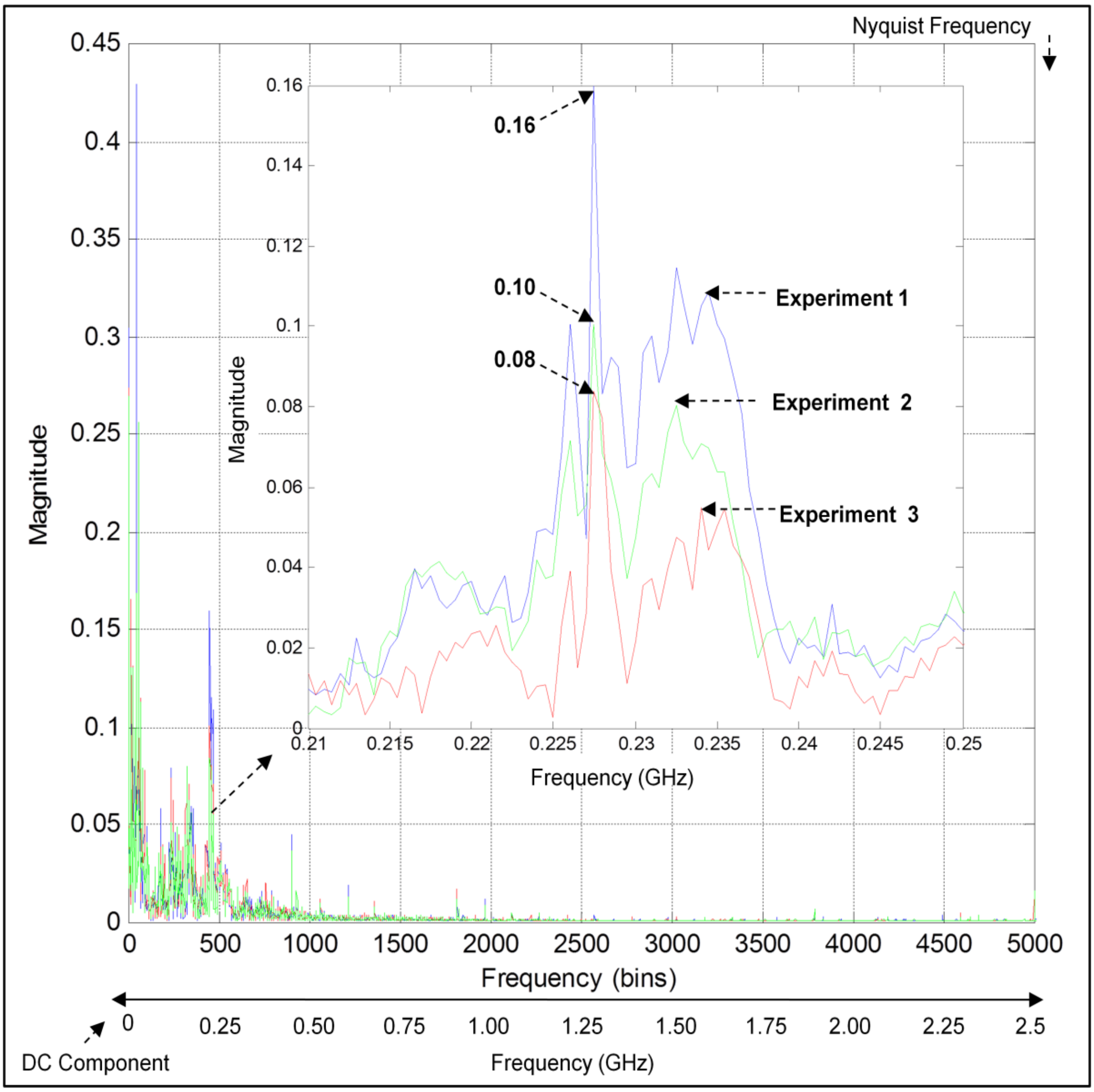

Figure 4.15: Frequency spectra of the terminal voltages of experiments 1, 2 and 3

4.5 Outcomes of the planar sensor experiments under VUV deuterium radiation

This section presents the measurement results of the VUV deuterium lamp radiation experiment. The apparatus used during the experimental setup include a multimeter, an Agilent power supply unit and an Agilent oscilloscope to capture the output signal. Figure 4.16 depicts the planar sensor circuit setup under VUV deuterium lamp radiation. The current flowing from the OG electrode is determined through measuring the voltage V_R over the 500 Ω resistor.

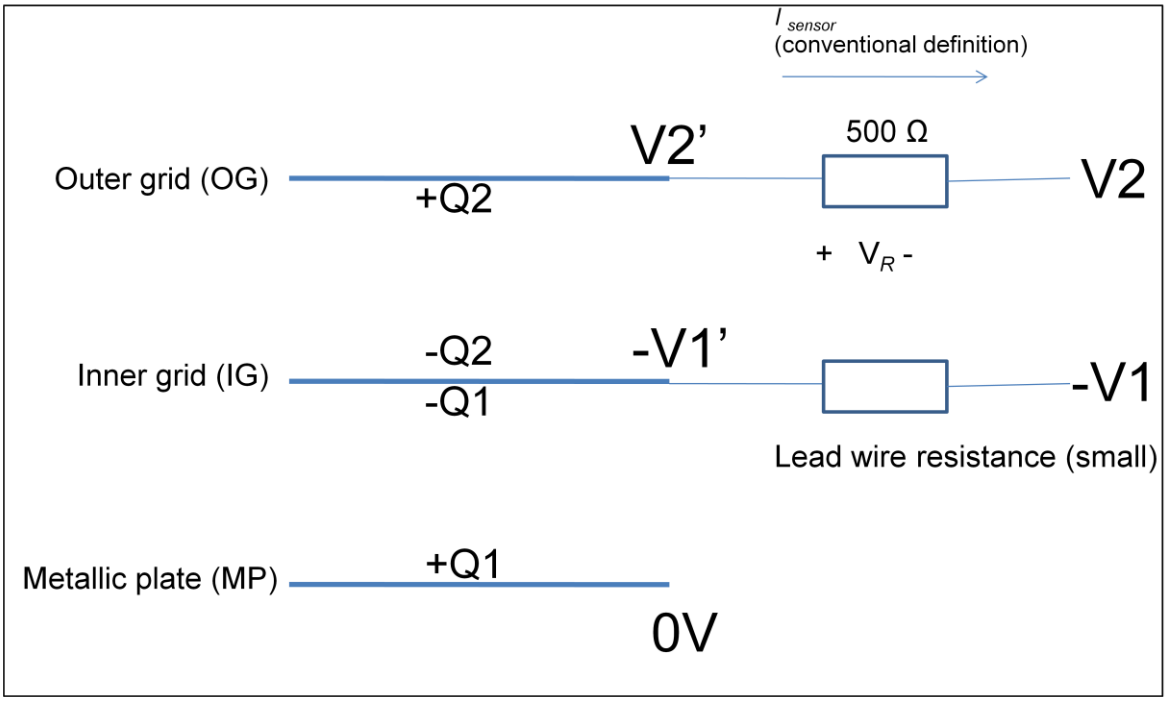

Figure 4.16: Planar sensor measurement circuit setup under VUV deuterium light

- **Control experiment**

Experiment 1 (without lamp) is used as the control experiment since there is no generation of electrons (Table 4.3). Therefore, the voltage measured across the 500 Ω resistor, *R*, is assumed to be a systemic offset voltage. The assumed measurement offset voltage is -1.01 mV. In all experiments, the actual voltage, V_{actual} , is the voltage measured across the 500 Ω, after subtracting the offset voltage. Furthermore, the sensor current, I_{sensor} , due to the photons can be determined using equation 4.14,

$$I_{sensor} = \frac{V_{actual}}{R} .$$ **Equation 4.14**

Table 4.3: Measurement results of the VUV deuterium light experiment

	Experiment 1 Without lamp	**Experiment 2 With lamp**	**Experiment 3 With lamp**
Stopping potential and accelerating voltage	V1 = -10 V, V2 = + 15 V	V1 = -10 V, V2 = +15 V	V1 = -5 V, V2 = +10 V
Time-average of V_R	-1.01 mV	-0.485 mV	-1.36 mV
Assumed measurement offset voltage	-1.01 mV	-1.01 mV	-1.01 mV
V_{actual} = Average – offset voltage	0 V	0.522 mV	-0.356 mV

- **Experiment 3 results**

From Table 4.3, after subtracting the offset voltage from the time-average of voltage V_R in experiment 3, the measured voltage is -0.356 mV. Considering equation 2.45 and Table 3.2, the stopping potentials of copper for the UV wavelengths between 116 nm and 264 nm are, respectively, between -6 V and - 0.01 V, while for the spectral content ranging from 265 nm to 410 nm, no stopping potential is required. Furthermore, at 140 nm, the stopping potential of copper is approximately -4 V. Therefore, the estimated 'stop voltage' of the electrons by the centre electrode (IG) is of the order -5 V. From the measurement results, it can be assumed that -5 V will bring most of the electrons to a standstill, and will be attracted towards the top electrode (OG), from where they flow through the 500 Ω resistor (Figure 4.16). The voltage that will be measured will therefore be negative in the conventional sense. The conventional current, I_{sensor} , obtained from experiment 3 will also be negative,

$$I_{sensor} = -\frac{3.56 \times 10^{-4}}{500} = -0.7\,\mu A .$$

This result compares very well with the theoretical calculation (0.69 μA) in Table 4.1, depending mostly on the value of copper quantum efficiency.

- **Experiment 2 results**

From Table 4.3, after subtracting the offset voltage from the time-average of voltage V_R in experiment 2, the measured voltage is 0.522 mV. From this result, the measured voltage seems to contradict the previous experiment because a positive voltage is measured. Electrons therefore do not flow away from the top electrode but rather towards it. One can assume with the lamp off that no current will flow after the two electrodes (centre and top) have charged up to $Q=CV$, i.e.,

$$Q1 = C1 \times V1 = C1 \times V1',$$

$$Q2 = C2 \times (V2 + V1) = C2 \times (V2' + V1').$$

However, when the lamp is switched on, the electrons generated by the photo electric effect will leave the grounded electrode (bottom electrode), but will be deflected back to the grounded electrode because of the stronger stopping potential (V1) than for experiment 3. Therefore, none of the created electrons will reach the top electrode. Electrons, on their return to the grounded electrode, may cause a screening effect of the positive charge on the grounded plate, effectively reducing the net charge of the bottom capacitor (+Q1 is decreased). The magnitude of the voltage V1' will therefore also decrease because Q1' = CV1'. This will cause a flow of (conventional) current from the centre electrode to V1 through the lead wires. The voltage difference between the centre and top electrodes (V2’ + V1’) will also decrease which leads to a decrease in +Q2. The charge +Q2 can only reduce if it is compensated for by electrons flowing in from V2 (capacitive effect). So the measured voltage and the conventional current, I_{sensor} , obtained from experiment 2 will be positive,

$$I_{sensor} = \frac{5.22 \times 10^{-4}}{500} = 1\ \mu A\ .$$

Comparing the results of experiments 3 and 2, the voltages measured are of the same order, but of opposite sign, i.e., the photon flux is similar in both cases. The slight difference may be because in experiment 2, the electrons are going back to the solid surface (MP) and not to the collecting grid where some of the electrons may not be attracted to the grid and are effectively lost to the experiment.

4.6 Conclusion

This chapter reported on the behaviour of copper sensor prototypes exposed to VUV radiation obtained from different sources, namely a pulsed laser and a deuterium lamp (steady light source). For this purpose, the SEPS and planar copper sensors have been constructed. The fabrication of the planar sensor is recommended because it helped not only to simplify the experimental setup but also to minimise the experimental uncertainty observed with the SEPS sensor. Consistent measurements were observed in both the pulsed and continuous radiation experiments.

CHAPTER FIVE: CONCLUSION AND RECOMMENDATIONS

5.1 Conclusion

The damaging effects of space weather on spacecraft electronics motivated the present study to develop sensors that can be used for measurement of plasma and radiation in the SAMA region. In order to measure EUV radiation and plasma parameters, the principles of developing and testing both spherical and planar sensors based on Langmuir probe theory and the photoelectric effect have been investigated. The testing procedures of such devices have been examined using facilities available in the Western Cape region (South Africa).

5.1.1 Addressing the research questions

- **EUV and VUV radiation sensors**

The focus of this study was to design, build and test plasma and radiation sensor prototypes. The SEPS sensor was chosen because it provides the ability to measure plasma and radiation omni-directionally. A planar version of the SEPS sensor prototype was also implemented because it provides the ability to measure plasma and radiation from a specific direction and is of much simpler design. The aim of this study was to investigate the sensors' electric response to plasma and EUV radiation. Plasma testing was not investigated due to the lack of test facilities in the Western Cape region. This investigation was done through modelling and simulation. The measured EUV experimental results suggest the use of the planar sensor to investigate EUV radiation in the SAMA region since a significant correlation exists with the theoretical expectation.

- **Material used to develop the sensor prototypes**

Any metallic material could be used in the fabrication of the sensors investigating the plasma and radiation in the SAMA region. However, for this study, the material of preference selected was copper because of its high conductivity, wide-spread availability and its work function (4.7 eV) which corresponds to a maximum UV wavelength of 264 nm. This wavelength also corresponds to the available VUV radiation sources at test facilities in the Western Cape. The use of short wavelengths is essential because they are comparable to EUV wavelengths (10 nm to 121 nm) in the SAMA region.

- **Adaptation of the sensors within the limitations of CubeSat design**

The prototypes have been designed to comply with a 1U CubeSat form factor. The diameters of the three concentric spheres used to construct the SEPS sensor are, respectively, 6 cm, 7cm and 8 cm while the side dimension of the three square probes used to construct the planar sensor is 5 cm. Therefore, the SEPS sensor can fit in a 1U CubeSat form factor and the planar sensor can fit on the sides of a 1U CubeSat.

- **Sensors and experimental measurement of radiation**

The SEPS and planar sensors were tested in the laboratory through the use of VUV radiation sources which mimic the actual EUV environment. Radiation was obtained from different VUV sources, namely a pulsed laser and a deuterium lamp. A major contribution of this study is related to the challenges faced with the testing of the sensors. These findings are elaborated on the sections below.

5.1.2 Simulation and modelling results

In the course of this research, simulations were conducted to determine the plasma parameters in the ionosphere's F-layer region using an ideal single spherical probe. Simulations were also conducted to study the flux and energy levels of UV radiation using a single copper plate placed in a vacuum chamber. In order to do this, MATLAB and Phet software (Phet, 2011) were used. Based on Langmuir single probe theory, numerical simulations of the ideal single spherical probe behaviour in the ionosphere's F-layer of the SAMA region were conducted. In addition, based on the photoelectric effect principle, Phet software was successfully used to simulate the behaviour of a copper plate exposed to UV radiation.

The simulation results of the ideal single spherical probe behaviour showed that ionospheric plasma parameters, such as electron temperature and density can be extracted from the $I{-}V$ characteristic curve obtained from the probe. Furthermore, the simulation results of the behaviour of a copper plate exposed to UV radiation showed that UV light with wavelengths shorter than 237 nm produced photocurrents due to a significant increase in the number of electrons ejected from the copper plate. These short wavelengths are relevant for this study since they occur in the SAMA region.

5.1.3 Experimental results

This study characterised the copper sensor prototypes and their responses to typical radiation levels within the limitations of the test facilities. The aim was to verify that theory and practical measurements agree, and that local test facilities are available for future sensor development and calibration.

- **SEPS sensor**

  For the realisation of this study, a triple probe spherical sensor prototype, implemented initially as a two plate capacitor by combining the outer grids, was constructed and the terminal voltages measured while exposed to VUV pulsed laser radiation. However, no voltage pulses were observed; only significant noise levels. The absence of voltage pulses can be attributed to the fact that electrons escaped the metal sphere too energetically, and may have flown through the outer combined grids under the additional acceleration of the positive bias and were not collected. The noise observed was due to the significant ambient noise in the laboratory. A triple probe structure with a negative inner grid is necessary to slow down electrons enough to be captured by the positive outer grid. The outer grid potential also needed consideration, as electrons would have been accelerated too much if this potential was too high. No further experiments were attempted with the SEPS sensor. However, based on the same principle of operation, the simpler planar sensor was used for further experimentation. In so doing, the experimental uncertainties that are compounded by the concentric spherical construction of the SEPS sensors would be avoided. This decision was also motivated for the sake of available time for the research and the experiments. In addition, the planar sensor has the additional advantage of directional measurement of radiation, and being attached outside the CubeSat does not occupy valuable space inside the satellite.

- **Planar sensor**

  A triple probe planar sensor prototype was developed to measure its response to VUV pulsed laser and continuous deuterium lamp radiation.

  In the pulsed VUV laser radiation experiment, the stopping potential of copper at 140 nm is approximately -4 V (equation 2.45 and Table 3.2). As a result, -5 V and -10 V were used as the stopping potentials while 8 V and 16 V were used as the accelerating potentials in the experiments. The time-averages of the measured terminal voltages were obtained. The frequency content of the measured terminal voltages also showed consistency at frequencies ranging from 210 MHz to 250 MHz for all three experiments conducted. The outcomes of these experiments were discussed in sections 4.4 and 4.5. It suffices to emphasise here the key findings regarding the probe bias voltages.

- **Key findings**

In this study, the stopping and accelerating potentials were chosen carefully. The theoretical stopping potential (approximately -4 V to -5 V) for VUV radiation measurements were validated by the experiments. Additionally, the study also found that the accelerating potential should be kept below 10 V in order to capture more electrons. This is a good reference for future sensor development. Furthermore, these stopping and accelerating potentials were consistently borne out by both pulsed and steady radiation experiments in both time and frequency domains.

5.1.4 Challenges experienced in test environment

Vacuum ultraviolet radiation measurements were performed under both pulsed and steady state conditions, but these measurements posed challenges in terms of noise. As a result, the study looked at both time and frequency domain analyses.

Pulsed radiation:

- **Challenges with time domain analyses**

In the VUV pulsed laser experiment the ambient noise in the laboratory was considerable and exceeded the current pulses generated. Although the noise has not been characterised, its offset may also fluctuate in time. The effective value of the output voltage pulse train is extremely small (of the order 0.3 µV) due to the very low duty cycle of the laser pulse. As a result, time domain analyses were not appropriate.

One option would have been to take the average of the voltage measurements over many experiments and over a set time of a few periods of the laser. In this case, it would be expected that with and without the laser, the average value of the measurements should vary. With the laser switched on, there would have been an increase compared to the no laser state. But again, these pulses were so short, that any variation in the amplitude of the pulses would not contribute significantly to the average value. So, the measurements would have been compromised by the ambient noise.

Another option considered was to measure the output voltage directly with a high frequency sampling oscilloscope while triggering it with the laser pulse signal. However, once again, the excessive ambient noise interfered and no output pulses were captured even when the average of the accumulative measurements was taken.

- **Challenges with frequency domain analyses**

In the VUV pulsed laser experiment, the frequency domain analyses seem to be more robust against the ambient noise and identify the small and short pulses in the measurements. A consistent change was noticed in the experimental outcomes at frequencies ranging from 210 MHz to 250 MHz after performing the post-processing of the measured voltage signals with FFT.

Steady state condition:

The time domain analysis was more appropriate for the steady state measurements since the noise was random and the expected output voltage constant. By taking the average of many experiments, it was easier to minimize the effect of the noise and clearly observed changes in DC levels. The measured output current agreed very well with theory.

5.2 Recommendation

The present research contributed to a pool of knowledge on plasma and radiation sensors and can serve as a reference for the building of radiation sensors that can be integrated with CubeSat subsystems. The outcomes of this research have laid a platform for future sensor development by identifying the practical challenges that are posed in terms of the facilities available, as well as experimental difficulties associated with the testing of the sensors. This research has also identified experimental complexities that need to be addressed by future researchers. Furthermore, the research has laid a solid foundation to help scientists and engineers to improve space weather monitoring and open doors to further research on radiation sensors.

REFERENCES

Aristov, V. V. 2009. The photoelectric effect in the semiclassical theory. *Doklady Physics*, 54(4):171-173.

Asselin, D.J. 2011. Characterization of the near-plume region of a low-current hollow cathode. Unpublished MSc dissertation, Worcester Polytechnic Institute, Worcester.

Barjatya, A. 2007. Langmuir probe measurements in the ionosphere. Unpublished PhD dissertation, Utah State University, Utah.

Barth, J.L., Dyer, C. & Stassinopoulos, E. 2003. Space, atmospheric and terrestrial radiation environments. *IEEE Transactions on Nuclear Science*, 50(3):466-482.

Bell, T. 2013. Electrical Conductivity in Metals. In *about.com metals* [online]. Available: http://metals.about.com/od/properties/a/Electrical-Conductivity-In-Metals.htm
[Accessed 12 April 2013].

Brunner, R., Schmidtke, G., Konz, W., Lambrecht, A. & Pfeffer, W. 2009. Spherical EUV and plasma spectrometer (SEPS). *Presentation held at Pico and Nano Satellites: Technologies for Small Satellite Research*, Fraunhofer, 1-2 Oct 2009. Germany: University Würzburg:1-29.

Brunner, R., Schmidtke, G., Hilgers, A. & Pfeffer, W. 2011. Spherical EUV and Plasma Spectrometer (SEPS-LEED) – typical measurement results and modelling. In *SEPS_SPINE Workshop* [online]. Available:
http://dev.spis.org/projects/spine/home/meeting/mxvii/data2/session3/SEPS_SPINE_Workshop_-_17-19_January_-_IRF_Uppsala-Part1_pdf
[Accessed 31 0ctober 2011].

Casadio, S. & Arino, O. 2011. Monitoring the South Atlantic Anomaly using ATSR instrument series. *Advances in Space Research*, 48(6):1056-1066.

Chen, F.F. 1984. *Introduction to plasma physics and controlled fusion*. 2nd ed.
New York: Plenum Press.

Chen, F.F. 2003. Langmuir Probe Diagnostics: Mini-Course on Plasma Diagnostics, IEEE-ICOPS meeting. Jeju: Korea. [Unpublished course note].

Chen, S. & Sekiguchi, T. 1965. Instantaneous direct-display system of plasma parameters by means of triple probe. *Journal of Applied Physics*, 36(8):2363-2375.

Cox, P. A. 1996. *Introduction to quantum theory and atomic structure*. Oxford: Oxford University Press.

Davis, P., Hairapetian, G., Clayton, C., Joshi, C., Hartman, S., Park, S. & Rosenzweig, J. 1993. Quantum efficiency measurements of a copper photocathode in an RF electron gun. *In Particle Accelerator Conference, 1993, Proceedings of the 1993,* Washington DC, 17-20 May 1993. USA: IEEE: 2976-2978.

Deline, C.A. 2008. Characterization of the magnetic nozzle region of high powered electric propulsion thrusters using numerical simulation, RF interferometry and electrostatic probes. Unpublished PhD dissertation, University of Michigan, Michigan.

De Santis, A. & Qamili, E. 2010. Equivalent monopole source of the geomagnetic South Atlantic anomaly. *Pure and Applied Geophysics*, 167(3):339–347.

Dowell, D. H., King, F. K., Kirby, R. E., Schmerge, J. F. & Smedley, J. M. 2006. In situ cleaning of metal cathodes using a hydrogen ion beam. *Physical Review Special Topics-Accelerators and Beams*, 9(6):1-8.

Düsterer, S. 2002. Laser plasma interaction in droplet targets. Unpublished PhD dissertation, University of Jena, Jena.

Eckman, R.F. 1999. Langmuir probe measurements in the plume of a pulsed plasma thruster. Unpublished MSc dissertation, Worcester Polytechnic Institute, Worcester.

Escobar, A.C. 2009. A Langmuir probe instrument for research in the terrestrial Ionosphere. Unpublished MSc dissertation, Pennsylvania State University, United State.

F'SATI. 2013. CubeSat. In *F'SATI* [online]. Available: http://www.cput.ac.za/blogs/fsati/cubesat/ [Accessed 31 December 2013].

Ginet, G.P., Madden, D., Dichter, B.K. & Brautigam, D.H. 2007. Energetic Proton Maps for the South Atlantic Anomaly. *Radiation Effects Data Workshop,* Honolulu, HI, 23-27 July 2007. Hawaii: IEEE: 1-8.

Griffiths, D. J. 1999. *Introduction to Electrodynamics*. 3rd ed. New Jersey: Prentice-Hall.

Grill, A. 1994. *Cold plasma in materials fabrication: from fundamentals to applications*. New York: IEEE Press.

Hamzavi, S., Hilgers, A., Lebreton, J.P. & Dovner, P.O. 1996. Langmuir probe plasma measurements reduction using a feed-forward neural network: Preliminary results. *ESA Symposium Proceedings on Environment Modelling for Space-based Applications*, ESTEC, 18-20 September 1996. Noordwijk: Netherlands: 207-212.

Hannum, D.A. 2010. Characterizing the plasma of the Rotating Wall Machine. Unpublished PhD dissertation, University of Wisconsin, Madison.

Heirtzler, J.R. 2002. The future of the South Atlantic anomaly and implications for radiation damage in space. *Journal of Atmospheric and Solar-Terrestrial Physics*, 64(16):1701-1708.

Hunsucker, R.D. & Hargreaves, J.K. 2003. *The high-latitude ionosphere and its effects on radio propagation*. Cambridge: Cambridge University Press.

HyperPhysics. 2013. Work Functions for Photoelectric Effect. In *hyperphysics* [online]. Available: http://hyperphysics.phy-astr.gsu.edu/hbase/tables/photoelec.html
[Accessed 16 March 2013].

Ji, H., Toyama, H., Yamagishi, K., Shinohara, S., Fujisawa, A. & Miyamoto, K. 1991. Probe measurements in the REPUTE-1 reversed field pinch. *Review of Scientific Instruments*, 62(10):2326-2337.

Kelly, A., Jahn, R. & Tilley, D. 1990. The Application of the Triple Probe Method to MPD Thruster Plumes. *21st International Electric Propulsion Conference*, Orlando, Florida, 18-20 July 1990. USA: Princeton University Press: 1-11.

Kirkpatrick, S. J. 2005. A primer on radiometry. *Dental Materials*, 21(1):21-26.

Kotova, G. 2007. The Earth's plasmasphere: State of studies (a Review). *Geomagnetism and Aeronomy*, 47(4):409-422.

Lee, H. C., Breneman, E. J. & Schulte, C. P. 1990. Modelling light reflection for computer color vision. *IEEE Transactions on Pattern Analysis and Machine Intelligence*, 12(4):402-409.

Liboff, R. L. 1980. *Introductory quantum mechanics*. San Francisco: Holden-Day.

Lyons, L.A. 2007. Construction and operation of a Mirror Langmuir Probe diagnostic for the Alcator C-Mod tokamak. Unpublished MSc dissertation, Massachusetts Institute of Technology, Cambridge.

Mackel, F., Kempkes, P., Tenfelde, J., Ridder, S. & Soltwisch, H. 2013. Triple Probe Measurements Benchmarked by Interferometry in a Pulsed-Power Plasma. *Contributions to Plasma Physics*, 53(1):33-38.

Mavromichalaki, H., Souvatzoglou, G., Sarlanis, C., Mariatos, G., Plainaki, C., Gerontidou, M., Belov, A., Eroshenko, E. & Yanke, V. 2006. Space weather prediction by cosmic rays. *Advances in Space Research*, 37(6):1141-1147.

Mavromichalaki, H., Papaioannou, A., Mariatos, G., Papailiou, M., Belov, A., Eroshenko, E., Yanke, V. & Stassinopoulos, E.G. 2007. Cosmic ray radiation effects on space environment associated to intense solar and geomagnetic activity. *IEEE Transactions on Nuclear Science,* 54(4):1089-1096.

McPherson Inc. n.d. Model 632 Vacuum Ultraviolet deuterium Light Source. In *McPherson Monochromator & Spectrometer Home Page* [online]. Available: http://mcphersoninc.com/lightsources/632.pdf [Accessed 25 August 2013].

Merlino, L.M. 2007. Understanding Langmuir probe current-voltage characteristics. *American Journal of Physics,* 75(12):1078-1081.

Millikan, R. 1916. A direct photoelectric determination of Planck's "h". *Physical Review*, 7(3):355-388.

Miyamoto, K. 2000. *Fundamentals of plasma physics and controlled fusion*. Tokyo: Iwanami Book Service Center.

Naderi, N. & Hashim, M. 2013. Porous-shaped silicon carbide ultraviolet photodetectors on porous silicon substrates. *Journal of Alloys and Compounds*, 552(5):356-362.

Ota, K. Watanabe, Y. Banine, V. & Franken, H. 2006. EUV Source Requirements for EUV Lithography. In *EUV sources for lithography*. Edited by Bakshi, V.B: SPIE Press. 1-1045.

Pace, D.C. 2009. Spontaneous thermal waves and exponential spectra associated with a filamentary pressure structure in a magnetized plasma. Unpublished PhD dissertation, University of California, Los Angeles.

Paul, C.R. 2004. *Electromagnetics for engineers: with applications to digital systems and electromagnetic interference*. New Jersey: John Wiley & Sons.

Phet. 2011. Photoelectric effect. In *Phet Interactive simulations* [online]. Available: http://phet.colorado.edu/en/simulation/photoelectric [Accessed 16 March 2013].

Rae, A. I. M. 2002. *Quantum mechanics*. 4th ed. Bristol, England: Institute of Physics Pub.

Robin, L. 2006. Mysterious Radio Hiss Blamed on Space Weather. In *space.com* [online]. Available: http://www.space.com/2971-mysterious-radio-hiss-blamed-space-weather.html [Accessed 9 September 2011].

Saron, K., Hashim, M. & Farrukh, M. 2013. Growth of GaN films on silicon (111) by thermal vapor deposition method: Optical functions and MSM UV photodetector applications. *Superlattices and Microstructures*, 64:88-97.

Schmerge, J.F., Clendenin, J.E., Dowell, D.H. & Gierman, S.M. 2007. RF Gun Photo-Emission Model for Metal Cathodes Including Time Dependent Emission. *International Journal of Modern Physics A*, 22(23):4069-4082.

Siingh, D., Singh, R., Kamra, A., Gupta, P., Singh, R., Gopalakrishnan, V. & Singh, A. 2005. Review of electromagnetic coupling between the Earth's atmosphere and the space environment. *Journal of Atmospheric and Solar-Terrestrial Physics*, 67(6):637-658.

Simmons, M.R. 2008. Remote Sensing with CubeSats. In *Mattew Simmons Papers* [online]. Available: http://www.matthewsimmons.org/papers/CubeSats-Simmons.pdf [Accessed 18 May 2012].

Sinclair, B.C. 2005. Langmuir Probe Diagnostics of the VASIMR Engine. Unpublished MSc dissertation, Naval Postgraduate School, California.

Sirajuddin, D. 2007. Langmuir Probe: Determination of Plasma Parameters of a Neon DC Plasma Using a Langmuir Probe. Available: http://www.itcanbeshown.com/NERS425/Lab3/Langmuir%20Probe%20I.pdf [Accessed 20 June 2012].

Stassinopoulos, E.G. & Raymond, J.P. 1988. The space radiation environment for electronics. *IEEE Transactions on Nuclear Science,* 76(11):1423-1442.

Sze, S. M. 1981. *Physics of semiconductor devices*. 2nd ed. New York: John Wiley & Sons.

Tilley, D.L., Gallimore, A.D., Kelly, A.J. & Jahn, R.G. 1994. The adverse effect of perpendicular ion drift flow on cylindrical triple probe electron temperature measurements. *Review of Scientific Instruments*, 65(3):678-681.

Tobiska, W.K. & Nusinov, A.A. 2000. Status of the draft ISO solar irradiance standard. *Physics and Chemistry of the Earth, Part C: Solar, Terrestrial & Planetary Science*, 25(5-6):387-388.

Tobiska, W.K. & Nusinov, A.A. 2005. Status of ISO draft international standard for determining solar irradiances (DIS 21348). *Advances in Space Research*, in review. Available: http://www.spacewx.net/pdf/C01_0014_04.pdf [Accessed 7 October 2013].

Tobiska, W.K. & Bouwer D.S. 2006. New developments in SOLAR2000 for space research and operations. *Advances in Space Research*, 37(2):347-358.

Visser, D. F. 2009. CPUT CubeSat – Mission requirements and technical specifications. Unpublished. Cape Town: Cape Peninsula University of Technology.

Watson, C., Devynck, M. & Taylor, D. 2013. Photon-Assisted Capacitance-Voltage Study of Organic Metal-Insulator-Semiconductor Capacitors. *Organic Electronics*, 14(7):1728-1736.

Weyde, C. 2006. Plasma parameters from the Rosetta LAP instrument. Unpublished MSc dissertation, Uppsala University, Sweden.

Yablonovitch, E. & Cody, G. 1982. Intensity enhancement in textured optical sheets for solar cells. *IEEE Transactions on Electron Devices*, 29(2):300-305.

Zettili, N. 2009. *Quantum mechanics: concepts and applications*. 2nd ed. Chichester: John Wiley & Sons.

APPENDICES

APPENDIX A: Matlab code

A.1 Current-voltage characteristic curve of an ideal single spherical probe

```
%%%%%%%%%%%%%%%%%%%%%%%%%%%%%%%%%%%%%%%%%%%%%%%%%%%%%%%%%%
%*Ayeleso Ayokunle *                                                                      %
%*211014788 *                                                                             %
%                                                                                         %
% M-file code for ideal Langmuir probe current to voltage characteristics using atomic oxygen ions   %
 %plasma                                                                                  %
 %%%%%%%%%%%%%%%%%%%%%%%%%%%%%%%%%%%%%%%%%%%%%%%%%%%%%%%%%%

clc;clear all;close all;

set (0,'DefaultAxesFontSize',14)

 Vp=1; K_B=1.38e-23;                      % Plasma potential and Boltzmann's constant (m2 kg
                                          % s-2 K-1)
Te=0.26*11604;                            % Electron temperature, unit (K)
Ti=0.1*11604;                             % Ion temperature, unit (K)
e=1.6e-19;                                % Electron charge, Unit Coulombs
ne=1e12; ni=1e12;                         % Electron & ion densities, unit (m^-3)
e0=8.85*10^-12;                           % Free space, Unit (m-3 kg-1 s4 A2)

ve=sqrt(8*K_B*Te/(pi*9.1e-031));          % Electron velocity
Aprobe=4*pi*(80e-3/2)^2;                  % Surface area of a spherical probe

Ies=1/4*e*ne*ve*Aprobe                    % Electron-saturation current
Iis=0.6*e*ni*sqrt(K_B*Te/2.64e-26)*Aprobe; % Bohm ion current

Ies/Iis;                                  % The ratio between I_isat and I_esat

p=0.6*sqrt(2*pi)
T=sqrt(2.64e-26/9.1e-031)
M=T/p                                      % M is also the ratio between I_isat and I_esat

VB=-15:0.01:10;                            % Bias voltage range

I_e=Ies*exp(-e*(Vp-VB)./( K_B*Te));
I_i=-Iis*exp(e*(Vp-VB)./( K_B*Ti));
Ii=-Iis;
Ie1=I_e(find(VB<=Vp));
Ie2=I_e(find(VB>Vp))*0+Ies;

Ie=[Ie1,Ie2];                             % Electron current
Ii1=I_i(find(VB>=Vp));
Ii2=I_i(find(VB<Vp))*0-Iis;
Ii=[Ii2,Ii1];                             % Ion current

I=Ie+Ii;                                  % Probe current

%****************************************To calculate the Debye length************************************

Debye_Length=69*sqrt((Te/ne))             % Debye length calculation
```

```
%*****To calculate electron temperature, floating probe potential and plasma potential***************

Vf=Vp+(KB*Te/e)*log(0.6*sqrt(2*pi*9.1e-031/2.64e-26))   % Floating probe potential
Vp=Vf-((KB*Te/e)*log(0.6*sqrt(2*pi*9.1e-031/2.64e-26)))  % Plasma potential

Te=e*(Vf-Vp)/(KB*log(0.6*sqrt(2*pi*9.1e-031/2.64e-26))) % Electron temperature


%*****************************************************Plot**************************************************
plot(VB,I/1e-3,'LineWidth',3); hold all          % Plot for the probe current
plot(VB,13*I/1e-3,'LineWidth',2);                % Plot for the magnified probe current
axis([-15 10 -0.05 0.35]);                       % for axis trimming

%******************************Title ('Ideal Langmuir current to voltage characteristics')*****************

ylabel('Current (mA)')                           % y- axis labelling
Xlabel('Probe voltage  (Vb)')                    % x- axis labelling
grid
```

A.2 Simulated photocurrent vs collector bias voltage at 237 nm wavelength

```
%%%%%%%%%%%%%%%%%%%%%%%%%%%%%%%%%%%%%%%%%%%%%%%%%%%%%%%%%%%%%%
%                                                                     %
%*Ayeleso Ayokunle *                                                  %
%*211014788 *                                                         %
%                                                                     %
% *M-file code for the simulated photocurrent vs collector bias voltage at 237 nm*     %
%%%%%%%%%%%%%%%%%%%%%%%%%%%%%%%%%%%%%%%%%%%%%%%%%%%%%%%%%%%%%%

clc;clear all;close all;

set (0,'DefaultAxesFontSize',14)


Current=[0.018,0.018, 0.018,0.018,0.018,0.000,0.000,0.000,0.000,0.000,0.000,0.000,0.000,0.000,
0.000,0.000,0.000,0.000,0.000,0.000,0.000,0.000,0.000,0.000,0.000,0.000,0.000,0.000,0.000]

Voltage= [8.0,6.0,4.0,2.0,0.0,-0.2,-0.4,-0.6,-0.8,-1.0,-1.2,-1.4,-1.6,-1.8,-2.0,-2.2,-2.4,-2.6,-2.8,-3.0,-3.2,-
3.4,-3.6,-3.8,-4.0,-5.0,-6.0,-7.0,-8.0]

%**********************************************Plot**********************************************************

plot(Voltage,Current,'LineWidth',2)              % Plot of photon current versus battery voltage

%*********************************Title ('Current versus battery voltage')***********************************

ylabel('Current (A)')                            % y- axis labelling
Xlabel('Voltage  (V)')                           % x- axis labelling
grid on
```

A.3 Simulated photocurrent vs collector bias voltage at 141 nm wavelength

```
%%%%%%%%%%%%%%%%%%%%%%%%%%%%%%%%%%%%%%%%%%%%%%%%%%%%%%%%%%%%
%                                                          %
%*Ayeleso Ayokunle *                                        %
%*211014788 *                                               %
%                                                          %
% *M-file code for the simulated photocurrent vs collector bias voltage at 141 nm*   %
%%%%%%%%%%%%%%%%%%%%%%%%%%%%%%%%%%%%%%%%%%%%%%%%%%%%%%%%%%%%

clc;clear all;close all;

set (0,'DefaultAxesFontSize',14)


Current=[0.622,0.622,0.622,0.622,0.622,0.605,0.574,0.543,0.512,0.481,0.450,0.419,0.388,0.357,0.32
5,0.294,0.263,0.232,0.201,0.170,0.139,0.108,0.077,0.046,0.000,0.000,0.000,0.000,0.000]

Voltage= [8.0,6.0,4.0,2.0,0.0,-0.2,-0.4,-0.6,-0.8,-1.0,-1.2,-1.4,-1.6,-1.8,-2.0,-2.2,-2.4,-2.6,-2.8,-3.0,-3.2,-
3.4,-3.6,-3.8,-4.0,-5.0,-6.0,-7.0,-8.0]

%*********************************************Plot*********************************************************

plot(Voltage,Current,'LineWidth',2)          % Plot of photon current versus battery voltage

%*********************************Title ('Current versus battery voltage')**********************************

ylabel('Current (A)')                        % y- axis labelling
Xlabel('Voltage  (V)')                       % x- axis labelling
grid on
```

A.4 Fast Fourier Transform code

```
%%%%%%%%%%%%%%%%%%%%%%%%%%%%%%%%%%%%%%%%%%%%%%%%%%%%%%%%%%%%
%                                                          %
%*Ayeleso Ayokunle *                                        %
%*211014788 *                                               %
%                                                          %
% *M-file code for Fast Fourier Transform (FFT)*            %
%%%%%%%%%%%%%%%%%%%%%%%%%%%%%%%%%%%%%%%%%%%%%%%%%%%%%%%%%%%%

clc;clear all;close all;
set (0,'DefaultAxesFontSize',14)

vuv1                                % Voltage signal of experiment 1
vuv2                                % Voltage signal of experiment 2
vuv3                                % Voltage signal of experiment 3

mean(vuv1)                          % Average of the voltage signal of experiment 1
mean(vuv2)                          % Average of the voltage signal of experiment 2
mean(vuv3)                          % Average of the voltage signal of experiment 3


A=vuv1(1:5000);                     % Half of the voltage signal of experiment 1
B=vuv2(1:5000);                     % Half of the voltage signal of experiment 2
C=vuv3(1:5000);                     % Half of the voltage signal of experiment 3

vuv1_fft = abs(fft(vuv1));          % FFT of the voltage signal of experiment 1
vuv2_fft = abs(fft(vuv2));          % FFT of the voltage signal of experiment 2
vuv3_fft = abs(fft(vuv3));          % FFT of the voltage signal of experiment 3
```

```
X=((1:10000)*5*10^9)./10000;
Y=vuv1_fft(1:5000)                          % Half of the FFT of experiment 1
Z=vuv2_fft(1:5000)                          % Half of the FFT of experiment 2
W=vuv3_fft(1:5000)                          % Half of the FFT of experiment 3

%********************************************Plot*********************************************************

figure
subplot(3,1,1);
plot(A,'b');                                % Display half of the voltage signal of experiment 1
hold all
plot(B,'g');                                % Display half of the voltage signal of experiment 2
plot(C,'r');                                % Display half of the voltage signal of experiment 3
title('Time domain');
xlabel('Number of samples per seconds');
ylabel('Voltage signal')
grid on

subplot(3,1,2);
plot(X(1:5000)/10e8,Y(1:5000),'b');         % Display half of the FFT of experiment 1
hold all
plot(X(1:5000)/10e8,Z(1:5000),'g');         % Display half of the  FFT of experiment 2
plot(X(1:5000)/10e8,W(1:5000),'r');         % Display half of the  FFT of experiment 3
title('Frequency domain');
xlabel('Frequency (GHz)');
ylabel('Magnitude')
grid on
```

APPENDIX B: The time and frequency spectra of the measured voltage signals of experiments 1, 2 and 3 under VUV pulsed laser radiation conditions

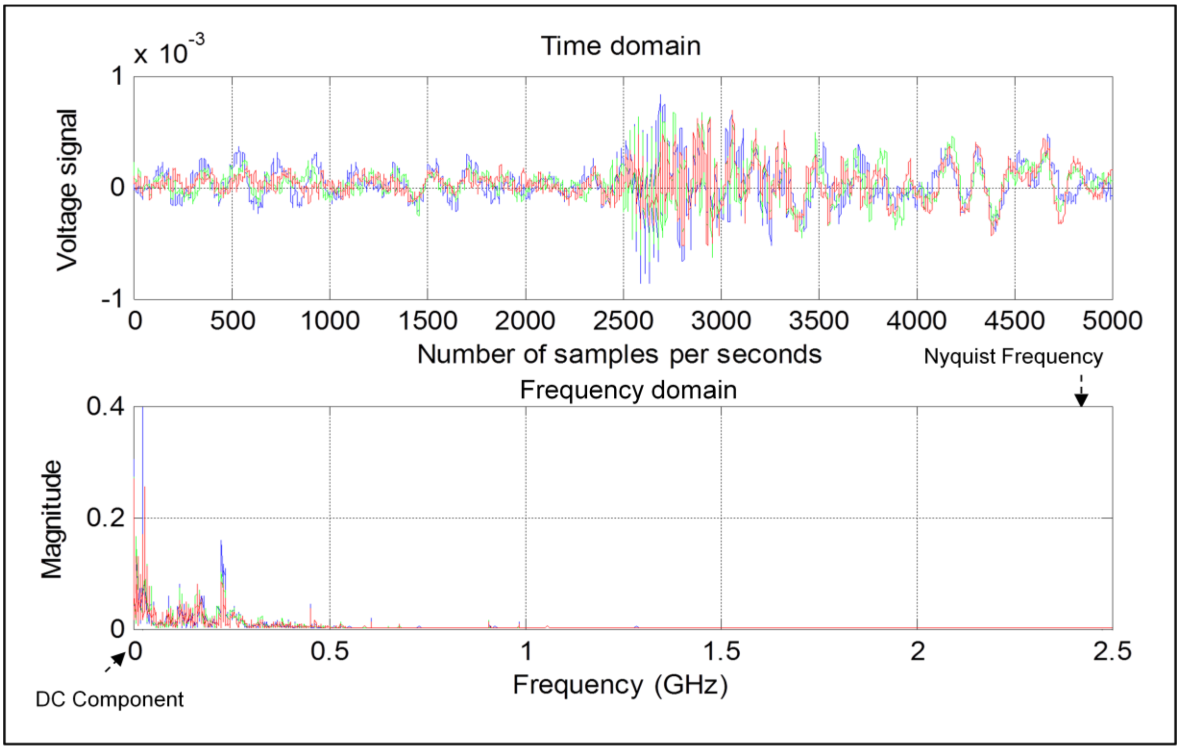

Figure B.1: The frequency spectra of the measured voltage signals of experiments 1, 2 and 3

APPENDIX C: Layout of the VUV deuterium light source

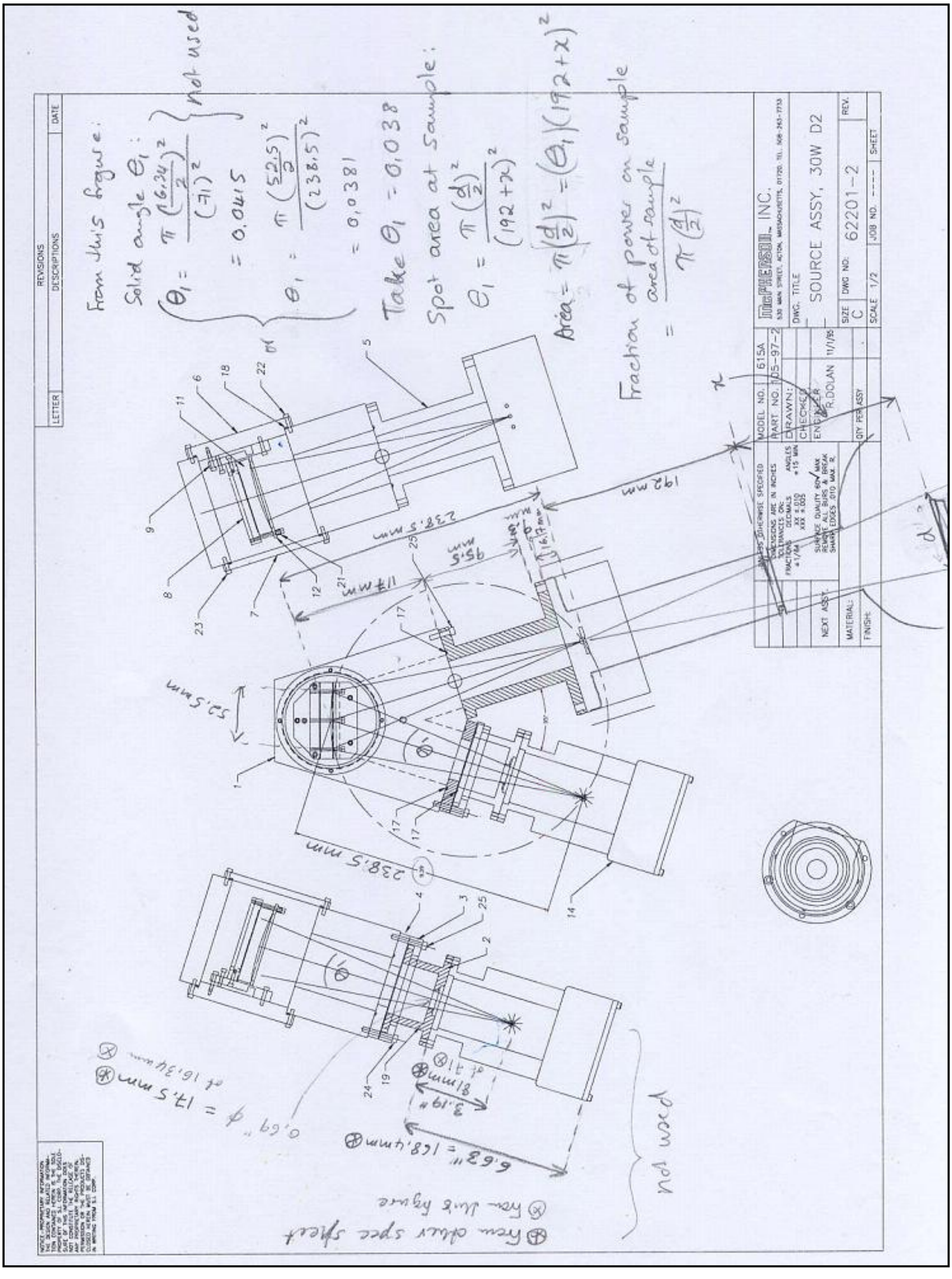

Figure C.1: Layout of the VUV deuterium light source

APPENDIX D: Photos of the planar sensor development stages

Figure D.1: Photos of the planar sensor development stages

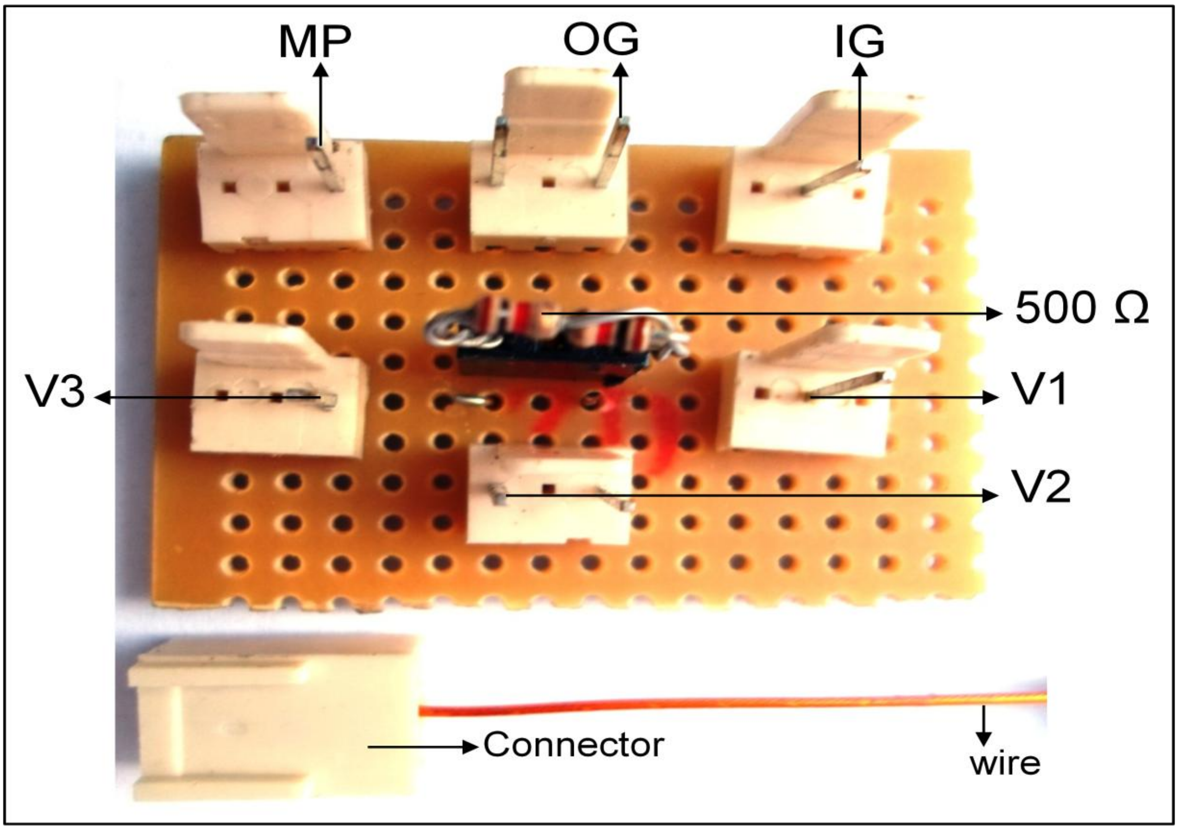

Figure D.2: RC circuit board